Investigating Early Nucleosynthesis of the Lighter Heavy Elements

Cameron J. Angus

Doctor of Philosophy

University of York
Physics, Engineering and Technology
July 2023

Abstract

The r-process produced half of all heavy elements in the universe today. While models successfully reproduce the abundance distributions of the heaviest elements observed in Ultra-Metal Poor stars, the lighter heavy elements ($36 < Z < 47$) are found to be more abundant than predicted. An additional nucleosynthesis process operating at early times in the universe, preferentially producing lighter heavy elements, has been proposed. This project consisted of experimental investigations into two candidates for this process: the weak r-process in the neutrino-driven winds of core-collapse supernovae and the s-process in rotating massive stars.

The ^{20}Ne(d,p)^{21}Ne reaction was studied using the HELIOS spectrometer at Argonne National Laboratory; angular distributions of energy levels in the ^{21}Ne nucleus were measured to determine their neutron widths and spin-parities. These parameters are important for determining the neutron poisoning effects of ^{16}O on the s-process in rotating massive stars. Results for several levels are reported. $J^\pi = \frac{3}{2}^-$ and $\Gamma_n = 7600 \pm 2100\,\text{eV}$ was found for the 7820 keV state disagreeing with the literature assignment of $2J^\pi = (3,5)^+$ and a neutron width limit of $\Gamma_n < 7200\,\text{eV}$ was determined for the first time for the 7749 keV state. Resonance strengths calculated with these results are compared to literature. Both the 7749 keV and 77820 keV energy levels are of astrophysical interest.

The reaction ^{86}Kr(α,n)^{89}Sr was studied at TRIUMF using the EMMA recoil mass spectrometer. Partial cross sections of $1.0^{+0.6}_{-0.8}$ mb and $0.8^{+0.7}_{-0.8}$ mb were measured for transitions in the recoiling ^{89}Sr nucleus from the 1032 keV excited state to the ground state and from the 1473 keV excited state to the ground state respectively; both measurements are in agreement with predictions.

These results will help constrain uncertainty in model predictions of nucleosynthesis for each site and inform future experiments. Ultimately, these results contribute to determining the contribution of these two processes to the abundances of the lighter heavy elements at early times in the universe.

Contents

List of Figures

List of Tables

Acknowledgements

This project has been a real adventure and I owe thanks to the many people who made it possible and helped me get to this point, I can't mention you all here by name but please know that I am very grateful to each of you.

First, my supervisor Alison Laird has throughout this project been fully engaged in both the research and in my development, willing to help even when the time difference meant she had to sacrifice her evenings; thank you so much. Next, a big thank you to Barry Davids for the amazing opportunity to work with him on EMMA, which made this project possible and who was always ready with good advice. Thanks as well to Matt Williams for all of his help in planning, conducting and analysing the ^{86}Kr experiment; good luck with your future research.

The basis of the ^{21}Ne experiment was the work done by Joe Frost-Schenk in his project; thank you for sharing your knowledge and experience with me. I'd also like to thank Phil Adsley for all his help with the DWBA "stuff". The ^{21}Ne experiment was run remotely at the height of the pandemic and virtual communication with Ben Kay and Ryan Tang was irreplaceable; I'm sorry we never got to meet in person, thank you for all your help.

I would also like to mention my original Vancouver housemates: Cassandra, Pedro, Marianne, John, Marc, Nassim and Simon. Moving to a new country is no small thing, especially during the days of coronavirus. You all made those months of social distancing not only bearable, but very special.

Last but not least; Mum, Dad, Ellen, thank you for everything. Love you all.

Declaration

I, Cameron Angus, declare that this thesis is a presentation of original work and I am the sole author. This work has not previously been presented for a degree or other qualification at this University or elsewhere. All sources are acknowledged as references.

Chapter 1

Introduction and Astrophysical Background

1.1 Nuclear Astrophysics and Nucleosynthesis

The physics of nuclei have a great impact on astrophysics, a famous example being the generation of energy inside stars via nuclear fusion reactions. Another case is the study of light curves such as those produced in a type 1a supernova where the radioactive decay of ^{56}Ni and ^{56}Co governs the observed shape of the curve [1]. Combining nuclear physics with observational astronomy can also help trace the galactic chemical evolution of the Milky Way; ^{26}Al is useful in this regard [2]. The focus of this project, however, is *nucleosynthesis*: the creation of the chemical elements. There are many different processes of nucleosynthesis but they all have their roots in the initial formation of the lightest elements (hydrogen, helium and lithium) just after the Big Bang [3]. From these first elements, all of the heavier elements are made [4]. The formation of other elements, can be split into two distinct groups: elements heavier than iron and elements lighter than iron.

The bulk of the light elements (those not made in the Big Bang) are produced in stellar burning, with some made in other sites such as classical novae [5]. During stellar burning, a star is under hydrostatic equilibrium: a state where there is balance between the force of gravity acting towards the centre of the star and the force of the pressure which acts against it. This pressure is generated by energy released in nuclear fusion reactions: where two nuclei merge together to create a heavier element and, in doing so, release energy. A star burning hydrogen in its core is known as a *main sequence* star and it is here that stars spend most of their life. The fusion of hydrogen happens in two ways: through the pp-chain and the CNO cycle. In stars lighter than $1.3\,\mathrm{M}_\odot$ the pp-chain dominates, but above that mass the CNO cycle is more

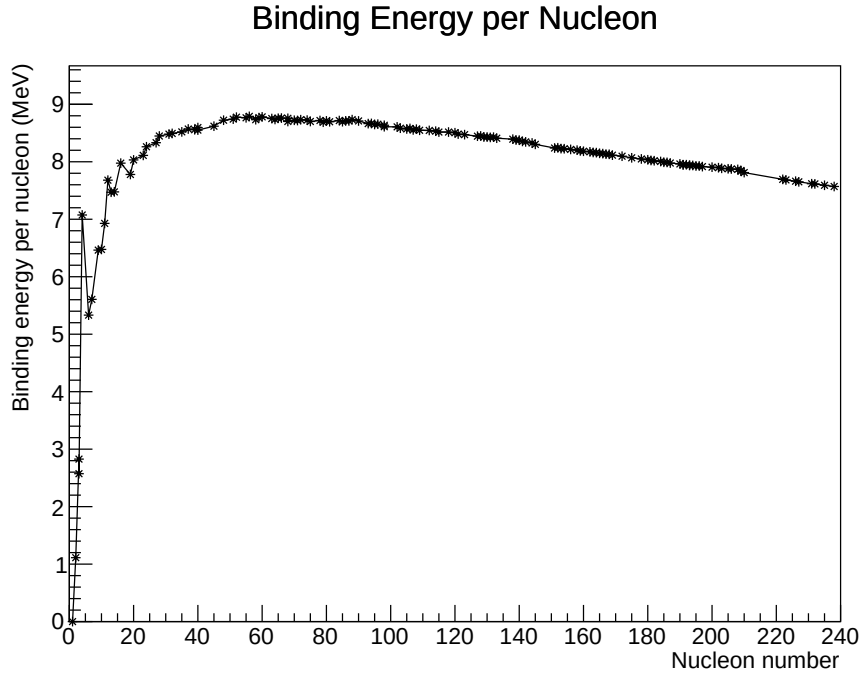

Figure 1.1: How binding energy per nucleon changes as a function of the atomic mass number. Data from: Ref.[8, 9].

significant [6] (for a more detailed description of the CNO cycle, see Chapter 1.3). Eventually, the hydrogen in the core of the star is exhausted and what happens next depends on the initial mass of the star. Stars above $0.3\,M_\odot$ will begin to burn hydrogen in the layers that surround the extinct core which causes the outer layers to expand and cool, forming a red giant [7]. Here, stars with an initial mass similar to that of the Sun may then experience a helium flash as the core ignites and begins to fuse helium into carbon via the triple alpha process. It is worth highlighting that fusion processes in stars produce both helium and lithium, meaning that not all of the He and Li atoms in the universe today were made in the Big Bang.

Stellar nucleosynthesis progressively fuses heavier and heavier elements. For example, the next phase for a star above a mass of $0.5\,M_\odot$ would be an inert carbon-oxygen core surrounded by an inner helium burning shell and an outer hydrogen burning shell; stars such as this are known as an Asymptotic Giant Branch (AGB) stars [10]. Eventually that C-O core may itself re-ignite (if the star is massive enough) and this allows the star to continue to release energy via fusion. The process of fusing ever more massive elements ceases once the star has reached an iron-nickel core, at which point the net production of energy from nuclear fusion is no longer possible. Fig.1.1 shows a plot of binding energy per nucleon vs nucleon number and illustrates that any fusion reactions beyond iron would require a net input of energy since iron is the most stable element. At this point the star will die, how its life ends depends on its mass. This

project concerns the second group of elements: those heavier than iron.

Most of the elements heavier than iron are made in either the s-process (the slow neutron capture process) or the r-process (the rapid neutron capture process) with a small number of elements made in other processes, such as the p-process or the i-process [11]. Predictions for the s- and r-processes are generally robust at reproducing observed elemental abundances, however, there are some discrepancies. One of these discrepancies is the focus of this project. Before that discrepancy can be introduced it is necessary to give some background as to the main modes of heavy-element nucleosynthesis.

1.1.1 The *s*-process

The s-process stands for the slow neutron capture process. In the s-process nuclei are exposed to a flux of neutrons, some of which react to form heavier nuclei in capture reactions. Some of these heavier nuclei are unstable and will radioactively decay. The slow neutron capture process is defined where the rate of neutron capture is much slower than the rate of beta decay: $t_\beta < t_n$. This results in the path of the s-process following the valley of stability up the Chart of the Nuclides by a sequence of neutron captures followed by beta decays, starting at iron and ending at bismuth beyond which point a lack of stable isotopes prevents further progress up the Chart of the Nuclides, as illustrated in Fig.1.2. Bismuth-209 is the last stable nucleus since it has 126 neutrons, a "magic number" corresponding to a nuclear shell closure which helps stabilise the nucleus. Past bismuth, the Coulomb repulsion between protons in a nucleus is too strong to be overcome by the attractive strong nuclear force interactions that act between nucleons and therefore nuclei with additional protons (heavier elements) are unstable. There are two astrophysical sites where the s-process takes place: in Asymptotic Giant Branch (AGB) stars and in massive stars [12]. The timescale of the s-process is on the order of thousands of years, in contrast with the r-process. Today, around 50% of elements heavier than iron are made in the s-process[13]. However, this was not always the case. The s-process is a *secondary process*, i.e. it does require pre-existing *seed nuclei* to synthesise heavy elements [12]. Seed nuclei are iron peak nuclei and in the s-process they must already exist when the star forms. None of the earliest stars would have been able to synthesize elements via the s-process as iron seeds had yet to be released into the intersteller medium by the r-process, therefore stars that formed early in the history of the universe would not have been enriched by the products of the r-process.

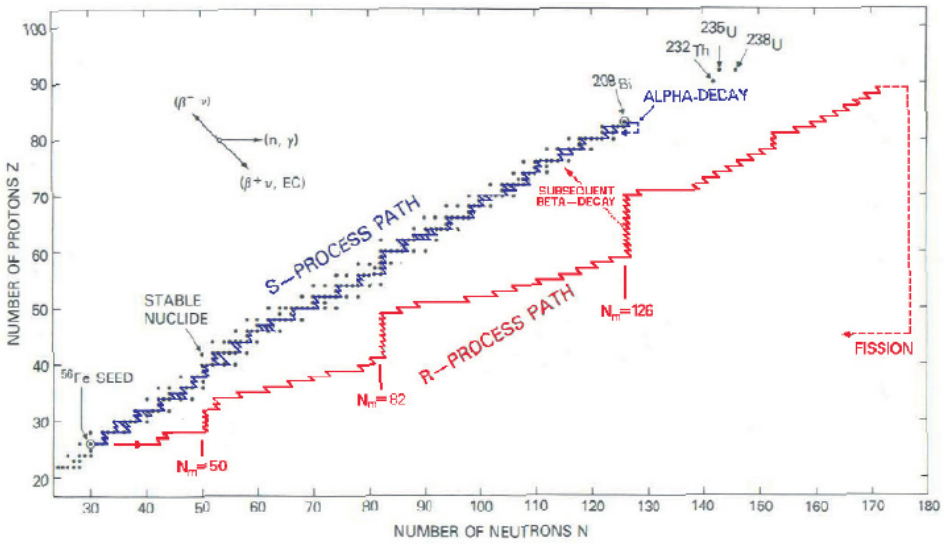

Figure 1.2: The paths of the r-process and the s-process along the Chart of the Nuclides [16].

1.1.2 The r-process

In the r-process, elements heavier than iron are synthesised through neutron capture reactions that happen faster than beta decays $t_n < t_\beta$. This drives nuclei towards unstable neutron-rich isotopes so fast that those isotopes do not have enough time to decay. Once the r-process is complete, these neutron-rich isotopes will eventually decay back to stability over time, as shown in Fig.1.2. Approximately half of all elements heavier than iron in the universe were made in the r-process along with all elements heavier than bismuth. The r-process is very fast lasting at most only a few seconds and occurring in extremely violent events. The specific astrophysical site of the r-process is still debated [14]. However, it is thought to take place in neutron-star mergers [15].

As a *primary process*, the r-process does not need heavy nuclei to exist before its astrophysical site forms [12]. It therefore follows that the first heavier-than-iron nuclei in the universe were synthesised via the r-process, so these elements should dominate the heavier-than-iron metal composition of the oldest stars observable. Stars in ultra-faint dwarf galaxies fall into this category and observations have shown that metals in their composition were produced in infrequent events that co-produced large quantities of both heavy elements ($A > 130$) and lighter heavy elements ($56 < A < 130$) [17]. Models have suggested that this would be the case if the r-process took place in neutron-star mergers [18] and recent analysis of Kilonova GW170817 identified strontium in the spectrum, an element synthesised through neutron capture reactions. This observation lends support to the theory that neutron-star mergers are the site of the r-process [15].

Another potential site of the r-process is in the neutrino-driven winds of core-collapse supernovae. However, models suggest that the conditions in these winds would not be able to synthesize nuclei above $A > 130$ [19]. While the evidence suggests that core-collapse supernovae are not the site of the main r-process, their potential to produce the lighter heavy elements is significant (cf. Chapter 1.2) and they will be discussed in detail in Chapter 1.4.

1.2 The Light Element Primary Process

Following the discussion in Chapter 1.1, it follows that early in the universe, any element heavier than iron should have been generated by the r-process, therefore any stars formed in that epoch should only contain metals that were made in the r-process. To test this theory, astronomers may observe Ultra-Metal Poor (UMP) stars. UMP stars are very old, thought to have formed before the s-process could significantly contribute to the galactic chemical abundances, therefore astronomers can test predictions for r-process nucleosynthesis against observed abundances in UMP stars.

When compared to metal abundances observed in UMP stars, r-process predictions have been found to be robust for the heaviest elements, however, fail to reproduce the abundances of elements heavier than iron but lighter than silver [20]. These so-called *lighter heavy elements*, show a clear overabundance relative to r-process predictions [21]. Strontium, yttrium and zirconium are often looked for in observations studying the r-process as these elements form part of the first r-process peak, which makes them significantly more abundant than other r-process elements [22]. Also, because their 1+ ions have low excitation potentials, they are relatively easy to detect [18].

Fig.1.3 shows the observed abundances for Sr, Y and Zr when normalised to what should be an r-process only element, in this case barium [20]. The x-axis uses the ratio of iron to helium as a proxy for time, since there is a correlation between the age of a star and its metallicity. Metallicity is the fraction of a star's mass that is made of elements heavier than hydrogen or helium. If the Sr, Y and Zr were synthesised in the r-process the abundance trends would appear flat on Fig.1.3. As can be seen, the r-process models under predict the abundances of the lighter heavy elements. When comparing measured solar system abundances to predicted s- and r-process yields, the models fall short for Sr by 8% and for Y and Zr by 18% [20].

This over population cannot be attributed to a flawed understanding of the main r-process because of the otherwise good theoretical predictions at higher Z numbers [20], suggesting that there is another unknown process contributing to the abundance of heavier-than-iron elements early in the Universe. This has been dubbed the *Light Element Primary Process* (LEPP). The

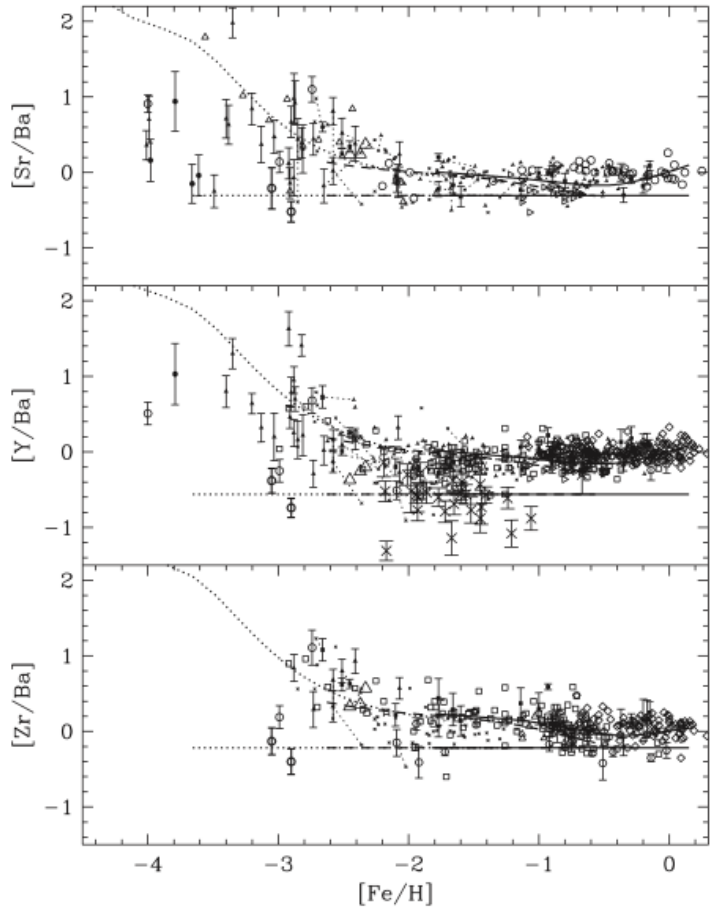

Figure 1.3: The trend in abundances of Sr, Y and Zr relative to barium with varying stellar metallicities compared to predictions based on the r-process [20]. The abundance ratio of iron to hydrogen is used here as a proxy for time.

term "Light Element" is used because whatever the exact mechanism might be, it favours the production of elements within the range of $26 < Z < 47$. It was expected to be a primary process due to the age of the UMP stars. However, as shall be discussed in Chapter 1.3, this may not necessarily be the case.

The difference between the observed and predicted abundances for elements in the first element peak represents an unidentified source of nucleosynthesis in the universe. This project has investigated two candidate processes for the LEPP. Two experiments were conducted, one for each candidate. The first reaction studied was part of an investigation into nucleosynthesis in rapidly-rotating metal-poor stars. The second experiment studied a nuclear reaction of interest to nucleosynthesis in core-collapse supernovae. The aim of this project is to help constrain uncertainties in the nucleosynthesis models for each process. The two candidates that were studied shall now be introduced.

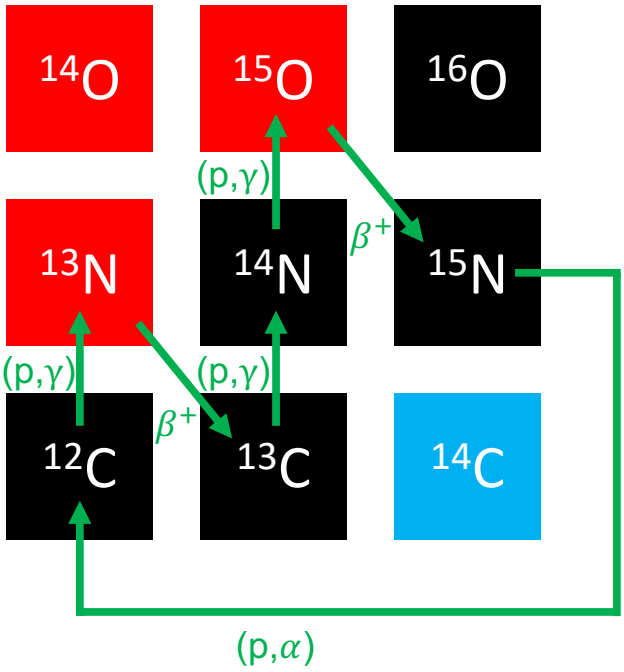

Figure 1.4: A diagram of the CNO cycle on the Chart of the Nuclides.

1.3 The *s*-process in Rapidly-rotating Metal-Poor Stars

The Light Element Primary Process was named according to the theory that only a primary process could significantly contribute to chemical abundances in old stars such as UMP stars. To be the missing source of the lighter heavy elements, the *s*-process would need to be efficient enough to synthesize elements in large quantities from low initial metallicities after the first generation of stars had expired, but before the UMP stars formed. Based on these constraints, the *s*-process was initially discounted as a significant source of lighter heavy elements at early times. However, simulations have shown that nucleosynthesis in rapidly-rotating metal-poor stars could be efficient enough to contribute to their abundances.

^{12}C is produced in the convective helium burning core of massive stars by the triple alpha process. The importance of the rotation of the star is that it mixes ^{12}C from the helium burning core into the hydrogen burning shell where it enhances production of ^{14}N in the CNO cycle. The CNO cycle is the main mode of fusion in the hydrogen burning shell of massive stars [23], in essence the carbon, nitrogen and oxygen in the CNO cycle act as catalysts for the fusion of hydrogen into helium. The CNO cycle can be summarised as ^{12}C(^{1}H,γ)^{13}N(e$^{+}\nu$)^{13}C(^{1}H,γ)^{14}N(^{1}H,γ)^{15}O(e$^{+}\nu$)^{15}N(^{1}H,α)^{12}C [24] with the overall reaction being $4^{1}\mathrm{H} \rightarrow {}^{4}\mathrm{He} + 2e^{+} + 2\nu$, a diagram is shown in Fig.1.4. The ^{14}N is synthesised as part of the CNO cycle. However, as the He core grows, it engulfs ^{14}N ashes left behind by the H

burning shell [25]. Once in the core, the ^{14}N undergoes a series of α induced reactions: ^{14}N(α, γ)^{18}F(e$^{+}\nu$)^{18}O(α,γ)^{22}Ne(α,n)^{25}Mg [26]. The series of reactions ends with ^{22}Ne(α,n)^{25}Mg which is a major source of neutrons for the *s*-process. Depending on the exact model used in the nucleosynthesis calculations, the rotation of a massive star can increase *s*-process yields by several orders of magnitude [26] compared with non-rotating massive stars.

Whether or not this process can account for the missing lighter heavy elements depends on a ratio of the rates two reactions: ^{17}O(α,n)^{20}Ne/^{17}O(α,γ)^{21}Ne [27]; reaction rate is introduced in Chapter 2.4 and is shown in Eq.2.6. The reason for the importance of this ratio is that the rate of *s*-process nucleosynthesis is determined by the flux of neutrons reaching the iron seed nuclei in the outer layers of the star. If some of those neutrons are absorbed before they can react with a seed nucleus then the rate of heavy element nucleosynthesis in that star is diminished. Nuclei that capture neutrons and inhibit the *s*-process are known as *neutron poisons*. ^{16}O is a strong neutron poison [28], capturing a neutron to form ^{17}O, and is produced in quantity during helium burning. What happens after the ^{16}O(n,γ)^{17}O reaction determines the significance of the neutron poisoning effect on nucleosynthesis in rotating massive stars. ^{17}O may undergo reactions with alpha particles and can do so in two ways (beside scattering): ^{17}O(α,n)^{20}Ne and ^{17}O(α,γ)^{21}Ne. The ratio of the ^{17}O+α reactions determines how many neutrons are "recycled" from the ^{16}O neutron capture by ^{17}O(α,n)^{20}Ne and therefore how much of an impact neutron capture by ^{16}O has on the final abundance predictions. The temperature range of interest for helium core burning in rotating metal-poor stars is 0.2 – 0.3 GK [29].

Determining the ^{17}O(α,n)^{20}Ne/^{17}O(α,γ)^{21}Ne ratio is challenging since the cross sections for each reaction are very low, making direct laboratory measurements impractical (although recently the ^{17}O(α,γ)^{21}Ne reaction was partly measured [29]) and thus expected rates are calculated from theoretical models. Because these are light nuclei, their cross sections depend strongly on *nuclear resonances* (cf. Chapter 2.4). These resonances have their origin in the energy levels of the compound ^{21}Ne nucleus. Each energy level has associated parameters known as *spin-parity* and *width* (cf. Chapter 2.3) which help determine the rate of a resonant reaction that proceeds via that resonance. If these parameters are unknown it introduces uncertainty into any attempt to model nucleosynthesis in this site. It is therefore important that information on the energy levels of ^{21}Ne is as complete as possible.

1.3.1 Current Status

At present there remain several energy levels in ^{21}Ne important to nuclear astrophysics that have unknown spin parities and partial widths. Fig.1.5 shows the level scheme for ^{21}Ne prior

to this study with the energy range of interest for He core burning, corresponding to the Gamow window for ^{17}O+α reactions (cf. Chapter 2.2), marked as ΔE_O at 7.65–7.99 MeV, well above the alpha and neutron thresholds at 7347.93(4) keV and 6761.16(4) keV, respectively [9]. Most significant for the ^{17}O(α,n) ^{20}Ne reaction are the energy levels at 7820 keV, 7749 keV and 7981 keV [30], two of which have uncertain or unknown spin-parities.

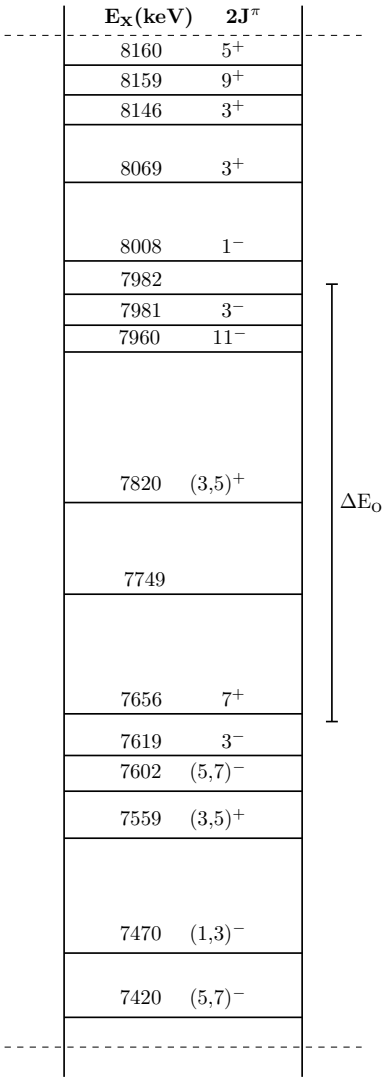

Figure 1.5: A level diagram for ^{21}Ne around the region of astrophysical interest in rapidly-rotating metal-poor stars with information on the spin-parities of each state from Ref.[30]. The neutron threshold is at 6761 keV and the alpha threshold is at 7347 keV [31].

Until recently there were two competing theoretical predictions for the ^{17}O(α,n)^{20}Ne to ^{17}O(α,γ)^{21}Ne reaction rate ratio that disagreed with each other by four orders of magnitude at the energies of interest for rapidly-rotating metal-poor stars. The ratio reported by Ref.[32] predicts that a significant proportion of neutrons are recycled from ^{16}O and was based on

a combination of Hauser-Feshbach theory (cf. Chapter 2.7 for a detailed description) and results from an ^{18}O(α,γ)^{22}Ne experiment [33]. Hauser-Feshbach formalism is at the limit of its applicability for reactions on such light particles and without experimental data for ^{17}O+α reactions, there is a large uncertainty on this prediction. The second model was based on calculations using a three-cluster generator coordinator (GCM) method [34], a microscopic model that builds up from nucleon-nucleon interactions which predicted that the effects of the neutron recycling would be negligible. The GCM method for a nucleus of this mass number was at the limit for the validity of the microscopic model [34] and its prediction has since been excluded by two independent experiments that shall now be discussed.

A measurement at the University of Notre Dame National Science Laboratory studied the ^{17}O(α,γ)^{21}Ne reaction at several energies between 8159 keV and 8659 keV [35] and found that the rate of reaction was significantly higher than predicted by Ref.[34]. The findings of Ref.[35] were later confirmed in an experiment conducted at TRIUMF using the DRAGON recoil spectrometer [29]. DRAGON (the Detector of Recoils And Gammas Of Nuclear reactions) uses a windowless gas target set up [36] and in 2019 was, for the first time, able to directly measure the rate of the ^{17}O(α,γ)^{21}Ne reaction at energies analogous to the highest temperatures within the convective He burning core of massive stars. The measurement within the energy range of interest consisted of one data point that, due to the thickness of the gas target, overlapped with three individual levels close in energy to each other (7982 keV, 7980 keV and 7961 keV). The individual contributions of each of the states could not be determined. However, the overall rate of reaction was calculated and fell in between the predictions of Ref.[32] and Ref.[34], thus excluding the latter.

Previous work to directly measure the ^{17}O(α,n)^{20}Ne reaction [37] determined widths and spin-parities for several energy levels above the energy range of interest by fitting an R-matrix to the measured cross section. The fit was then extrapolated down to lower energy levels relevant to ^{17}O+α reactions in He core burning to estimate the rate of the ^{17}O(α,n)^{20}Ne reaction in stars. It should be noted that it is possible to reproduce the same fit using different resonance parameters and therefore results derived from R-matrices can disagree with studies that use different methods to assign resonance parameters [37].

Combining the ^{17}O(α,γ)^{20}Ne results [37] and the earlier ^{17}O(α,γ)^{21}Ne results [35], an upper limit was determined for the ratio of the two reactions. Fig.1.6 shows that limit in green, calculated in simulations that were based on nuclear data. The limit reported in Ref.[37] was calculated using the results of that study for J^π, Γ_α and Γ_n for the higher-lying states but assumed $\ell = 0$ for all ^{17}O(α,n)^{20}Ne reactions for states in the compound nucleus with unknown spin-parities; alpha widths were estimated with the relation $\Gamma_\alpha = C^2 S \Gamma_{\alpha,\mathrm{sp}}$ taking single-

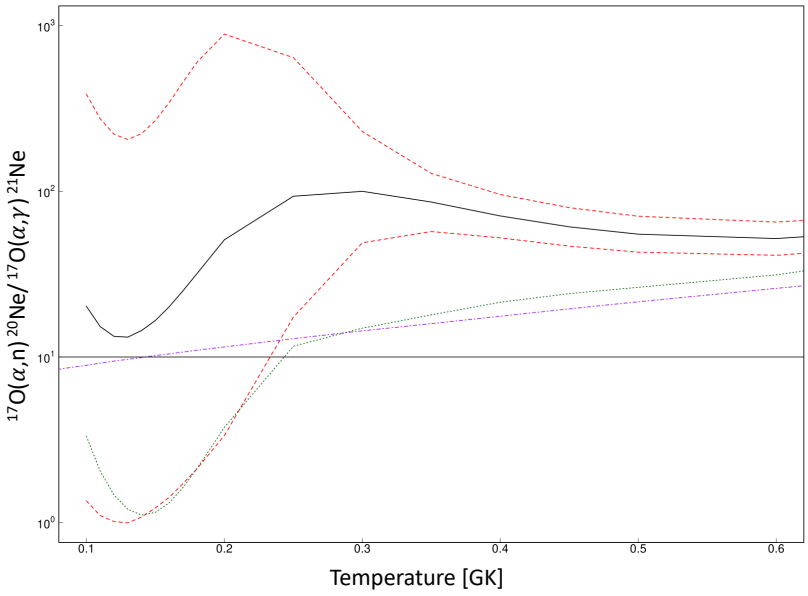

Figure 1.6: Ratio of the rates of reaction for ^{17}O(α,n)^{20}Ne / ^{17}O(α,γ)^{21}Ne [30]. The black line indicates the median rate as calculated in Ref.[30] using experimental data and the red lines indicate the uncertainty limits of that rate. The purple line is the theoretical CF88 rate [32] and the green line is the previous limit estimated using experimental data from reaction studies at energies above the range of interest [35]. Recall that the Gamow window ranges from 0.2–0.3GK in this site.

particle alpha widths ($\Gamma_{\alpha,\mathrm{sp}}$) calculated with the DWUCK4 code [38], assuming a spectroscopic factor (C^2S) of 0.01 where no data were available.

The most up to date predictions for the ratio of ^{17}O(α,n)^{20}Ne to ^{17}O(α,γ)^{21}Ne came from a study conducted with the Enge split-pole spectrometer at the Triangle Universities National Laboratory (TUNL) [30]. That experiment determined the spin-parities of several energy levels in the range of astrophysical interest (shown on Fig.1.5 as ΔE$_\mathrm{O}$) and reported the spin-parity of the 7820 keV level as either $\frac{3}{2}^+$ or $\frac{5}{2}^+$. The TUNL experiment, however, suffered from contamination of their target, a carbon foil implanted with ^{20}Ne. ^{16}O reacted with the deuteron beam through the ^{16}O(d,p)^{17}O channel, producing ^{17}O resonances that overlapped with the proton spectrum of ^{21}Ne making an accurate determination of the spin-parity difficult for the 7820 keV state and impossible for the 7749 keV state. Fig.1.7 shows the TUNL proton energy spectrum at 38° measurement, illustrating the challenges introduced by the ^{17}O contaminant. The results from Ref.[30] were used to re-calculate the ratio of the ^{17}O(α,n)^{20}Ne and ^{17}O(α,γ)^{21}Ne reactions using the RatesMC Monte Carlo code [39, 40], taking the input parameters used in Ref.[37] as a basis and updating them with the newly measured data. Predictions made in Ref.[30] therefore include the same assumptions about spin-parities and alpha widths as Ref.[37] except where new information was available. The result, shown in Fig.1.6, indicated a significantly

higher ^{17}O(α,n)^{20}Ne/^{17}O(α,γ)^{21}Ne ratio than had been reported by Ref.[37] and predicted that enough neutrons are recycled by ^{17}O(α,n)^{20}Ne reactions for a significant quantity of lighter heavy elements to be synthesised in this site by the *s*-process. The black line on Fig1.6 is the simulated median ratio and the red lines are the uncertainty limits, which remain large especially at lower temperatures (cf. Fig.1.6) and further constraining these uncertainties is necessary to improve the precision of nucleosynthesis predictions.

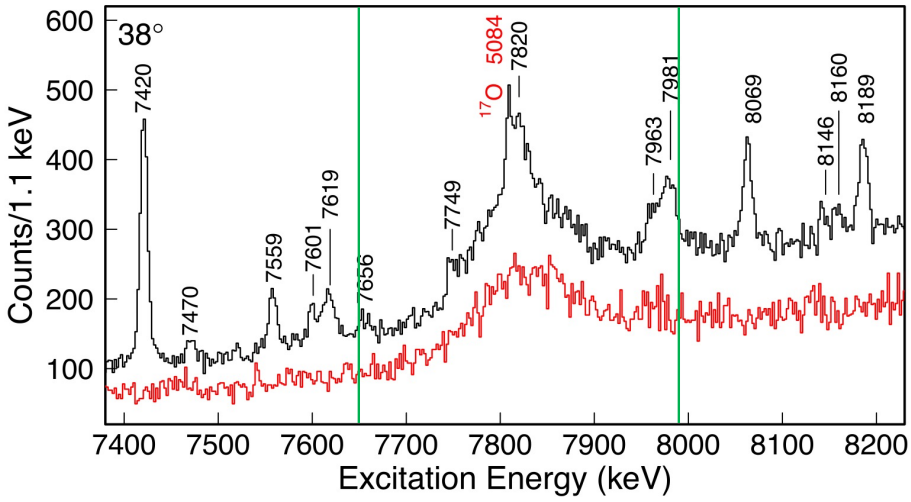

Figure 1.7: The 38° spectrum for the ^{20}Ne(d,p)^{21}Ne experiment of Ref.[30], with the ^{17}O contaminant obscuring the 7820 keV and 7749 keV resonances. The black line indicates the ^{21}Ne excitation energy spectrum and the red line is the carbon spectrum (on an arbitrary scale). The Gamow window is bracketed by the two green lines.

The first experiment that was studied during this project was ^{20}Ne(d,p)^{21}Ne, the same experiment as in Ref.[30]. This time, however, it was conducted in inverse kinematics (cf. Chapter 2.1.2) to avoid the ^{17}O contaminant and enable the determination of the spin-parities and neutron widths of the energy levels within the energy range 7.65–7.99 MeV. The 7749 keV and 7820 keV energy levels were of particular interest. The experiment was conducted at Argonne National Laboratory (ANL) using the HELIOS spectrometer.

1.4 The Weak *r*-process in Core-collapse Supernovae

1.4.1 Neutrino-Driven Winds

Recently it has been shown that the weak *s*-process in rapidly-rotating metal-poor stars alone does not produce sufficient quantities of the lighter heavy elements to fully account for the

overabundances relative to r-process predictions observed in UMP stars, indicating an additional r-process component is required to fully explain the abundance of intermediate mass elements in UMP stars [41]. The additional source of r-process nucleosynthesis is known as the weak r-process. There is some uncertainty on the astrophysical site of the weak r-process, suggestions include magnetorotationally-driven supernovae [42] and the neutrino-driven winds of core-collapse supernovae [43]. This project investigates the latter case: neutrino-driven winds in core-collapse supernovae.

Core-collapse supernovae occur when a massive star ($M > 8\,M_\odot$) reaches the end of its life. After the star exhausts the hydrogen in its core, it proceeds to fuse progressively heavier elements leading to "onion shell" layers, as shown in Fig.1.8. Once the star reaches the iron-nickel core stage, however, fusion reactions require a net energy input (cf. Fig.1.1) and the star can no longer maintain hydrostatic equilibrium, leading it to collapse under gravity. As the star contracts, the core comes under increasing pressure until the electrons and protons combine to form neutrons through electron capture reactions. The core collapse will continue until the pressure reaches the point of *neutron degeneracy*. Neutron degeneracy is a state where the neutrons have been compressed to the point where the *Pauli exclusion principle* becomes relevant. This principle states that: "two Fermions with the same spin cannot occupy the same space". At this point the core cannot be further compressed and the in-falling matter rebounds. This core bounce leads to a shock that radiates outward from the neutron-degenerate core but begins to stall due to the dissipation of energy in photo-disintegration of iron nuclei surrounding the proto-neutron star core [44]. Computer models suggest that the shock will not reach the outer layers of the star, however, it is thought that an enormous outward flux of neutrinos released by the cooling proto-neutron star drives material outward, giving the shock a "second wind" and producing the characteristic explosion associated with a supernova [45]. This model of a core-collapse supernova was first shown to be able to reproduce the observed overabundance of the lighter heavy elements seen in UMP stars by Ref.[43].

Although, as discussed in Chapter 1.1, the main site of the r-process is thought to be neutron-star mergers [47] the conditions in the neutrino-driven winds of core-collapse supernovae are right for the synthesis of the lighter heavy elements (up to $A \sim 130$) [48]. This has been labelled the weak r-process and it is a candidate for the LEPP. While the precise conditions in the neutrino-driven winds are not clear, it is currently thought that they are proton rich with small pockets of neutron-rich ejecta [44, 49]. In the proton rich parts of the outflow the νp-process dominates nucleosynthesis. In the parts of the winds that are slightly neutron rich it has been found that (α,n) reactions become important [11]. Indeed, the name weak r-process is somewhat misleading, since it implies that this is a neutron capture process and

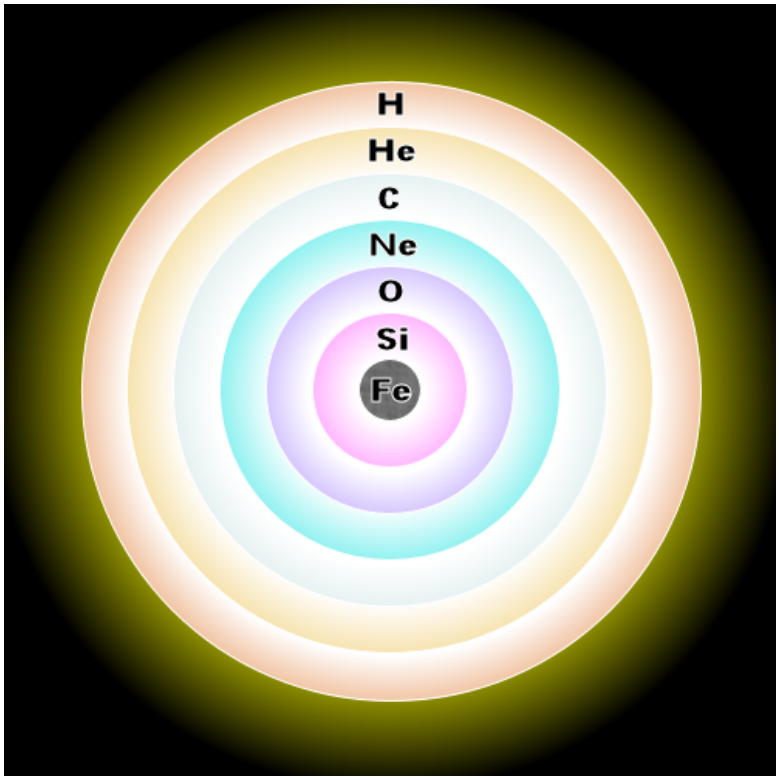

Figure 1.8: The onion layer structure of a pre-supernova massive star [46].

while, neutron capture reactions do occur in this site, the primary driver of nucleosynthesis in neutron-rich winds are (α,n) reactions.

1.4.2 The Role of (α,n) Reactions

Initially, the neutrino-driven winds are in a state of *nuclear statistical equilibrium*, which means that each nuclear reaction is happening at the same rate as its inverse so on average there is no change in the elemental composition of the winds. For example, (p, n) reactions occur at the same rate as (n, p) reactions. The nuclear statistical equilibrium does not last and as the wind evolves, the changing conditions leads to some reactions falling out of equilibrium with their inverse. Simulations have shown that (α,n) reactions are most significant in shifting matter to Z numbers beyond iron [11], Fig.1.9 demonstrates the reason for this: between $2 < T[GK] < 5$ the rate of (α,n) reactions is much faster than that of (n,α) and therefore drives nucleosynthesis. In these simulations the predicted rates of all (α,n) reactions were varied and this resulted in significant differences between final abundance predictions.

The precise conditions within a neutrino-driven wind are unknown, therefore it is important to consider a variety of different possibilities when modelling the weak r-process. By varying the parameters of the simulations that correspond to the physical properties of the winds it was

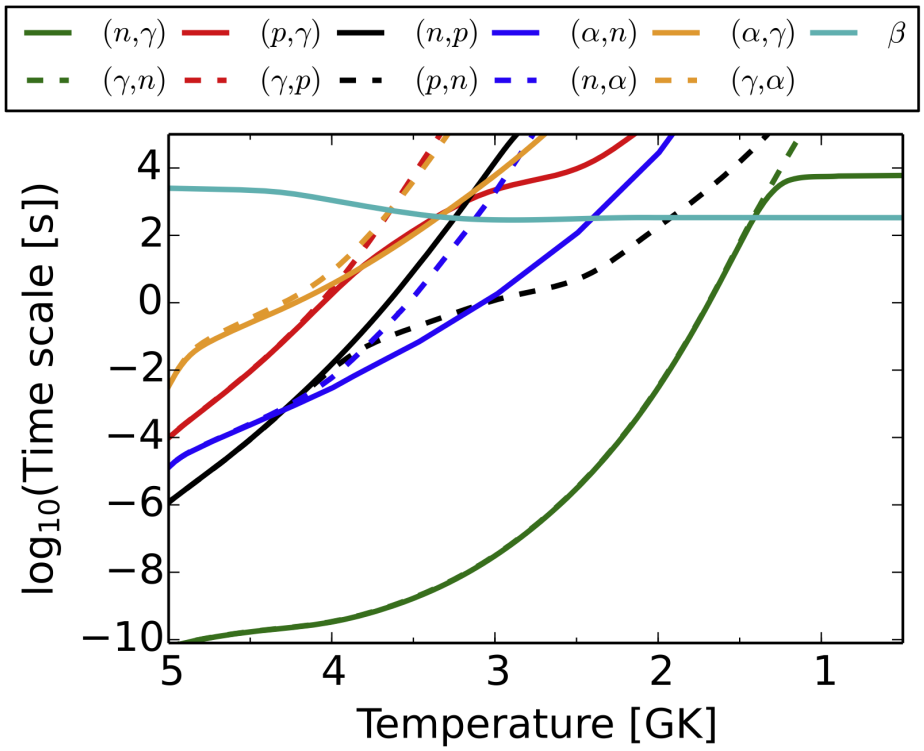

Figure 1.9: The change in the rate of different nuclear reactions in neutrino-driven winds as their temperature evolves over time [11].

found that the baryon fraction (Y_e) had a significant impact on the final abundance predictions [11]. Baryon fraction is the ratio of electrons to the total number of baryons (protons and neutrons). The effect of changing the baryon fraction on the final elemental abundances is shown in Fig.1.10. Note that as those simulations only studied slightly neutron-driven winds the range of baryon fraction considered only covered $0.4 < Y_e < 0.5$. These results illustrate the significance of Y_e to the final abundances and shows that the further Y_e moves from 0.5, the heavier the nuclei that can be synthesised. The reason being that stable nuclei at intermediate masses have more neutrons than protons and therefore since the weak r-process proceeds close to the line of stability more neutrons are needed than protons.

Whatever the exact properties of the winds are, simulations are able to make predictions for their nucleosynthesis. Those predictions contain uncertainties which are dominated by uncertainty of the (α,n) reactions [11], the origin of which is the lack of experimental data for the cross sections of (α,n) reactions. Few studies have been conducted on either stable or unstable nuclei at energies relevant to the weak r-process. In order to include these reactions in simulations, theorists must resort to using model predictions for their cross sections. The model used to predict cross sections for these reactions is known as Hauser-Feshbach theory

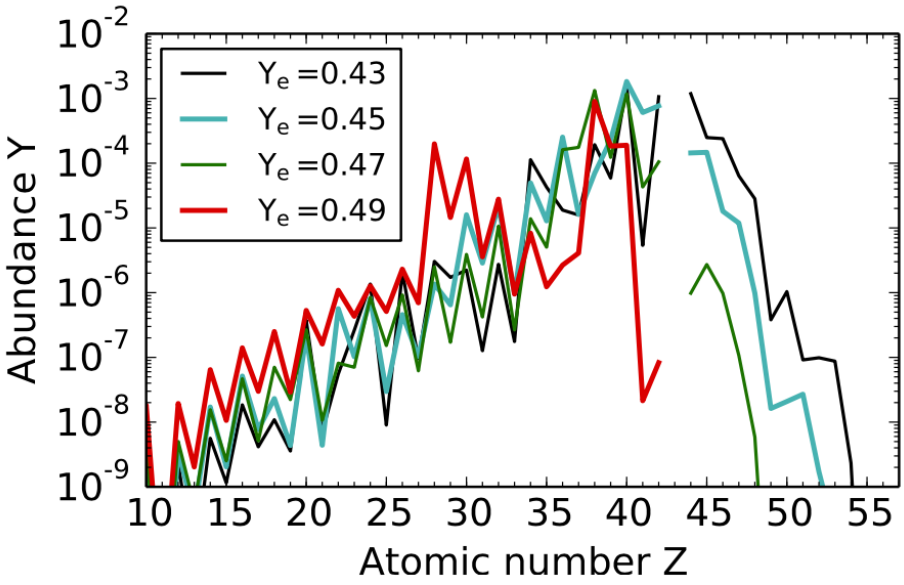

Figure 1.10: The variation of abundance patterns with different values of baryon fraction (Y_e), illustrating that the further below 0.5 the Y_e gets, the more matter is pushed to heavier elements in neutron rich neutrino-driven winds [11].

and will be discussed in detail in Chapter 2.7. Hauser-Feshbach calculations depend on models for the nuclear interaction between the alpha particle and the incident nucleus, known as the *alpha optical model potential* (αOMP). It is in the choice of αOMP that the uncertainty arises, since there are many different αOMPs and their cross section predictions for the same reaction can differ from each other by up to a factor of 10 [11].

1.4.3 Current Status

To date, there are few cross section measurements for (α,n) reactions within the ranges of energy and mass that are relevant for the weak r-process. It must therefore be concluded that to constrain abundance predictions, (α,n) cross sections must be directly measured. Those most important reactions to measure have been identified in the studies of Ref.[50, 51]. Recent experiments have studied the reactions ^{96}Zr(α,n)^{99}Mo [52] and ^{100}Mo(α,n)^{103}Ru [53] at the Institute for Nuclear Research (Atomki) in Hungary which yielded cross section measurements with significantly reduced uncertainties compared to those used in model simulations thus far. Both Atomki experiments used the activation method [54] in which a stable (or very long lived isotope in the case of ^{96}Zr) is bombarded with an alpha particle beam to induce the desired reaction. The reaction products are radioactive and follow the *Radioactive Decay Formula*: $N = N_0 e^{-\lambda t}$ where N_0 is the number of radioactive particles at time zero, t is the time elapsed

since time zero and the decay constant $\lambda = \frac{\ln(2)}{t_{1/2}}$ with $t_{1/2}$ as the half-life of the radioactive isotope. For a detailed description the activation method see Ref.[54].

The ^{100}Mo(α,n)^{103}Ru reaction has also been studied using the MUlti-Sampling Ionisaiton Chamber (MUSIC) active target set up at ANL [55]. In an active target, the detection medium also acts as the target for the beam [56]. Ref.[55] shows agreement between their (α,xn) results and the Atomki (α,1n) results [53] below $E_{CM} = 11.5\,\text{MeV}$.

Recently a new αOMP called Atomki V2 has been developed and has been shown to reproduce the shape of (α,n) reaction cross sections [52, 53, 57]. The Atomki V2 potential was developed after it was recognised that the main source of the discrepancy between αOMP predictions are the tails of the imaginary part of the potentials. The imaginary tails are unconstrained by experimental data leading the Atomki V2 developers to use a pure barrier transmission model to avoid the uncertainties introduced by the imaginary tails. The Atomki V2 potential will be trialled against results from this study.

To decided which (α,n) cross section to measure, it was desirable that the chosen cross section have the maximum impact on constraining the uncertainties. To that end, Ref.[51] was consulted. That study had used a reaction network to model the expected abundances of the lighter heavy elements under various astrophysical conditions, while using a Monte Carlo simulation to vary the (α,n) reaction rates within their theoretical uncertainties. The results identified those reactions that, when their reaction rate was varied, had the greatest impact on final elemental abundance plots. The significant of the impact of varying a given reaction rate on the final abundances was quantified by *Spearman Rank*, which measures the strength of the relationship between a given reaction rate and final abundance of each specific isotope and assigns it a value between -1 and 1 (1 indicating a perfect correlation and -1 indicating a perfect anti-correlation). Based on the work reported in Ref.[51], it was decided that an experiment to measure the cross section of ^{94}Sr(α,n)^{97}Zr would be conducted alongside an ^{86}Kr(α,n)^{89}Sr measurement; the latter using a stable beam to test the experimental setup before moving onto the radioactive ^{94}Sr beam as the main experiment. During the experiment, however, problems with the radioactive beam development meant that the ^{94}Sr(α,n)^{97}Zr had to be postponed. Since the successfully measured ^{86}Kr(α,n)^{89}Sr reaction was also a reaction of interest for the weak r-process, it became the second of the two experiments studied in this project.

In Ref.[51], it was found that the ^{86}Kr(α,n)^{89}Sr reaction impacted "many elemental abundances under many astrophysical conditions", specifically the abundances of elements with Z-numbers: 38–42, 44, 45 & 47. Table 1.1 summarises the impact of the ^{86}Kr(α,n)^{89}Sr reaction on weak r-process nucleosynthesis by listing the variation in the final abundance of each element that was significantly affected, as reported in Ref.[51]. Table 1.1 also includes the

Table 1.1: Summary of the impact of the ^{86}Kr(α,n)^{89}Sr reaction on final abundances of the lighter heavy elements in weak r-process nucleosynthesis [51].

Element (Z)	Abundance Variation	Correlation Coefficient
38	6.81–10.53	0.3–0.58
39	6.62	0.3
40	5.59–6.0	0.35–0.7
41	5.11–14.26	0.2–0.8
42	5.05–8.55	0.22–0.54
44	7.71–31.16	0.5–0.54
45	10.69–31.69	0.22–0.56
47	20.78	0.22

calculated correlation coefficient between the ^{86}Kr(α,n)^{89}Sr reaction rate and the abundance of each element.

The rate of the ^{86}Kr(α,n)^{89}Sr reaction was later found in a second study to significantly impact the abundances of elements: 38, 40–42, 44–46 with abundance variations ranging between 2.07–5.76 and correlation coefficients between 0.33–0.70 [50]. That study followed a similar method to Ref.[51], but differed in that it used the new Atomki V2 alpha optical model potential to constrain the (α,xn) reaction rates. The authors also compared their results to observed abundances in metal-poor stars and thus were able to constrain their simulations to those which were able to reproduce observed abundances. Ref.[50] also provided estimates for the impact on elemental abundance ratios, finding correlations of 0.28–0.69 for Sr/Zr, Y/Zr and 0.21–0.78 for Mo/Zr. These results lead the authors to conclude that the reaction ^{86}Kr(α,n)^{89}Sr affected "few elemental ratios under many astrophysical conditions" [50].

Chapter 2

Nuclear Theory

This chapter explains the nuclear physics underpinning this project. For theory relating to the astrophysical background see Chapter 1 and for the theory behind the detectors used in the two experiments, see Chapters 3 and 4.

2.1 Reaction Cross Sections

In general, an experiment which aims to study a nuclear reaction consists of a beam impinging upon a target. The composition of the beam and the target depends on the reaction being studied. In a reaction between a beam nucleus (projectile) and a target nucleus, the products are a recoiling nucleus and an ejected light particle (except in a capture reaction where there is no ejectile). Since not all beam projectiles incident on the target will react, a reaction has an associated probability of occurring which is measured by a cross section. The number of reactions that happen per second depends on several factors: the reaction cross section, the intensity of the beam and the target areal density. In an experiment designed to measure a cross section the number of reactions taking place is counted while the beam intensity and target density are controlled. The reactions are counted by detecting the recoiling nucleus, ejectile and/or a characteristic gamma ray emitted by the de-exciting nucleus (or some combination of these). The method of detection for any one of these reaction products varies and so experimental set ups depend on the reaction being studied. Each reaction product requires a different detector and with these different detectors there is always be an associated efficiency of measurement which must be included when calculating the cross section of the experiment from the measured yield (Y). Putting all of this together leads to

$$\mathrm{Y} = \epsilon\sigma\mathrm{N_t}\mathrm{I_b} \tag{2.1}$$

Where ϵ represents the total efficiency, σ is the cross section (in units of barns, 1b = $10^{-24}\,\mathrm{cm}^2$), $\mathrm{I_b}$ is the beam intensity (in units of particles per second) and $\mathrm{N_t}$ is the target density (nuclei per square centimeter).

2.1.1 Differential Cross Sections

Eq.2.1 gives the total cross section over the full 4π solid angle. In practice, however, no detector set up can fully cover this 4π range and will only be able to measure part of the total cross section; this is significant because within the full 4π, the measured cross section varies with the position of measurement. Therefore what is actually measured is $\mathrm{d}\sigma(\theta)$ which is the cross section as measured by a detector set at angle θ. Normalising by the solid angle coverage of that detector gives the differential cross section, which is denoted by $\mathrm{d}\sigma(\theta)/\mathrm{d}\Omega$. The angle θ is usually defined relative to the beam axis.

Cross sections vary with parameters other than just angle (such as energy) and strictly speaking equations describing those relationships are also "differential cross sections". However, it is common to refer to the variation of the cross section with angle as the differential cross section and that shall be the case here going forward.

2.1.2 Inverse Kinematics

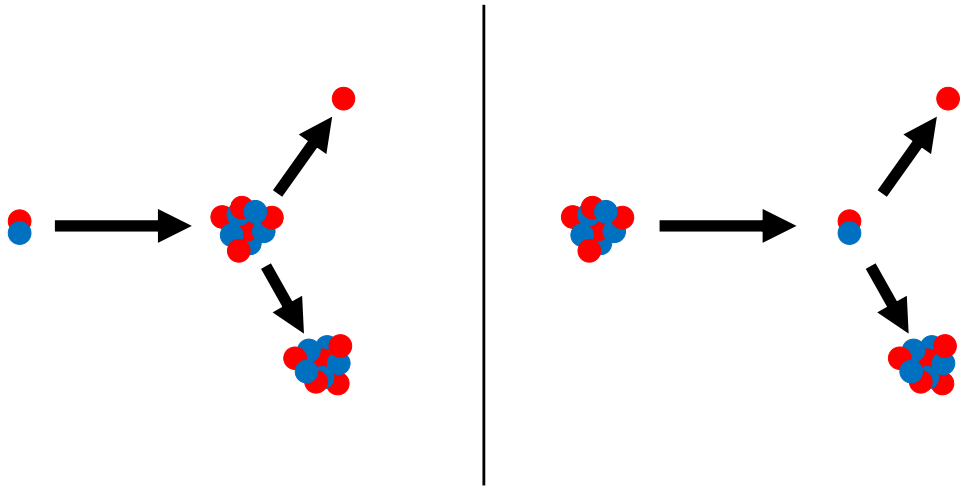

Figure 2.1: A comparison of an experiment conducted in forward kinematics (left) versus inverse kinematics (right).

Traditionally when conceptualising a nuclear reaction one imagines a light nucleus accelerating towards a heavier one and many experiments are indeed conducted in this configuration. However, sometimes this is an inappropriate set up. Some radioactive nuclei have very short

lifetimes which means targets containing them cannot be fabricated. For example, ^{94}Sr has a half-life of 75.3 s [31] and studying reactions on this nucleus is of interest to nuclear astrophysicists [51]. By instead accelerating the heavier radioactive isotope towards a target containing the lighter nucleus enough radioactive nuclei will reach the target and react before they decay, making it possible to study reactions on short lived radioactive nuclei. Fig.2.1 shows a comparison of these two approaches.

The draw back of the inverse-kinematics set up is that compared to forward kinematics the energy resolution is much poorer, since the larger mass of the projectile relative to the target results in forward focusing of the reaction products in the laboratory frame, meaning the detectors effectively cover a much larger angular bin than they would in a forward-kinematics set up. Covering a greater angular range means that particles associated with the same resonance are detected with a greater range of energies on a single detector than they would be in an equivalent forward-kinematics experiment. Fig.2.2 compares data from two experiments studying the ^{20}Ne(d,p)^{21}Ne reaction at similar centre-of-mass energies; one was conducted in forward kinematics (blue) [30] and the other in inverse kinematics (red). The plot shows the proton energy spectrum between 7.0 MeV to 8.2 MeV measured at the same angle in the centre-of-mass frame, though at a different centre-of-mass energy. The inverse-kinematics experiment was conducted at 22.155 MeV and the forward-kinematics experiment at 13.984 MeV and this difference in energy results in variations of the relative height of the resonances shown on Fig.2.2. Nevertheless, Fig.2.2 illustrates the improved resolution of forward kinematics, resonances that are clearly distinguishable in the forward kinematics set up are unresolved in the inverse-kinematics data. There are, however, advantages to studying this particular reaction in inverse kinematics, even though ^{20}Ne is a stable nucleus. A full explanation can be found in Chapter 1.3. However, the main advantage for this comparison is that reactions producing ^{17}O are avoided when using a ^{20}Ne beam instead of a deuteron beam. The feature in the forward-kinematics data on Fig.2.2 at channel number 2600 comes from ^{17}O and obscures part of the ^{21}Ne spectrum, however, as can be seen, is not present in the inverse-kinematics data.

2.2 The Gamow Window

The when planning nuclear astrophysics experiments there are many parameters to consider beyond just the composition of the beam and target, not least at what energy the reaction in question should be studied. The range of energies that are significant for a reaction in a given astrophysical site is called the *Gamow window* and will be introduced here. The energies referred to in this description are in the centre-of-mass frame and must be translated into the

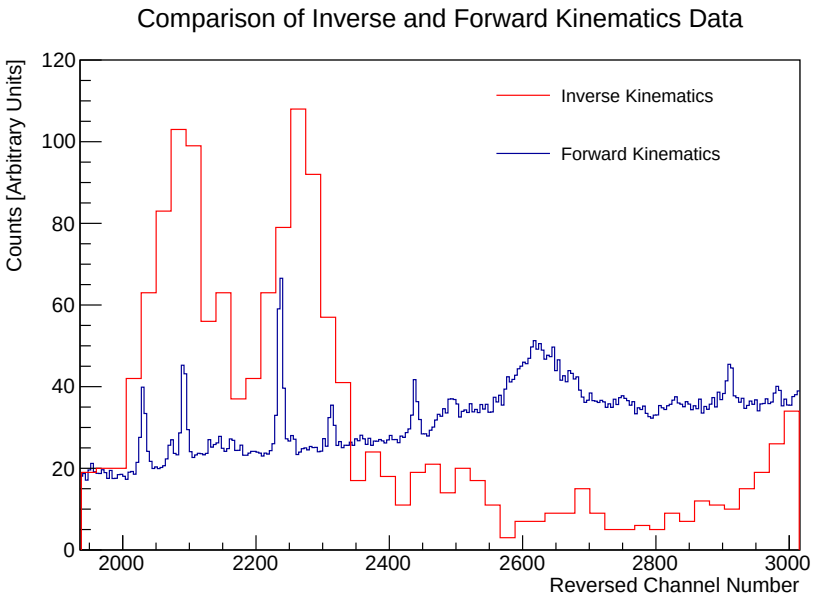

Figure 2.2: A comparison of data from two experiments studying the ^{20}Ne(d,p)^{21}Ne reaction: one in inverse kinematics, one in forward kinematics. Both data taken at the same centre-of-mass angle, equivalent to 16° in inverse kinematics. The y-axes are scaled to compare the shape of the spectrum and the x-axis covers a range of energies from 7.0 MeV to 8.2 MeV. The forward-kinematics data are from Ref.[30] and the inverse-kinematics data are from this project.

laboratory frame when planning experiments.

In the core of a star the protons and neutrons in nuclei are held together by the Strong Nuclear Force. However, beyond a few femtometers, the electrostatic repulsion of the positively charged protons repel other nuclei and the result is a potential barrier to nuclear fusion known as the Coulomb barrier. The shape of the Coulomb potential is shown in Fig.2.3.

The nuclei in a star have a range of energies (dependent on the temperature of the star) which can be modelled with the Maxwell-Boltzmann distribution. Based on this distribution alone, ions in the core of stars would not appear to have sufficient energy to overcome the Coulomb barrier and react. However, the effects of quantum tunneling must also be considered.

A nucleus in a star has a finite probability of quantum tunnelling through the Coulomb barrier and fusing with the nucleus on the other side. This probability depends on the width of the Coulomb barrier as well as the energy of the incident particle. By combining the Maxwell-Boltzmann distribution with the probability distribution of particle to tunnel through a given potential barrier, it can be shown that there is a region of energies where the probability of nuclear reactions taking place is most favourable. Within that range the energy of the reactants is high enough for a significant probability of tunnelling to exist, while still being low enough for a significant number of particles to posses. The range of energies where the

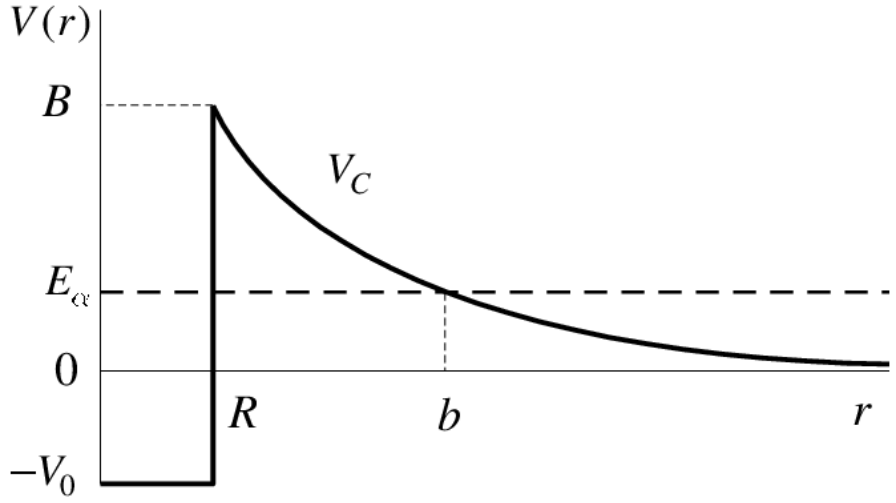

Figure 2.3: The shape of the Coulomb barrier in nuclear reactions. The potential within the nucleus is negative (attractive) indicating the dominance of the strong nuclear force. Outside the nucleus (beyond radius R) the repulsive Coulomb force dominates [58].

reaction is most favourable is known as Gamow Window and is shown graphically on Fig.2.4 along with the Maxwell-Boltzmann distribution and a curve representing the probability of quantum tunnelling to illustrate how the Gamow window arises from both these distributions.

An approximate value for the central energy of the Gamow window can be found with

$$E_o = 0.122(Z_1^2 Z_2^2 \mu T_9^2)^{\frac{1}{3}} \tag{2.2}$$

and the width of the window with

$$\Delta E_o = 0.237(Z_1^2 Z_2^2 \mu T_9^5)^{\frac{1}{6}} \tag{2.3}$$

Combining Eq.2.2 and 2.3 gives the range of energies that defines the Gamow window for two nuclei with reduced mass $\mu = \frac{M_1 M_2}{M1+M2}$ at a temperature T_9 (the subscript indicating units of GK) with Z_1 and Z_2 representing the charges of the two interacting nuclei. The Gamow window describes the range of energies where a reaction in a star is most likely to happen and is therefore the energy range of interest for nucleosynthesis.

2.3 Spin-Parity

Angular momentum is a conserved quantity and in a nucleus arises from two sources: orbital angular momentum and intrinsic spin. Much like in atomic physics, a nucleus can be conceptualised as having a series of energy levels, each with its own quantised orbital angular momentum.

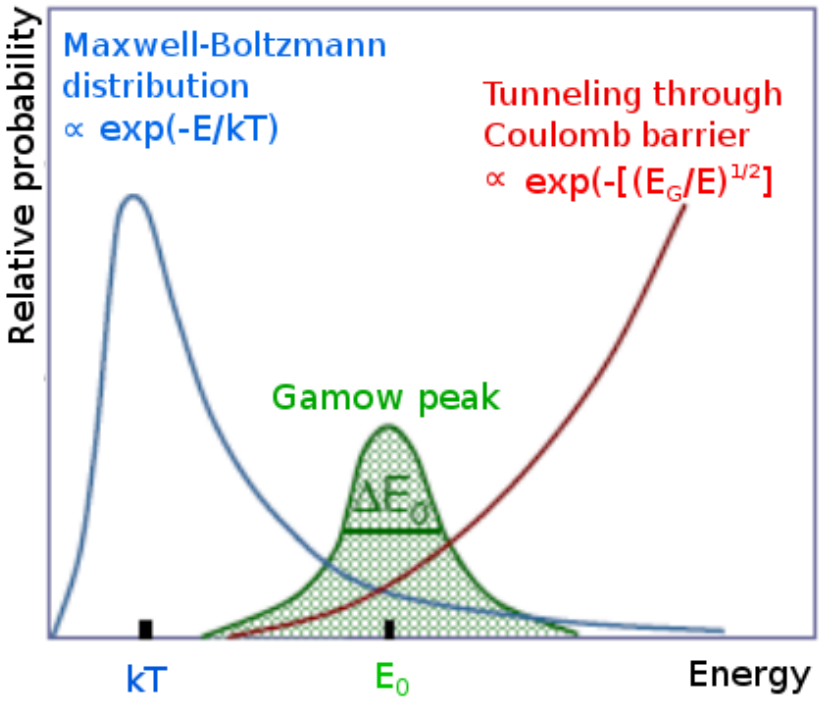

Figure 2.4: The Gamow window arising from the Maxwell-Boltzmann distribution and the probability distribution of quantum tunnelling for a particle with energy E in a astrophysical site of temperature T [59].

The azimuthal quantum number ℓ is derived from the classical equation $\vec{L} = \vec{r} \times \vec{p}$, where $\vec{r}$ is a position vector, $\vec{p}$ is linear momentum and $\vec{L}$ is the angular momentum with its magnitude defined as $L = \hbar\sqrt{\ell(\ell+1)}$ ($\hbar$ is the reduced Planck constant). In the quantum treatment of angular momentum, the quantum number ℓ can only have integer values $0, 1, 2, 3, ...$ (usually denoted *s*,*p*,*d*,*f*...). This theory forms the basis of the nuclear shell model. The number of particles in each energy subshell follows the rule $N = 2(2\ell + 1)$, derived using the magnetic quantum number $m_\ell = -\ell, ..., 0, ..., \ell$ which describes the possible spacial orientations of the nucleons; the additional factor of two originates from the two possible spins that a nucleon may hold. As protons and neutrons are different particles, their energy levels are independent of one another

Since both protons and neutrons are Fermions they each have an intrinsic spin s of either $+\frac{1}{2}$ or $-\frac{1}{2}$. Nucleons naturally fill energy levels from lowest energy up, forming pairs with particles of opposing spin. These two sources of angular momentum, the orbital angular momentum ($\vec{L}$) and the spin ($\vec{S}$), must be combined in a vector sum to find the total angular momentum ($\vec{J}$) of a given nucleus: $\vec{J} = \vec{L} + \vec{S}$. The numbers s, ℓ and m_ℓ are three of the four quantum numbers

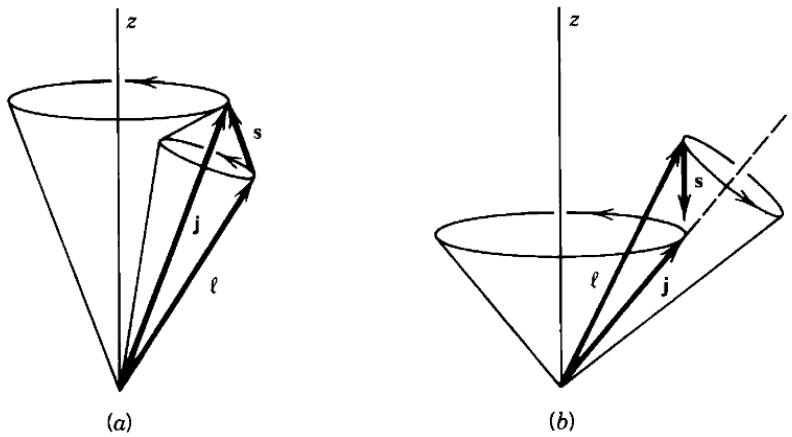

Figure 2.5: The coupling of orbital angular momentum to spin for a nucleon [24].

that describe the shell model. The fourth quantum number is n, the principle quantum number denoting which overall shell a nucleon belongs to.

Because of their pairing-up where there are even numbers of protons or neutrons the nuclear spins cancel out, meaning that the shell model predicts the angular momentum of a nucleus in its ground state originates from any unpaired nucleons. Nuclei with an even number of protons and an even number of neutrons (even-even nuclei) have a total angular momentum of zero and therefore $J^\pi = 0^+$. The + sign indicates that it has positive parity.

Parity is another quantum mechanical property of a nucleus and can either be positive or negative. Two particles that are identical but that have opposite parities can be conceptualised as being mirror images of each other. When parity is positive it means that the wave function of the particle in that state is even, thus satisfying $\phi(-\vec{r}) = +\phi(\vec{r})$. A cosine curve is an example of an even function. When parity is negative, it means that $\phi(-\vec{r}) = -\phi(\vec{r})$, such as is the case for a sine function. The parity of an even-even nucleus is positive by definition. Together, the total angular momentum and parity of an energy level is known as *spin-parity* and is labelled J^π.

2.4 Resonant Reactions

Now that the quantum treatment of angular momentum has been presented nuclear reactions can be returned to; starting with the theory of resonant reactions.

The cross section of a reaction varies smoothly with the centre-of-mass energy between the interacting particles. When this energy matches an nuclear energy level in the compound nucleus, however, the cross section (and therefore the rate of reaction) increases significantly.

The sudden increase in cross section is known as a resonance and in quantum mechanical terms is where the wave function of an incident particle outside of the nucleus matches the wave function of an energy level inside the nuclear potential. Should the Gamow window for a reaction in a given astrophysical site cover a region of $\sigma(E)$ which includes resonances, they can be the dominating factor in the overall rate of reaction.

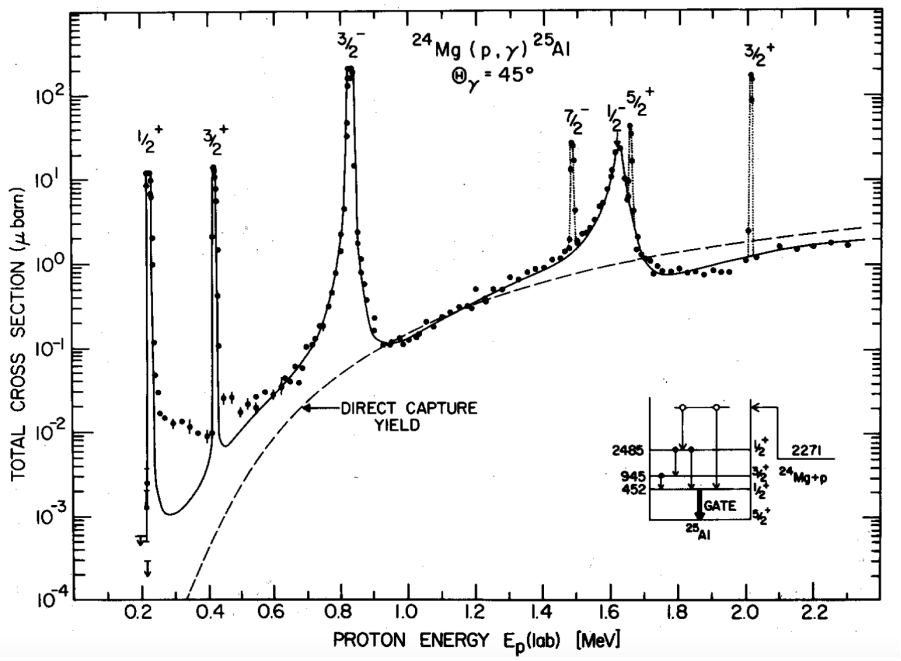

Figure 2.6: The cross section of the ^{24}Mg(p,γ)^{25}Al reaction as it varies with energy including several narrow resonances [60].

The cross section of a reaction that proceeds via a single narrow resonance is described by the Breit-Wigner formula

$$\sigma(E) = \pi\lambda^2 \frac{2J_r + 1}{(2J_1 + 1)(2J_2 + 1)} \frac{\Gamma_a \Gamma_b}{(E - E_r)^2 + (\Gamma/2)^2} \tag{2.4}$$

Where E is the centre-of-mass energy and E_r is the resonance energy. Fig.2.6 illustrates how the presence of a resonance can locally affect the cross section of a reaction.

J_r is the total angular momentum of the resonance and J_1 and J_2 are the angular momenta of the particles in the entrance channel (i.e. the target nucleus and incident particle). Γ is the full width at half maximum of the resonance, equal to $\frac{\hbar}{\tau}$ (where τ is the lifetime of the state). If the range of energies covered by a given astrophysical site is much broader than the total width (ie. $\Delta E >> \Gamma$), the resonance can be said to be narrow in which case, provided the resonance is wholly within the energy range, the narrow resonance approximation applies.

The total width can be decomposed into a series of partial widths: $\Gamma = \Gamma_a + \Gamma_b + ...$ A

partial width represents a possible channel through which a reaction can proceed and its value is proportional to rate of the reaction through that channel. In the Eq.2.4, the subscripts a and b represent the entrance and exit channels respectively. For example, in a reaction between an ^{17}O nucleus and an alpha particle the entrance channel is ^{17}O+α and the products could be ^{20}Ne+n or ^{21}Ne+γ from nuclear reactions or ^{17}O+α from scattering reactions. Each of these possibilities represents an exit channel with its own associated width. Partial widths can be calculated with

$$\Gamma_{\lambda c} = 2\frac{\hbar^2}{mR^2} P_l C^2 S \theta^2_{pc} \tag{2.5}$$

Derived in Ref.[61] where P_c is the penetrability factor: a parameter that represents the penetrability of the target nucleus with respect to the Coulomb and angular momentum barriers, θ^2_{pc} is the dimensionless single-particle reduced width: a parameter representing the probability the single-particle will be present at the nuclear boundary, C is a Clebsch-Gordan coefficient describing the angular momentum coupling, S is the single-particle spectroscopic factor and R is the channel radius. The equation for the rate of reaction is given by

$$< \sigma v >= \left(\frac{8}{\pi\mu}\right)^{\frac{1}{2}} \left(\frac{1}{k_b T}\right)^{\frac{3}{2}} \int_0^\infty \sigma(E) E e^{\frac{-E}{k_b T}} dE \tag{2.6}$$

Where μ is the reduced mass, k_b is the Boltzmann constant, T is the temperature of the astrophysical site, $\sigma(E)$ is the cross section and E is the centre-of-mass energy. Solving Eq.2.6 for a narrow resonance produces

$$N_a < \sigma\nu >= 1.54 \times 10^{11} (\mu T_9)^{-3/2} \omega\gamma e^{-\frac{-11.605 E_r}{T_9}} \tag{2.7}$$

Where T_9 is the temperate of the site in GK, E_r is the central energy of the resonance and N_a is Avogadro's number. $\omega\gamma$ is the resonance strength determined defined by

$$\omega\gamma = \frac{2J_r + 1}{(2J_1 + 1)(2J_2 + 1)} \frac{\Gamma_a \Gamma_b}{\Gamma} \tag{2.8}$$

Here, ω is the spin-factor, $\frac{2J_r+1}{(2J_1+1)(2J_2+1)}$, with J_1 and J_2 representing the angular momentum of the two particles in the entrance channel of the reaction and J_r representing the total angular momentum of the energy level the produces the resonance. γ represents the multiplication of the partial widths for the entrance and exit channels (Γ_a and Γ_b, respectively), normalised by the total width. When one of the partial widths is much narrower than the other, the value of $\omega\gamma$ is reduced to be proportional only to the narrower partial width, since $\frac{\Gamma_a\Gamma_b}{\Gamma} \approx \Gamma_b$ (if $\Gamma_b << \Gamma_a$) [62]. Therefore, measuring these partial widths is vital for knowing the rate of a

particular direct reaction.

2.4.1 Q-value and the Energy Range of Astrophysical Interest

Resonances are found where the centre-of-mass energy of the incident reactants matches an energy level in the recoiling nucleus. The following equation can be used to determine which energy levels are of relevance for a reaction in a given astrophysical site

$$E_{range} = Q + E_o \pm \frac{1}{2}\Delta E_o \tag{2.9}$$

Where E_o is the central energy of the astrophysical site as determined by Eq.2.2 and ΔE_o defining the width of the range of interest (cf. Eq.2.3). Q is known as the Q-value which is the amount of energy released or absorbed in the nuclear reaction. If this is positive the reaction is exothermic and releases energy, if negative then it is endothermic and absorbs energy. The Q-value of a reaction can be found with $Q = [(M_p + M_T) - (M_e + M_R)]c^2$, where M_T is the mass of the target nucleus, M_R is the mass of the recoiling nucleus, M_p is the mass of the projectile and M_e is the mass of the ejectile.

2.5 Direct Reactions and Compound Reactions

As mentioned in Chapter 1.3, it is not always practical to experimentally measure reactions and therefore approximations must be made. For example, to study the *s*-process in rapidly-rotating metal-poor stars the ^{20}Ne(d,p)^{21}Ne reaction was used to probe the energy levels of the ^{21}Ne nucleus. A (d,p) reaction is an example of a transfer reaction, which in turn is a type of direct reaction. Direct reactions occur when the de Broglie wavelength of a projectile ($\lambda = \frac{h}{p}$) is comparable to the distance between nucleons in the target nucleus. The probability of such a reaction occurring increases with energy. This type of reaction is fast, happening in timescales on the order of $\sim 10^{-21}$ s.

Compound nuclear reactions are slow (lasting $\sim 10^{-18}$– 10^{-16} s) due to the requirement for thermal equilibrium to be established between the nucleons inside the compound nucleus that forms from the fusion of the two reactants [24]. The decay of the compound nucleus is therefore independent of its formation making the whole process a two-step reaction, in contrast to direct reactions where the interaction between target and projectile occurs on the surface of the nucleus in one quick step.

Because the theory of these two types of reaction are so different, separate models are needed to describe them. Direct reactions can be modelled using the Distorted-Wave Born

Approximation which will be discussed in Chapter 2.6 and compound reactions can be modelled with Hauser-Feshbach theory which will be introduced in Chapter 2.7.

2.5.1 Selection Rules for Direct Reactions

When conservation rules are combined with the quantisation of physical properties it can be seen that in a direct reaction there are only certain combinations of angular momenta and parties are possible. The two equations that determine the possible outcomes are known as selection rules and are

$$||J_a - \ell| - s| \leq J_b \leq J_a + \ell + s \tag{2.10}$$

$$\Delta\pi = (-1)^{\ell} \tag{2.11}$$

Where J_a is the total angular momentum of the initial nucleus, J_b is the total angular momentum of the final nucleus, ℓ is the orbital angular momentum quantum number and s is the spin of the transferred particle ($s = 0$ for alpha particles or $s = \frac{1}{2}$ for protons and neutrons). It is important to remember that these rules only apply to direct reactions, since compound reactions last long enough that the exit channel is effectively independent of the entrance channel from a quantum physics standpoint.

2.6 The Distorted-Wave Born Approximation

A nuclear reaction is envisaged classically as a series of particles interacting like billiard balls. In the quantum treatment, however, particles can be represented as waves with wave functions that describe them. The Distorted-wave Born Approximation (or DWBA) uses the wave like nature of particles to model direct reactions.

In DWBA, a direct reaction is modelled by treating the incoming projectile nucleus as a plane wave and the reaction as a perturbation to that wave; this is illustrated in Fig.2.7. This perturbation contains the information about the reaction that took place. In the optical model, the plane wave is incident on a partially opaque sphere that represents the target nucleus (stationary in the laboratory frame) [24]. Analogous to optical physics, part of the wave is reflected and part is transmitted. The total interaction potential is the sum of both of these parts

$$V(r) = V_r(R) + iU(R) \tag{2.12}$$

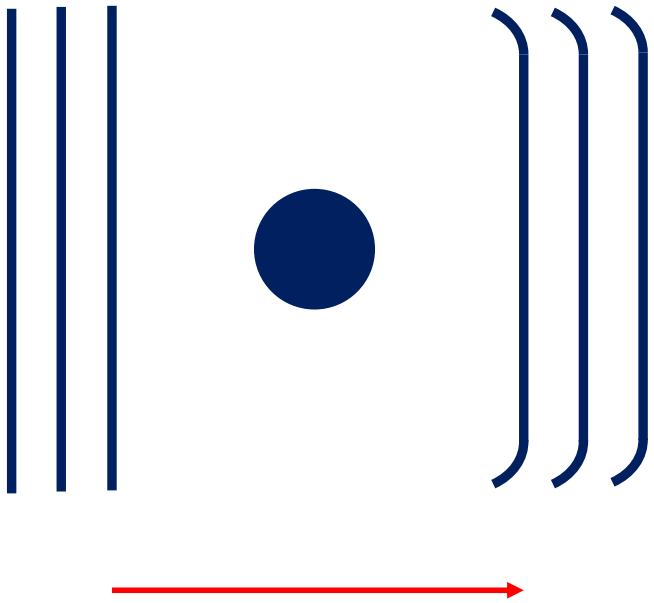

Figure 2.7: A simple diagram illustrating the DBWA treatment of a direct reaction, with wavefronts shown before and after the interaction.

$V_r(R)$ is the real term which represents elastic scattering and is usually based on the Woods-Saxon potential combined with the Coulomb potential. $U(R)$ is the imaginary part of the potential (i.e. the part that is transmitted) and represents the inelastic nuclear reactions (including direct reactions). The differential cross section of the transmitted wave displays an interference pattern, similar to double-slit diffraction. When direct reactions occur via a narrow resonance the quantum mechanical properties of the energy level that gave rise to the resonance have an impact the reaction. A relevant example for this project is that the spin-parity of an energy level affects the shape of the differential cross section of a reaction[63]. Experimenters can therefore determine the spin-parity of individual energy levels by measuring the differential cross section for a resonant reaction across several angles and compare the resulting data to possible theoretical predictions made using DWBA. Each prediction is produced by modelling the reaction with a different angular momentum transfer ($\Delta\ell$) while holding all other variables constant. The spin-parity assigned to that state is the one whose theoretical prediction best fit the data. The code used to produce DWBA predictions for the ^{20}Ne(d,p)^{21}Ne part of this project was FRESCO [64].

Once the spin-parity has been determined, the next step is to extract the partial width. DWBA contributes to this by providing the spectroscopic factor of each energy level. The spectroscopic factor scales the measured differential cross section to the value predicted by DWBA theory, this relationship is

$$\frac{d\sigma}{d\Omega}^{exp} = C^2 S \frac{d\sigma}{d\Omega}^{theory} \tag{2.13}$$

The spectroscopic factor can then be used in Eq.2.5 to calculate the partial width.

Using DWBA to determine the spin-parities of a reaction has its limits. By nature, assignments made using DWBA are model dependent, since assignments are by comparison to model predictions and these models do not always reproduce observed physics accurately or may only be valid under certain conditions, for a relevant example of this see Chapter 2.6.2. Sometimes the predictions made using DWBA for two different spin-parities can both agree with the experimental data, in which case it is difficult to determine which is the most appropriate assignment.

2.6.1 Optical Model Potentials in DWBA

Difficulty arises in modelling reactions due to there being many interacting bodies within the a nucleus. The many interactions are approximated by optical model potentials (OMPs). Precisely what information is contained within the OMPs depends on the model being used. As mentioned already, an OMP often begins with a Woods-Saxon central potential representing the short-ranged nuclear forces and builds from there, adding terms to represent the Coulomb interaction (electromagnetic) and sometimes a term representing the spin-orbit coupling though this can be a minor component of the total potential [65]. The linear sum of these parts to the real potential is

$$V_r(r) = V_{WS} + V_{coul} + V_{SO} \tag{2.14}$$

Where, V_r is the real potential, r is the radius, V_{WS} is the Woods-Saxon potential contribution, V_{coul} is the Coulomb potential contribution and V_{SO} is the spin-orbit potential contribution. The imaginary terms have been omitted for clarity. The imaginary potential may also have several terms, depending on the specific model being used.

The final potential is substituted into the Schödinger equation along with the wave function of the relevant particle and used to calculate the radial wave equation for the particle experiencing the potential

$$\frac{d^2 u_L(r)}{dr^2} + \left(\frac{2m}{\hbar^2}[E - V(r)] + \frac{L(L+1)}{r^2} \right) u_L(r) = 0 \tag{2.15}$$

Here, $u_L = rR$ where R is the radial component of the potential, r is the radius, $\hbar$ is the Planck constant, L is an integer value, m is the particle mass, E is the total energy and V(r)

is the potential. This equation is solved first within the radius of the nuclear potential and then outside the potential by solving the radial wave equation again, this time without the potential. The requirement is then set that the wave function should transition between these two solutions smoothly [66]. The wave function used to produce Eq.2.15 is the spherically symmetric solution $\Phi(r) = \sum \frac{u_L(r)}{r} i^L P_L(\cos\theta)$, with P_L being the Legendre polynomial and θ is the angle to the z-axis.

Integrating the radial wave equation over a series of steps gives the wave function of the recoiling particle and comparing that to the same wave function in the absence of a nuclear potential yields the differential cross section of the reaction. When modelling direct reactions parameters such as the number of steps or the size of each step can have a significant impact on the final results and therefore must be selected with caution [64].

To reproduce a direct reaction computationally using this formulation, different potentials are needed. Precisely which depends on the reaction being modelled. However, for a transfer reaction such as was studied in this project, one OMP is needed for the entrance channel, one for the exit channel, one describing the incident nucleus, one for the core-core interaction and one describing the recoiling nucleus [64].

The choice of which OMP to use for each of these potentials depends on the conditions the reaction is being simulated under. An important consideration is whether to select a local or a global potential. A local potential is valid for a specific reaction at a specific energy and is often derived from empirical measurements. A global potential is valid across a range of energies and nuclear masses for a given interaction and consists of theoretical functions which vary the shape of the potential with the changing parameters of the interaction, for instance Ref.[67]. Local potentials are desirable where possible since they are usually based on data. However, when a reaction has not been studied before global potentials can be used, such as is the case in this project.

2.6.2 The Adiabatic Approximation

Above beam energies of $E = 10\,\mathrm{MeV/u}$ in (d,p) reactions deuteron break up becomes important [68, 69] and this causes an issue for the DWBA predictions because the OMPs are based on elastic scattering and do not account for that break up. Thus as the beam energy increases and break up effects becomes more important, DWBA predictions become less accurate. It is possible to adjust the OMP of the entrance channel to account for the break up of the deuteron using a linear correction known as the adiabatic approximation [70]. While the modified OMPs have been shown to best describe (d,p) transfer reactions above $E = 10\,\mathrm{MeV/u}$, they do so at the

expense of a good representation of elastic scattering. The modified theory is called ADWA (the Adiabatic Distorted-wave Born Approximation). A comparison between DWBA and ADWA for certain energy levels populated in the ^{20}Ne(d,p)^{21}Ne experiment at beam energies of $E = 11\,\mathrm{MeV/u}$ is made in Chapter 3.3.

2.7 Hauser-Feshbach Theory

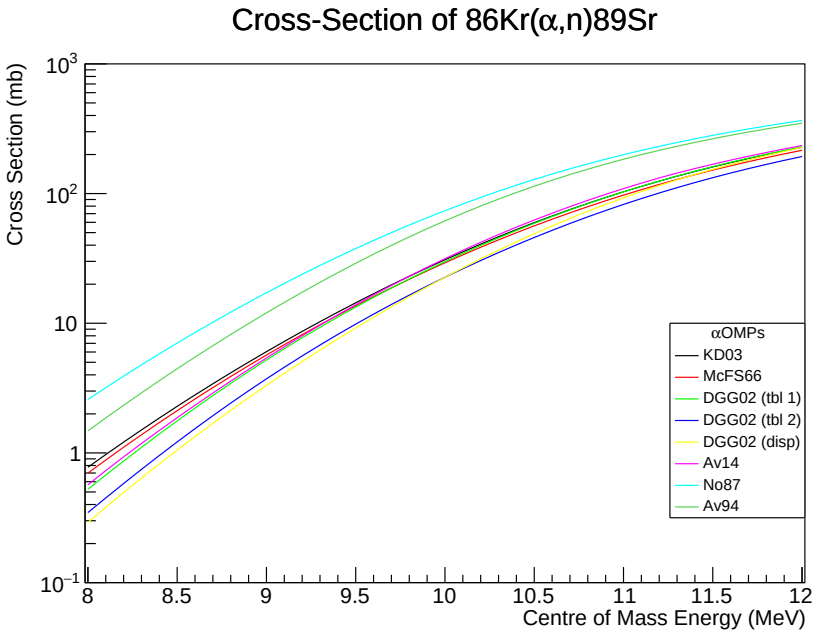

Figure 2.8: An example of Hauser-Feshbach predictions for the cross section of the ^{86}Kr(α,n)^{89}Sr reaction made using different αOMPs [71, 72, 73, 74, 75, 76].

While single narrow resonances dominate the rates of reaction for lighter nuclei, reactions involving heavy nuclei are different. In heavier nuclei, the protons and neutrons are much more numerous meaning that there are many excited states close enough together that they overlap. The cross section of a reaction can therefore be modelled as varying smoothly with energy by statistically averaging the contributions from the individual energy levels. This approach is known as Hauser-Feshbach theory [77] and can used in circumstances where there are no experimental data for the cross section of a reaction. It is important to note here that this is not a direct reaction because the reaction forms a compound nucleus as an intermediary step between the entrance and exit channels.

The Hauser-Feshbach formula underpins this theory [77]

$$\sigma_{ab}^{HF}(E) = \pi\lambda^2 \sum_{J\Pi} \omega_a \frac{\sum_{\{j_a\}} T_a \sum_{\{n_b\}} \sum_{\{j_b\}} T_b W_{ab}}{\sum_c \sum_{\{n_c\}} \sum_{\{j_c\}} T_c} \tag{2.16}$$

Here, σ_{ab}^{HF} is the cross section, E is the centre-of-mass energy, the subscripts a and b denote entrance and exit reaction channels respectively and c represents all the channels that are open. $\{j_a\}$ and $\{j_b\}$ are the angular momentum in the entrance and exit channel, respectively, $\{j_c\}$ represents the angular momenta defining a given channel and $\{n_c\}$ are all possible discrete states in the residual nuclei, while $\{n_b\}$ are only those states being considered. Π is the parity of the compound system, λ is the reduced wavelength in the incident channel, ω_a is the spin-factor of the entrance channel ($\omega_a = \frac{(2J_r+1)}{(2J_2+1)(2J_1+1)}$, where J_r is the total angular momentum of the energy level that produces the resonance and J_1 and J_2 are the angular momenta of the reactants) and W_{ab} is a factor relating the individual averages of partial widths for channels a and b to the combined average of both over the total width ($\langle \frac{\Gamma_a \Gamma_b}{\Gamma} \rangle = W_{ab} \frac{\langle \Gamma_a \rangle \langle \Gamma_b \rangle}{\langle \Gamma \rangle}$). The terms T represent the transmission coefficients for each of the channels and are calculated from the optical model potentials used to model the reaction. These OMPs are one of the three main input parameters, the choice of which can significantly affect the predictions made using Hauser-Feshbach theory. The other two parameters are the gamma strength function and the level density function. The gamma strength function describes the gamma-ray channel of a nuclear reaction and enters into Eq.2.16 through the transmission coefficient calculated for gamma-ray channels. As can be deduced from its name, the level density parameter describes the density of the nuclear energy levels in the outgoing channel b. Level density is an important parameter where there is a range of possible final state energies in the outgoing nucleus. The following equation shows the extension of Eq.2.16 to show the variation of the cross section with numerous energy levels in the outgoing nucleus, including the level density function $\rho(E_b, I_b, \Pi_b)$

$$\frac{d\sigma_{ab}^{HF}(E)}{dE_b} = \pi\lambda^2 \sum_{J\Pi} \omega_a \frac{\sum_{\{j_a\}} T_a}{\sum_c \sum_{\{n_c\}} \sum_{\{j_c\}} T_c} \sum_{I_b,\Pi_b} \sum_{\{j_b\}} T_b W_{ab} \rho(E_b, I_b, \Pi_b) \tag{2.17}$$

Where E_b, I_b and Π_b are the final energies, spins and parities respectively. The derivation of Eq.2.16 will not be given here. However, a clear description can be found in Ref.[78], starting from the Breit-Wigner formula (cf. Eq.2.4).

The Hauser-Feshbach calculations for the ^{86}Kr(α,n)^{89}Sr part of this project were done using the computer model TALYS (version 1.95) [79]. An example plot made with TALYS is shown in Fig.2.8 and was made by holding all parameters constant except the choice of αOMP, which was varied to show how the selection of OMP can significantly affect the predictions made with Hauser-Feshbach theory.

Chapter 3

^{20}Ne(d,p)^{21}Ne for the *s*-process

3.1 The HELIOS Spectrometer

The Helical Orbital Spectrometer (HELIOS) is part of the Argonne Tandem Linac Accelerator System (ATLAS) facility [80] at Argonne National Laboratory (ANL) in the United States and studies nuclear reactions using an inverse kinematics setup. The beam that reaches HELIOS has been accelerated through a series of Linacs (linear accelerators): the PII Linac, Booster Linac, and finally, the ATLAS Linac. For radioactive isotope beams, the Argonne In-flight Radioactive Ion Separator (RAISOR) can then be used to purify radioactive beams before they reach the experimental end stations. The available ions sources for beam production are an Electron Cyclotron Resonance (ECR) source and the CAlifornium, Rare Isotope Breeder Upgrade (CARIBU). CARIBU is used to produced neutron-rich isotopes [81] that are then ionised by an Electron Beam Ionisation Source (EBIS), which uses electron impact reactions to produce ions. For this experiment, the ECR was used to produce the ^{20}Ne beam The ECR works by applying a magnetic field to gaseous atoms and electrons, then exciting the electrons using incident microwaves that have a frequency equal to the electron cyclotron frequency, such that they impact the neutral atoms and produce ions [82].

As is shown in Fig.3.1, HELIOS is a large solenoid with the beam entering along the axis and impinging upon a target [83]. The force exerted on a moving ion in an electromagnetic field is described by the Lorentz equation

$$\boldsymbol{F} = q(\boldsymbol{E} + \boldsymbol{v} \times \boldsymbol{B}) \tag{3.1}$$

where q is the charge of the ion (measured in C), $\boldsymbol{v}$ is the velocity of the ion (measured in m/s), $\boldsymbol{B}$ is the magnetic field strength (measured in T), $\boldsymbol{E}$ is the electric field strength (measured

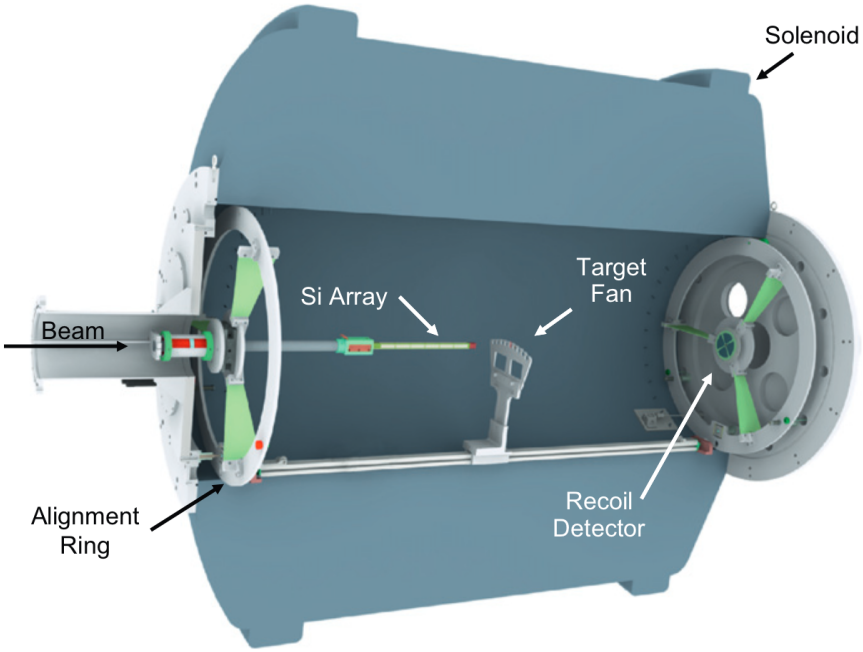

Figure 3.1: A labelled diagram of the HELIOS Spectrometer [83]

in V/m) and $\boldsymbol{F}$ is the resulting force on the ion (measured in N). Because HELIOS is a solenoid the magnetic field lines inside the spectrometer are parallel to the beamline and uniform; this means when light particles (such as protons) are ejected from reactions at an angle to the beamline they move across these magnetic field lines thus experiencing a centripetal force that brings them back to the beamline. If viewed from one end of the spectrometer this appears to be a circular path. However, because the particle is also moving along the beamline the resulting motion is a spiral.

The Lorentz equation can be used to predict the position at which a particle will return to the beamline by substituting the equation for a centripetal force ($F = \frac{mv_{\perp}^2}{r}$), along with $v_{\perp} = \omega r$ and $\omega = \frac{2\pi}{T_{cyc}}$, into Eq.3.1 to yield

$$T_{cyc} = \frac{2\pi m}{q|\boldsymbol{B}|} \tag{3.2}$$

The cyclotron period (T_{cyc}) can be used to predict the position (z) where the light particle will return to the beamline as $z = v_{||}T_{cyc}$, where $v_{||}$ is the particle velocity parallel to the beamline. The velocity parallel to the beamline depends upon the energy and reaction angle of the light particle. Thus, by using an coaxially mounted array of position-sensitive silicon detectors, the position and energy of the ejected light particles can be measured and used to calculate the reaction angle of that particle and the energy level through which the reaction

proceeded. This description is an idealised scenario to illustrate the general operating principles of the HELIOS spectrometer and is complicated, for example, by the fact that the detector array has real volume, which means particles are detected before they have fully returned to the beamline. For a more physical description see Chapter 3.1.2 and Ref.[83, 84].

As HELIOS operates in inverse kinematics, nuclei recoiling from reactions carry away most of the energy and continue down the solenoid at small angles to the original beam axis. These are stopped at the end of the solenoid by a silicon telescope which measures the ΔE-E of each ion [85], allowing each isotope to be identified. Subsequently these recoil measurements can be used to place a coincidence gate on the data and improve the signal-to-noise ratio of a given experiment.

3.1.1 Coaxial Detector Array

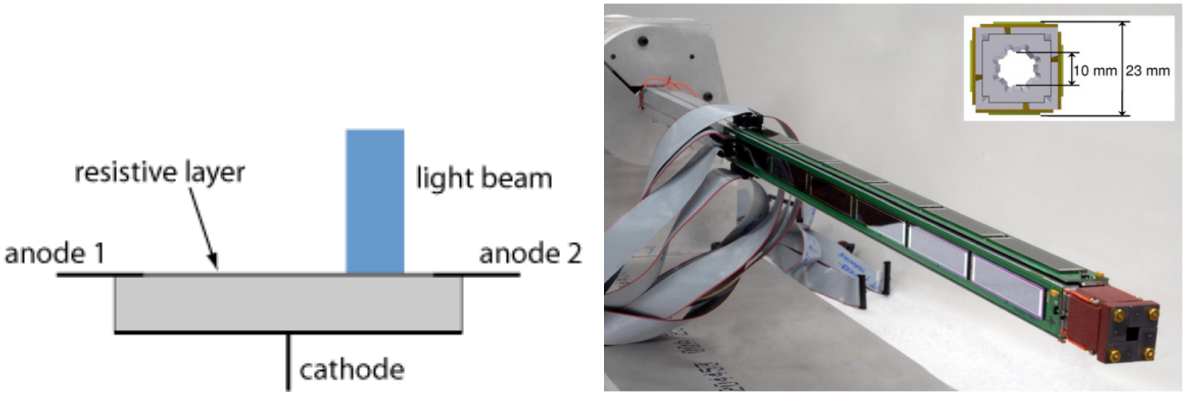

Figure 3.2: Left) A simplified diagram of a position-sensitive silicon detector [86]. Right) The coaxial array of position-sensitive silicon detectors used in HELIOS [83].

The coaxial detector array consists of twenty-four position-sensitive silicon detectors with six mounted on top, six below and six to either side of a long hollow box which surrounds the beamline; an image of the array can be seen in Fig.3.2. It is positioned upstream of the target so as to measure low centre-of-mass angles. Each detector is a silicon semiconductor and is sensitive to position in one dimension (along the beam axis). The diagram in Fig.3.2 shows how an individual position sensitive silicon detector is designed. While the base is connected to one cathode there are two anodes on the face of the detector, one at either end. When a particle (e.g. a proton) impinges upon the detector it deposits its energy through electromagnetic interactions with the semiconducting material. These interactions excite electrons in the silicon into the conduction band, thus allowing electrons and holes to flow. The number of charge carriers liberated is proportional to the energy of the incident particle. Charge flows out of the detector

via the two anodes and the proportion of the total charge measured by each output for a single event is determined by the relative distance between the two anodes that the charged particle impinged upon the detector. Thus, detection position can be measured along with the total energy of the incident particle.

When fabricating a detector, intrinsic semiconductors like silicon are *doped*. This is a process where by atoms of other elements are added in order to improve the electrical conductivity of the detector. The are two types of doping: n-doping (negative-doping), which introduces atoms that act as electron donors, and p-doping (positive doping), which introduces atoms that act as electron acceptors. These silicon detectors contain regions of n- and p- doped silicon, the boundary between which is called the p-n junction. At the p-n junction, electrons from the n-doped region diffuse into the p-region, forming what is known as a depletion region. On the p-doped side of the depletion region, the electrons combine with holes to produce negatively charged ions. On the n-doped side, the positively charged ions that donated those electrons remain. The p-n junction stabilises once a sufficient number of electrons have diffused into the p-region to repel addition electrons from diffusing.

When used in a nuclear physics experiment, a semiconductor detector is placed under reverse bias, a state where an external voltage has been applied to the detector such that the electrons and holes are drawn away from the p-n junction and thus the width of the depletion region is expanded. Under these conditions, the electrons released by incident radiation will flow towards the n-doped region, and the holes towards the p-doped region. Biasing reduces the flow of *leakage current*, the current that naturally flows across the detector which is mostly caused by thermal generation of electron-hole pairs, therefore improving the signal-to-noise ratio of a detector.

3.1.2 Conversion from (e,x) to (E,z)

Based on the position along z that a light particle is detected by the coaxial array and the amount energy it deposited the centre-of-mass angle of the reaction and the energy level through which the reaction proceeded could be calculated. As mentioned in Chapter 3.1, the equation to convert position in z to θ_{cm} is not as simple as $z = v_{||}T_{cyc}$. Owing to the presence of the coaxial detector the light particles have not completely returned to the beamline when they are detected since the array has real volume. To resolve this, a correction can be made to the equation for the time period ($T_{\mathrm{cyc}} = \frac{2\pi r}{v_{\perp}}$). As the full cycle is not complete, the full 2π angle must be replaced with $2\pi - 2\alpha$ where $\alpha = \arcsin(\frac{r_0}{2r})$. This relationship is derived from the

diagram in Fig.3.3 and is used to produce

$$z = (v_0 \cos(\theta_{cm}) + V_{cm}) \frac{r[2\pi - 2\arcsin(\frac{r_0}{2r})]}{v_0 sin(\theta_{cm})} \tag{3.3}$$

Which is the calculation for z, where the detector array radius is $r_0 = 11.4\,\text{mm}$ and r is the radius of the orbit of the proton. v_0 is the velocity of the proton in the centre-of-mass frame (which depends on its emission energy), V_{cm} is the velocity of the centre-of-mass frame in the laboratory and θ_{cm} is the centre-of-mass reaction angle. The substitutions for $v_\perp$ and $v_{||}$ can be found in Ref.[84].

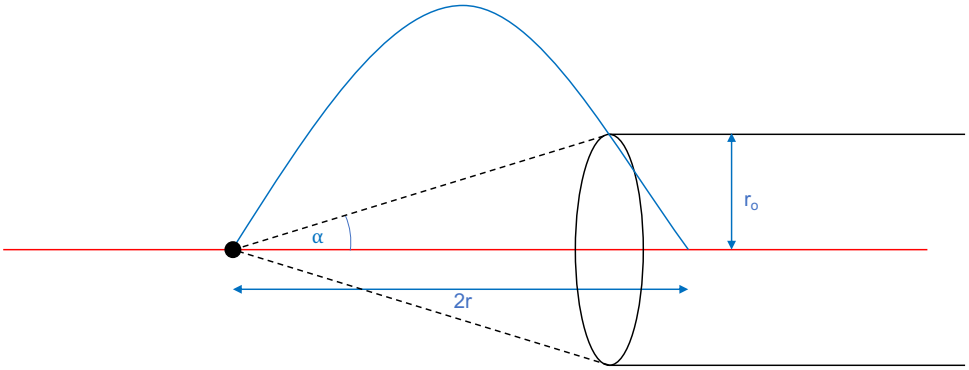

Figure 3.3: A diagram of the HELIOS detector array illustrating the correction to the cyclotron period. The black cylinder is the coaxial array, the red line represents the beamline and the blue line is the trajectory of the recoiling protons.

The measured energy of a light particle depends on the energy level through which the direct reaction proceeded. Because position in z is determined by both reaction angle and the excitation energy of the state each detector corresponds to a different angular range for each energy level in the recoiling heavy ion. To perform calculations with Eq.3.3, *Heliosmatics (v14)* [87] was used. This spreadsheet was also used to calculate the solid angle that each detector subtended.

3.1.3 Recoil Detector

The recoil detector is circular and divided into four segments. Each segment consisted of two layers of silicon. The surface layer is 80 μm thick and measures the energy loss of a recoil as it passes through (ΔE). The backing layer is 500 μm thick and stops the recoiling ion, measuring the residual energy. By measuring ΔE–E, the proton number and mass number of a recoiling nucleus can be identified. The ΔE of a recoil is associated with the proton number of that recoil through a classical particle identification technique known as the *Bethe-Bloch formula*, which

models the average energy loss of a nucleus as it moves through matter, the non-relativistic version of the Bethe-Bloch formula takes the form of

$$-\frac{dE}{dx} = \frac{4\pi N_a Z_t \rho_t Z^2}{A_t M_u m_e v^2}(\frac{e^2}{4\pi\epsilon_0})^2 \ln(\frac{2m_e v^2}{I}) \tag{3.4}$$

Z_t is the atomic number of the target, A_t it the nucleon number of the target, ρ_t is the target density, Z is the charge of the recoiling nucleus, v is the velocity of the recoil and I is the effective ionisation energy. The constants m_e and e represent the mass and charge of an electron, respectively; N_A is Avogadro's number and M_u is the molar mass constant. Eq.3.4 illustrates the Z^2 dependency of the energy loss. The energy deposited in the thin layer of silicon provides the ΔE measurement. The rear layer of silicon in the HELIOS recoil detector is thick enough to stop the recoils altogether and thus measures the residual energy. Thse measurements can be used to determine nucleon number of a recoil (A) and so ΔE–E allows for the identification of different recoiling isotopes.

3.1.4 Experimental Setup

For the ^{20}Ne(d,p)^{21}Ne experiment the ^{20}Ne beam energy used was 11 MeV/u (for a total beam energy of 220 MeV in the laboratory frame) and the magnetic field strength was set to 2T. The silicon telescope was in use to measure the ^{21}Ne recoils and the ejected protons were detected by the position sensitive coaxial array. The coaxial array was positioned to cover an angular range of 10° – 35° in the centre-of-mass frame (96° – 143° in the laboratory frame) for nuclei recoiling with excitation energies of 7.5–8.0 MeV. The target used was deuterated polyethylene with a thickness of 50 μgcm^2. The luminosity monitor (Elum) was not in use during this experiment. The Elum is a silicon semiconductor that detects elastically scattered ions, allowing the beam intensity to be monitored throughout the experiment.

3.2 Data Analysis

3.2.1 Position Calibration

The information on the recoil angle of a light particle and the excited state through which the direct reaction proceeded was extracted from the raw data collected by the spectrometer, measured by the number of charge carriers liberated in a single event and the position at which each event occurred. These charge carriers were collected by the two anodes at either end of each silicon strip in the coaxial array, with the sum of the two signals being the total size of

the signal (e) registered for a single event. Here, x_f is defined as the size of the signal collected by the upstream anode and x_n is the size of the signal collected by the downstream anode. The position of an event on the detector was determined by the relative current induced on the upstream and downstream anodes (cf. Chapter 3.1). The first step in the data analysis was to use these two measured signals to compute the position each event occurred at on a given detector and began by gain matching the detectors for x_f and x_n. Gain is a term describing the process of multiplying the number of electrons measured by the detector for each event. Applying detector gain is necessary since the raw number of counted electrons, e, in any detector is very small and must be amplified so that a data acquisition unit (DAQ) can handle it. Note that each detector needed to be treated individually as each had a slightly different response.

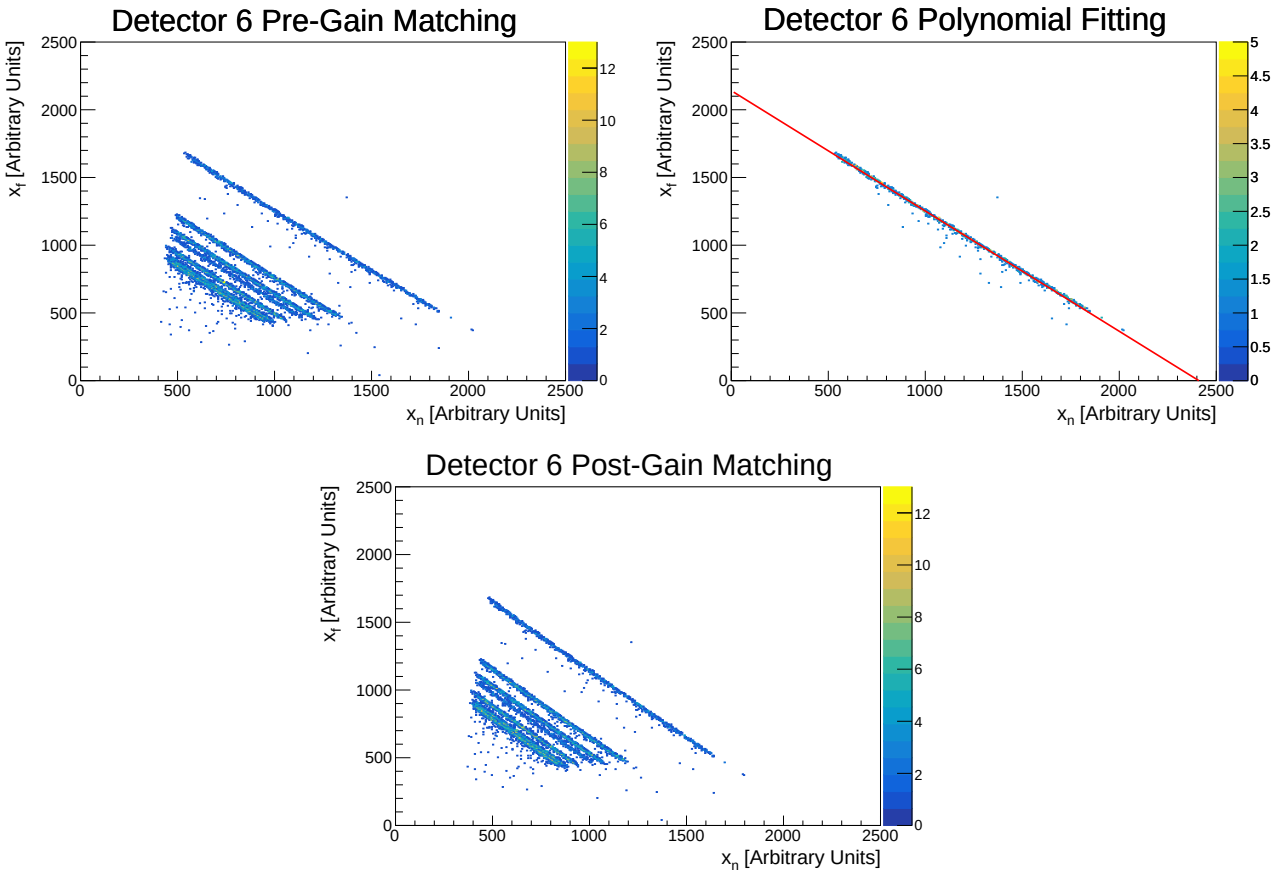

Figure 3.4: The process of gain matching the position-sensitive SSBs in HELIOS. x_f denotes the signal collected by the upstream anode and x_n, the downstream anode. The χ^2 value of the fit shown is 29.1351.

A ^{228}Th source was placed in the target position and calibration data were collected; this is a radioactive source that emits alpha particles at a several well known energies as the nucleus passes down the ^{228}Th decay chain, specifically the 5.388 MeV, 5.432 MeV, 5.685 MeV,

6.050 MeV, 6.288 MeV, 6.778 MeV and 8.785 MeV lines. A plot of x_f vs x_n, such as is shown in Fig.3.4, was made for each detector and on these plots the alpha particles emitted by the source could been seen. The alpha particles are the straight lines with a negative gradient, each line corresponding to a specific emission energy. For each of these lines $x_f + x_n = k$, where k is a constant and each should intercept the x- and y-axis at values of $x_n = k$ and $x_f = k$, respectively, when they are correctly gain matched. It can be seen from the fit in Fig.3.4 that this is not the case in the raw data and that had to be corrected. One of the lines associated with an emitted alpha particle was isolated and fitted with the function

$$x_f = Bx_n + k \tag{3.5}$$

This determined the correction B that was needed to match the gain in the upstream and downstream anodes. Here, $x'_n = Bx_n$ was defined for later use. The B parameter was then used to make a plot of e vs $x'_n + x_f$ and once more a first order polynomial was fitted, using the equation

$$e = C_1(x'_n + x_f) + C_0 \tag{3.6}$$

The constants C_1 and C_0 were then used to define the following terms

$$x'_f = C_1 x_f + C_0 \tag{3.7}$$

$$x''_n = C_1 x'_n + C_0 \tag{3.8}$$

At this stage the gain matching was complete and $e = x'_f + x''_n$. The relative position on a single detector ranges from $(-1, 1)$ and is defined by

$$x = \frac{(x'_f - x''_n)}{e} \tag{3.9}$$

This was then converted to an absolute position in z (distance along the beam axis) with

$$z = d(\frac{x+1}{2}) + p \tag{3.10}$$

Where d is the length of the single detector and p is the position of the leading edge of that detector. Once z had been calculated, the absolute distance along the beam axis for the interaction of each proton was known.

Now turning to the proton data from the ^{20}Ne(d,p)^{21}Ne experiment, Fig.3.5 shows raw

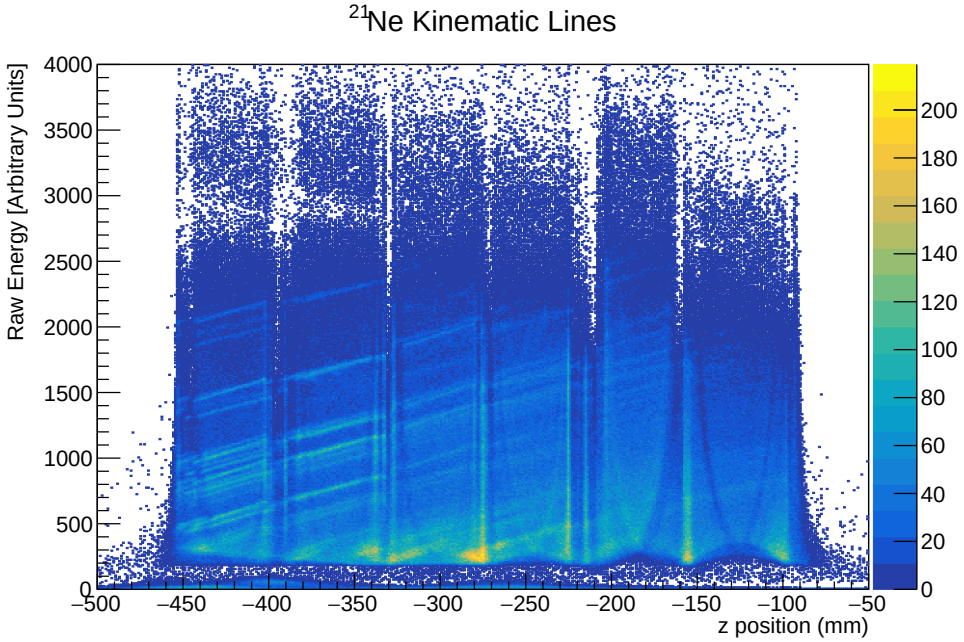

Figure 3.5: Raw energy vs z position from the ^{20}Ne(d,p)^{21}Ne experiment.

energy measured by the detectors plotted against position along the beamline, z. Note the six distinct sections show clearly the six different detector positions along z. Already the excited states of ^{21}Ne can be seen. These are the straight lines that are continuous across multiple detector positions, their angle to the beam axis comes from the kinematics of the reaction. The next step was to calibrate the energy registered by each detector.

3.2.2 Energy Calibration

Before the raw spectrum could be plotted for calibration, a correction had to be made for a kinematic effect that arose from the motion of the beam nuclei as they reacted with the target deuterons. This effect resulted in the kinematic lines of the ^{21}Ne excited states appearing at an angle on Fig.3.5. To perform the correction, another first-order polynomial was fitted to an isolated kinematic line. Isolating these lines is easiest when they are clearly separated from one another, however, as can be seen in Fig.3.5, in these data they were not. There was a significant background which could be cleaned up using the recoil detector at the end of HELIOS as a coincidence gate.

Coincidence gating set a condition that after a proton was detected in the coaxial array, a recoiling ion must be detected within a given time frame otherwise the proton event would be vetoed. In this work, the time gate required a recoil be measured within 8 μs of a proton, which based on kinematic calculations was a sufficient time for the associated recoils to reach

the detector. Furthermore, the proton and neutron number of each recoil could be identified by $\Delta E - E$ analysis. This allowed an additional gate to be set such that only protons in coincidence with specific recoiling nuclei were included in the analysis, specifically: ^{21}Ne, ^{20}Ne and ^{17}O. By gating on these recoils, it was possible to isolate an individual excited state so that the necessary correction for the beam kinematics could be determined. The process of doing this is illustrated in Fig.3.6. The polynomial fitted is $e' = D_1 x + D_0$ and the two constants D_0 and D_1 are different for each detector. Once this step was complete the proton energy spectrum could be plotted.

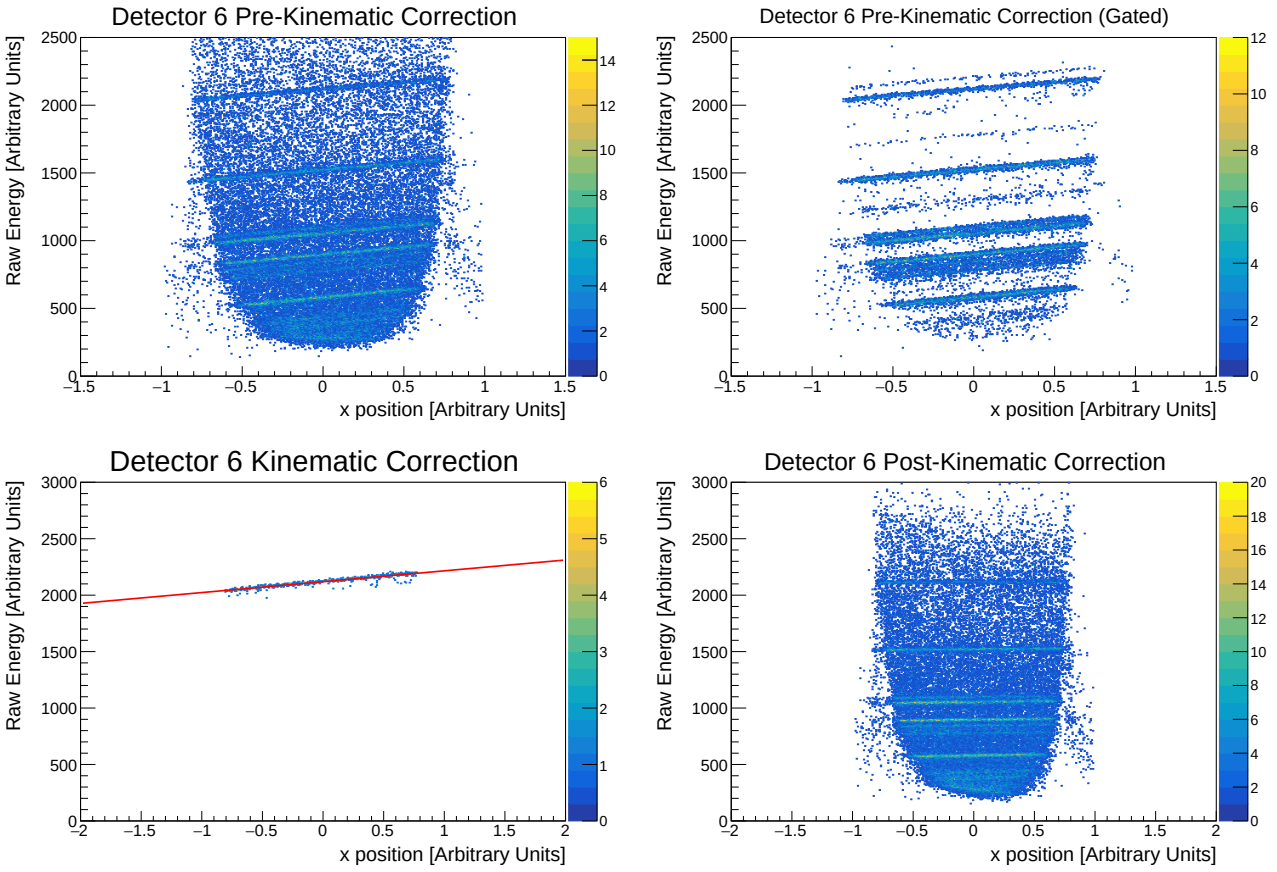

Figure 3.6: A comparison of detector 6 before and after the kinematic correction, the first order polynomial fit to one of the energy levels after the background has been removed by gating on the recoils, the associated χ^2 value is 6.2791.

3.2.2.1 Internal Calibration

The value of e measured by the detectors represents the size of the detected signal when a proton was stopped in the detector. e is proportional to the kinetic energy of the detected proton which could be used, along with z position, to calculate the energy of the excited state

in ^{21}Ne through which the reaction proceeded and the reaction angle. e was converted directly to excitation energy by an internal calibration.

An internal calibration plots the e spectrum and compares it to an excitation energy spectrum from literature; identifying the most prominent peaks and using these as reference points for a calibration. The precise position in e was determined by fitting Gaussian functions to each peak and taking the centroid value. A plot of measured e vs literature E_x was then made to graphically relate the two parameters and a linear function was fit. This fit is the calibration function.

A summary of which peaks were used in the calibration for each detector in this work can be found in Table 3.1. Ideally the same set of energy levels would be used in the calibration of each detector. However, this was not possible due to variation in the resolution of individual detectors, which led to the energy levels on some detectors overlapping and making it impossible to reliably identify the e position of the two peaks.

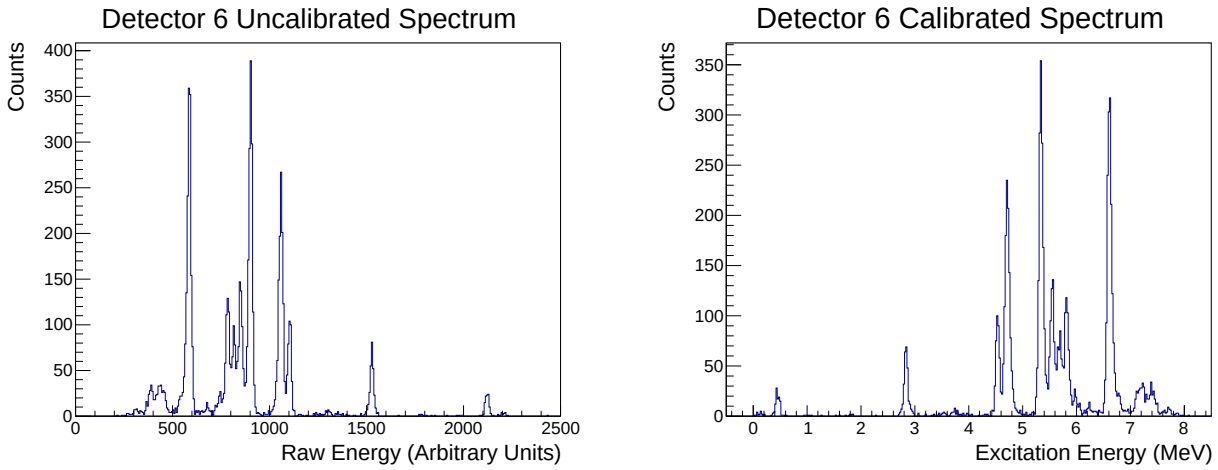

Figure 3.7: Proton energy spectrum from detector 6 before and after energy calibration and the polynomial used to transform between the two. The apparent difference in counts is a function of binning which results from the x-axis being slightly wider in the uncalibrated plot.

Once the plot of E_x vs e had been made using all available points of comparison, a linear function was then fitted to the data. This process is illustrated in Fig.3.7 on which it can be seen that detector 6 provided a high resolution data set with narrow peaks leading to a calibration with a low uncertainty. The calibration itself is shown in Fig.3.8. Uncertainty in the calibration was determined by calculating the standard deviation of the data points from the linear fit for each detector.

With the excitation energy spectra calibrated, the analysis could move onto the next stage: peak fitting. Note that by converting from e to E_x, the spectrum was reflected through the

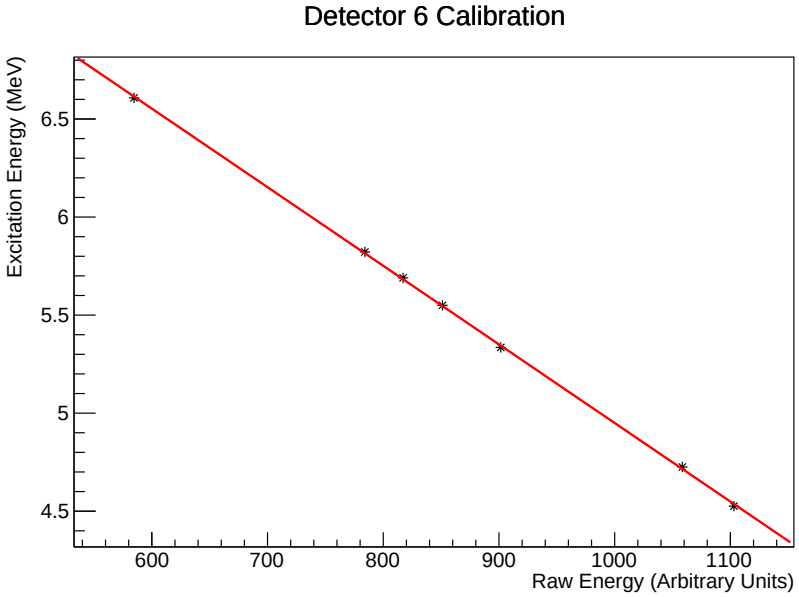

Figure 3.8: The polynomial used to calibrate detector 6, producing the transformation shown in Fig.3.7. This calibration has χ^2=0.000458.

y-axis because the higher energy protons originated from the lower energy levels deeper in the nuclear potential well.

An internal calibration was used rather than calibrating with the ^{228}Th alpha source. Both options included states close to the region of astrophysical interest, but the internal calibration covered a range of energies that reached down to 4.526 MeV, whereas the alpha calibration only reached extended down to 5.388 MeV. Since it was desirable that the lower states in ^{21}Ne also be investigated, the internal calibration was chosen as the range of energies it included covered more of the excitation energy spectrum that was the aim of this study.

3.2.3 Peak Fitting

With the proton energy spectrum for ^{20}Ne(d,p)^{21}Ne calibrated and the relationship between detector position, ^{21}Ne energy level and reaction angle established, the next step was to extract the number of counts for each excited state at each angle. As there were six detector positions, the differential cross section for each excited state was measured at six different angles. In practice, however, not all detectors were used in the analysis of states above the alpha threshold. See Chapter 3.2.5.1 for a discussion on which detectors were used and why some were not. The excitation energy spectrum for each detector now displayed a series of peaks, each corresponding to an excited state in ^{21}Ne. The number of protons recoiling from a reaction that proceeded through a specific energy level in ^{21}Ne was determined by fitting a Gaussian function to its

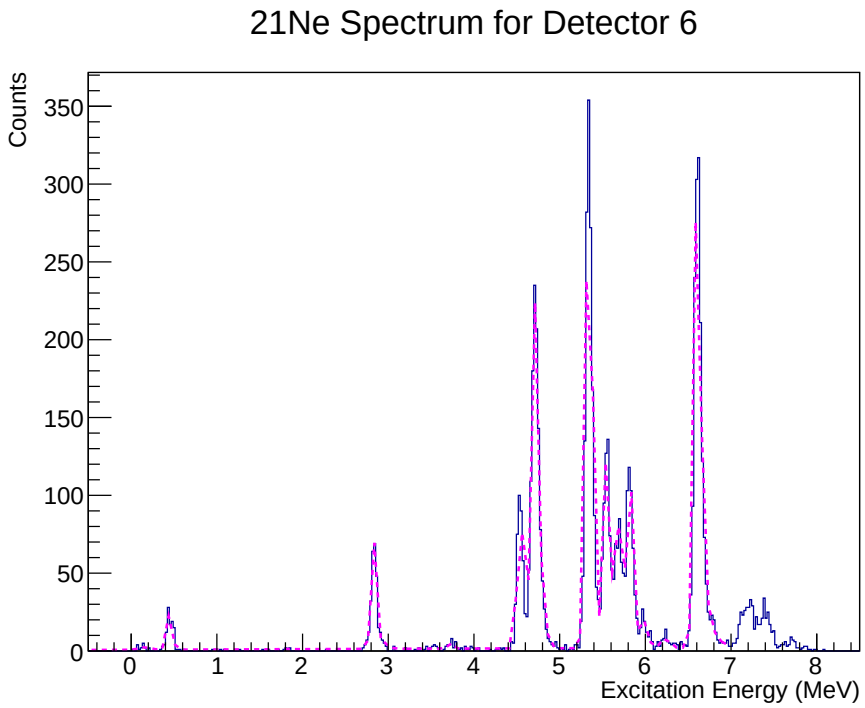

Figure 3.9: The proton energy spectrum for detector 6 fitted below the neutron threshold. Note that this is shown here as an example of a full range fit. A more detailed plot showing similar fits zoomed in on the higher energy region can be found in Fig.3.16 and include the individual contributions from each state. $\chi^2 = 131.14033$

respective peak on the energy spectrum and calculating the area underneath. In practice none of the energy levels were completely isolated and overlapped with other levels of various strengths. When fitting therefore, the function used is a sum of several Gaussian curves, one for each energy level. Background protons are often accounted for by fitting a polynomial function to the spectra, however, this was not done here as the background can be seen to be negligible in comparison to the height of the main peaks on Fig.3.9. The software used to perform the spectrum fitting in this experiment was ROOT [88]. The equation

$$P(x) = \frac{\Lambda}{\sigma\sqrt{2\pi}} e^{-(x-\mu)^2/2\sigma^2} \tag{3.11}$$

Shows the version of the Gaussian function that was used to fit the peaks, with Λ, μ and σ as the area, centroid and width respectively. The most prominent peaks in the ^{21}Ne spectrum were below the neutron threshold and these are the peaks used in the internal calibration due to the low uncertainties in literature for their energies. An example of a full fit of the post-calibration spectrum can be seen in Fig.3.9.

Table 3.1: The states in ^{21}Ne below the neutron threshold used to calibrate the detectors.

ID	States used to calibrate (MeV)	Comments
0	6.608, 5.822, 5.550, 5.335, 4.725, 4.526	
1	6.608, 5.822, 5.550, 5.335, 4.725, 4.526	
2	6.608, 5.822, 4.725	
3	6.608, 5.550, 5.335, 4.725, 4.526	
4	6.608, 5.335, 4.725, 4.526	
5		Not working
6	6.608, 5.822, 5.690, 5.550, 5.335, 4.725, 4.526	
7	6.608, 5.690, 5.550, 5.335, 4.725	
8	6.608, 5.822, 5.690, 5.550, 5.335, 4.725, 4.526	
9	6.608, 5.335, 4.725, 4.526	
10	6.608, 5.335, 4.725	
11		Not working
12	6.608, 5.822, 5.550, 5.335, 4.725, 4.526	
13	6.608, 5.822, 5.690, 5.550, 5.335, 4.725, 4.526	
14	6.608, 5.550, 5.335, 4.725	
15	6.608, 5.550, 5.335, 4.725, 4.526	
16		Not working
17	6.608, 5.335, 4.725, 4.526	
18	6.608, 5.822, 5.550, 5.335, 4.725, 4.526	
19	6.608, 5.822, 5.550, 5.335, 4.725, 4.526	
20	6.608, 5.335, 4.725, 4.526	
21	6.608, 5.335, 4.725, 4.526	
22	6.608, 5.335, 4.725	
23	6.608, 5.550, 4.725	

3.2.4 Recoil Identification

3.2.4.1 Shift in Recorded Recoil Energy

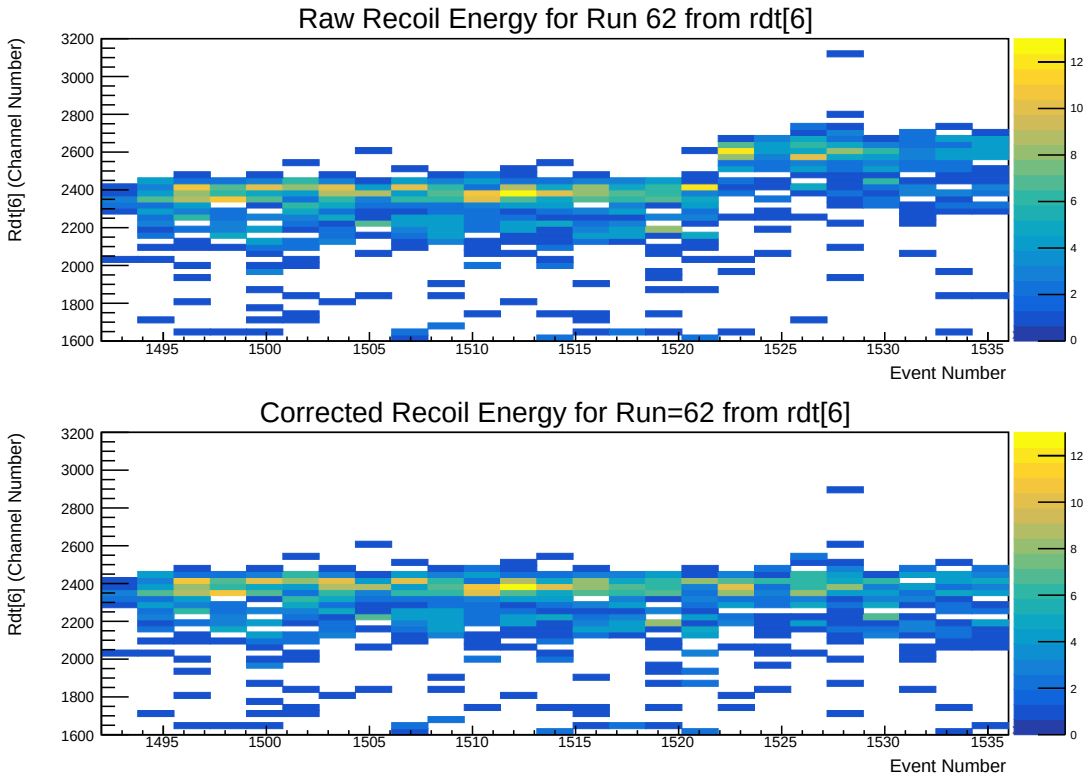

Figure 3.10: Recoil E vs event number (time) for recoil detector rdt[6], zoomed in on the region where the leakage current change took place. Top) before recorded energy correction. Bottom) after the recorded energy correction.

As mentioned in Chapter 3.2.2, the recoiling nuclei could be used to set a gate on the data, thus removing background events to leave only those associated with the ^{20}Ne(d,p)^{21}Ne reaction. Gating was done by plotting graphs of ΔE vs E and identifying the loci of the recoils. One issue encountered was an observed change in the leakage current that occurred partway through the experiment. Leakage current is the current that naturally "leaks" across the band gap of the semiconducting silicon. The change in leakage current was correlated with a shift in the E value measured by the recoil detectors and had to be accounted for by making a correction to the recorded data. The origin of this shift is uncertain; it could be that a change was made to the gain of the detectors midway through the experiment. No change was logged, however, since the change is discontinuous, it is likely the result of human intervention. This experiment was conducted during the coronavirus pandemic and was largely remotely attended. The reduced number of on-site staff did, understandably, impact communication over the course of the experiment; it is possible that this is one such example.

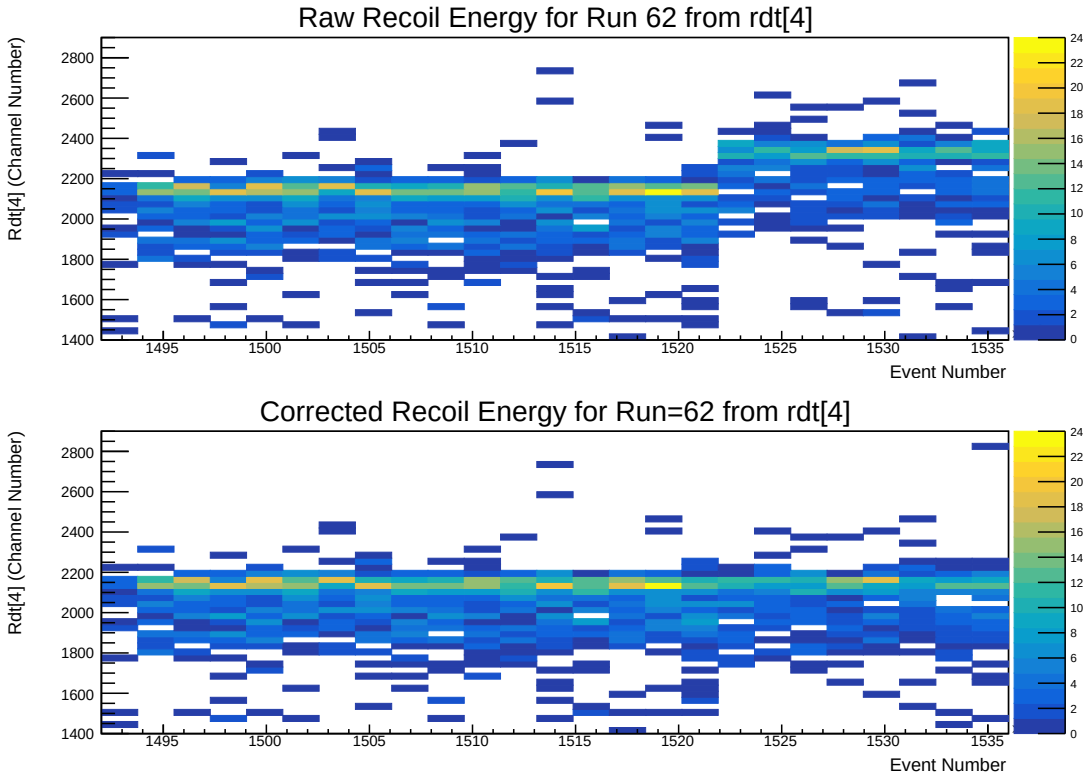

Figure 3.11: Recoil E vs event number (time) for recoil detector rdt[4], zoomed in on the region where the leakage current change took place. Top) before the correction for the shift in recorded recoil energy. Bottom) after the correction for the shift in recorded recoil energy.

The correction made to the recoil data was linear and had a magnitude calculated from plots of E vs time for each of the four recoil segments. The precise time at which this shift occurred could be identified by finding the discontinuity on these plots. E should be constant in time, therefore by fitting a straight line either side of the shift the measured energy was determined both before and after the leakage current shift and the difference between these values was the necessary correction. Fig.3.10 shows the energy vs time plot before and after the correction was made for one of the recoil detectors (rdt[6]); the plot is zoomed in on run

Table 3.2: The recoil detector corrections for the shifts in recorded energy.

Recoil Detector	Correction (channel number)
rdt[0]	-135.2(37)
rdt[2]	n/a
rdt[4]	-190.1(24)
rdt[6]	-217.0(42)

62, during which the leakage current shift took place. Fig.3.11 shows the same plot, this time for the rdt[4] detector, illustrating that this change was observed in multiple recoil detectors. Correcting for this shift was necessary otherwise the inconsistent E value for the recoils made it impossible to set appropriate gates based on the recoils, as the shift in E resulted in some overlap between the ^{21}Ne and ^{20}Ne loci on the particle identification plots. The shifts varied for each detector and their corrections are listed in Table 3.2.

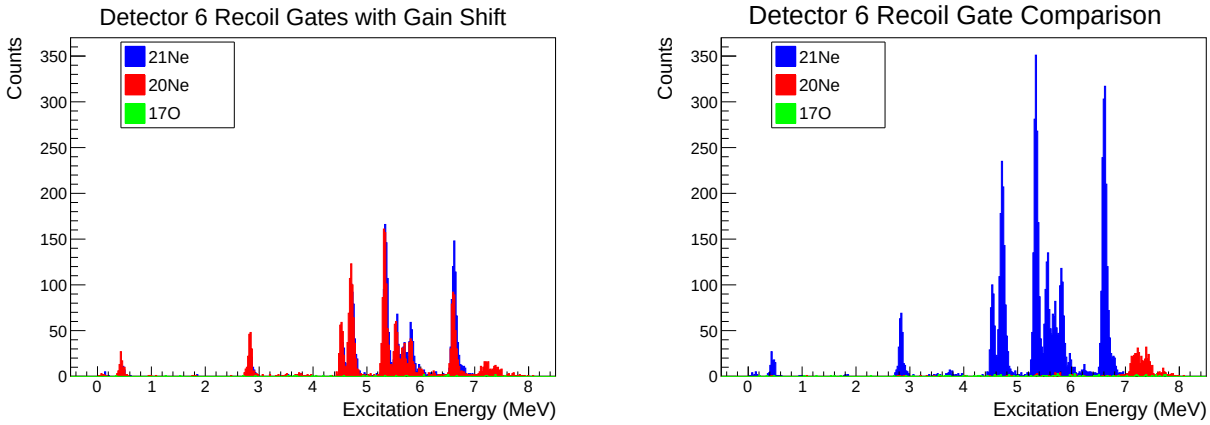

Figure 3.12: The excitation energy spectrum from detector 6 when gating on different recoils (^{21}Ne, ^{20}Ne and ^{17}O) both before and after the correction for the shift in recorded energy. Left) before correction. Right) after correction.

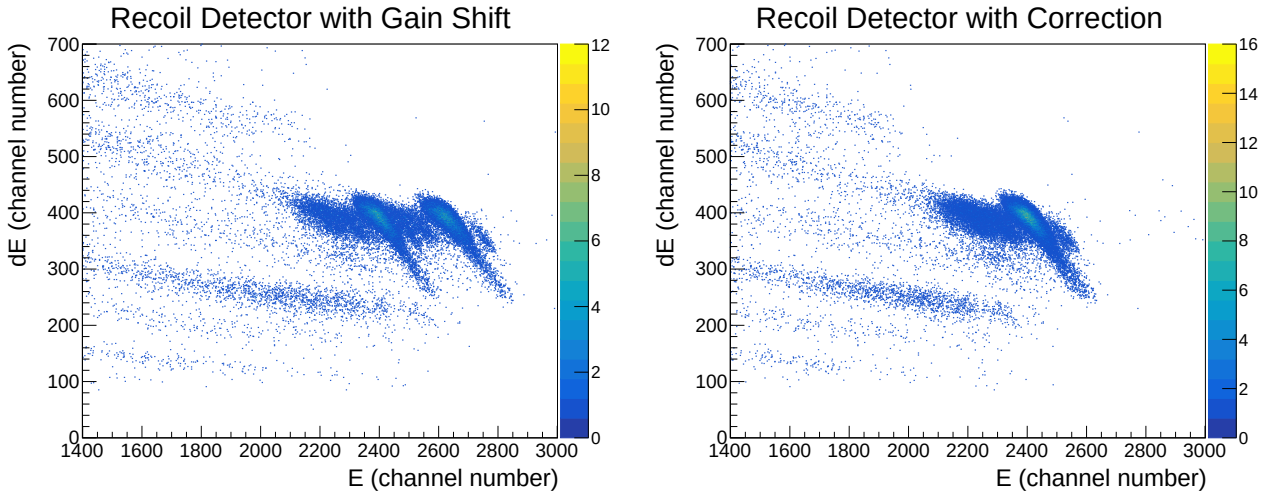

Figure 3.13: Particle ID plots before and after the correction for the shift in recorded recoil energy. Left) before correction. Right) after correction.

A comparison of the plots on Fig.3.12 illustrates the importance of this correction for the recorded recoil energy as the ^{20}Ne gate clearly shows data from ^{21}Ne is being included in the

cut, despite having attempted to gate on only ^{20}Ne. Gating on ^{20}Ne should exclude data below the neutron threshold, which is at 6761 keV. The post correction plot no longer displays this behaviour, indicating the shift in recorded recoil energy was indeed the reason for the overlap. The ΔE–E plots shown in Fig.3.13 show the effects of the shift in recorded recoil energy on the measurements made with the recoil detectors.

3.2.4.2 Recoil Gates

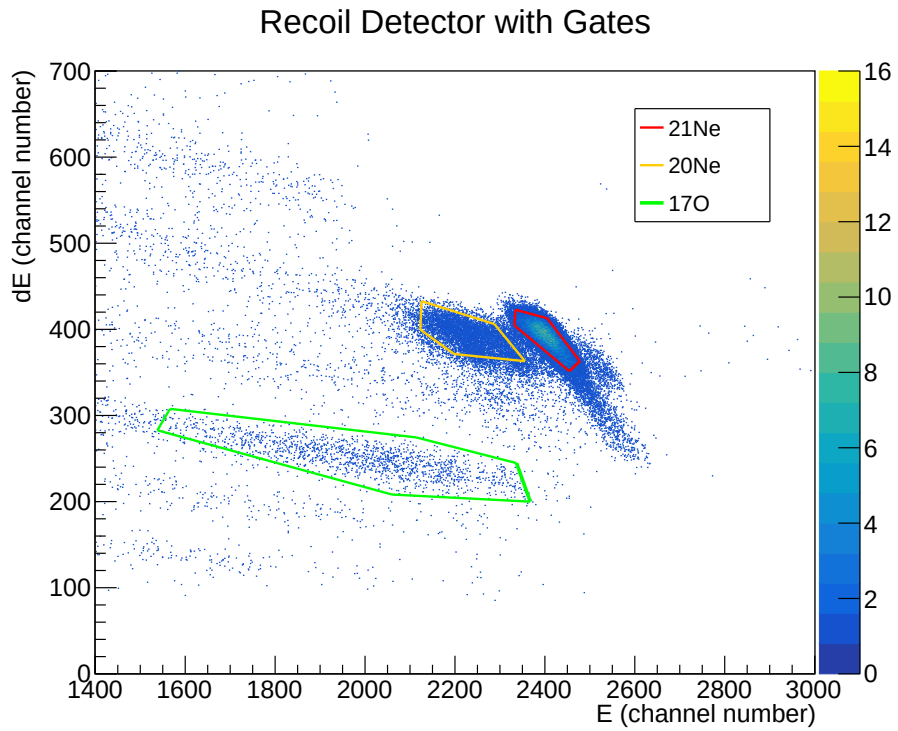

Figure 3.14: The recoil gates for each nucleus studied for the rdt[6] vs rdt[7] detectors.

Fig.3.14 shows the recoil gates used for the three isotopes of interest to this experiment. Each locus on this plot corresponds to a different isotope being measured by the recoil detectors. The red gate is ^{21}Ne, orange is ^{20}Ne and green is ^{17}O (from the ^{20}Ne(n,α)^{17}O channel). These gates were made tight to minimise any random background events in the spectrum. Fig.3.15 shows a close up of the spectrum, plotted using the recoils for each gate and illustrates that by gating on these loci the background became negligible.

3.2.5 Spectrum Fitting

By fitting Gaussian functions to the excitation energy spectrum of each detector, the yield for excited states at several different angles could be found. The yield needed to be corrected for

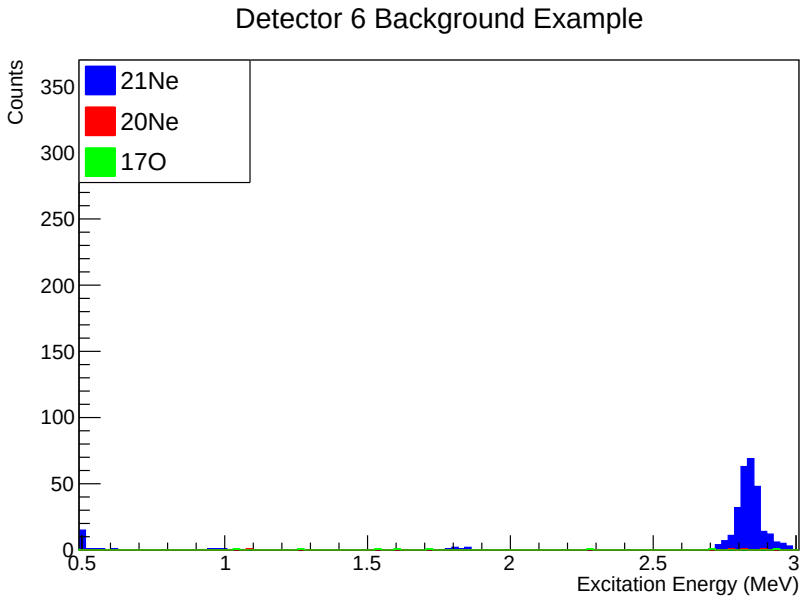

Figure 3.15: The excitation energy spectrum for detector 6, zoomed in on a region of background.

statistical binning and the solid angle coverage for each detector had to be included to allow comparison. Each detector was positioned at a different distance along z and therefore a proton must travel further to reach some detectors than others. Conceptualising these distances as the radius of a sphere, one can see that the solid angle of detectors at different positions are not the same. Calculating the solid angle coverage was done using *Heliosmatics* [87], as mentioned in Chapter 3.1.2. Once these corrections had been made, graphs of counts vs angle for each energy level could be plotted by normalising the solid angle for each detector to that of one position. The position chosen for normalisation was the same for all levels studied and was position 1 (which covered detectors 1, 7, 13 & 19).

The width of a peak in one of these spectra is a fixed value (not allowed to vary in the fitting) calculated by combining the resolution of each detector (determined with the method discussed above) and the total width of that energy level. As this experiment was conducted in inverse kinematics detector resolution dominates the measured width, so the width of a level could be considered negligible unless it was larger than the detector resolution and all of these states produce narrow resonances. The resolution for each detector was determined by fitting the strong states below the neutron threshold, allowing the width and height of the Gaussian peaks to vary freely, and taking an average of the resulting σ from the Gaussian fits, the results are shown in Table 3.4. Determining the resolutions was useful in the fitting of states in the energy range of interest above the neutron threshold because the much lower statistics in this region required the fitting parameters to be constrained as much as possible. Calibration

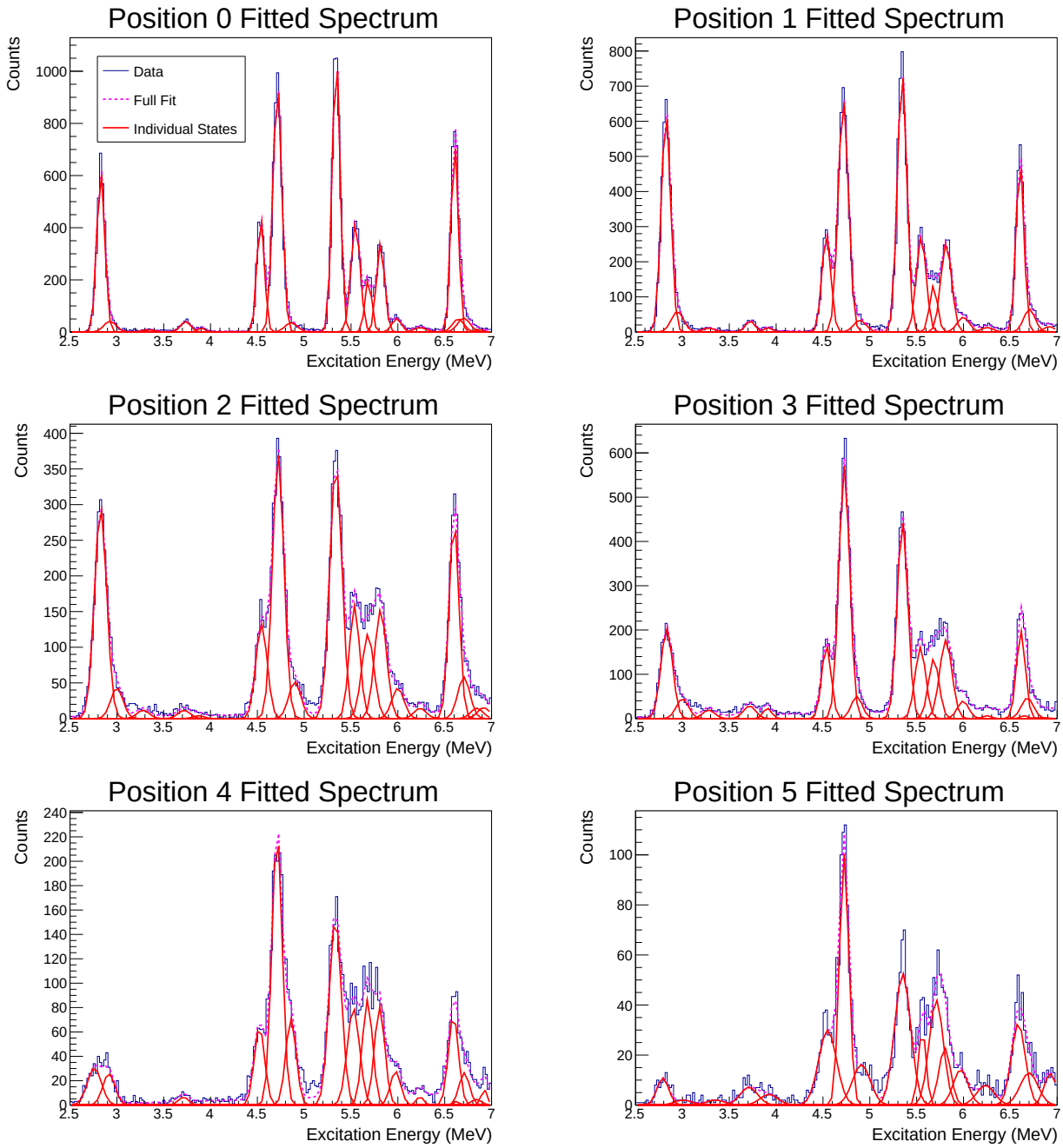

Figure 3.16: Fits for those strong states below the neutron threshold of ^{21}Ne. The dashed magenta lines indicates the overall fits and the red Gaussians are the individual peaks that contribute. These spectra combine contributions from different detectors at the same angle. For a list of which detectors are associated with which position, see Table3.4. χ^2 values for the fits to positions 0 to 5 are as follow: $\chi^2(0) = 233$, $\chi^2(1) = 264$, $\chi^2(2) = 322$, $\chi^2(3) = 288$, $\chi^2(4) = 263$ and $\chi^2(5) = 176$.

uncertainty (calculated as explained in Chapter 3.2.2.1) was used to constrain the centroid of each energy level above the neutron threshold by commuting the calibration uncertainty with the uncertainties on the energies reported in Ref.[30].

Table 3.3: The energy levels used in fitting the ^{21}Ne proton energy spectrum above the alpha threshold and their literature source.

Energy level (keV)	Source
7108(1)	[89]
7176(1)	[89]
7337(1)	[89]
7420.4(15)	[30]
7559.1(15)	[30]
7619.9(10)	[30]
7748.8(17)	[30]
7820.1(15)	[30]
7981(2)	[30]
8069(1)	[30]
8189(2)	[37]

To extract out the counts for each state below the neutron threshold, the spectra from and the working detectors at a given position were summed. These combined position spectra were then fitted with the same states as was used in the fits to the spectra individual detectors. These fits are shown in Fig.3.16, zoomed in on the section of the spectra showing the peaks that were investigated in this study. In these fits below the neutron threshold, the centroid position was constrained as described above and the heights and widths were left to vary freely.

The fitting of the states above the neutron threshold was done separately to those below. There were several difficulties in analysing the data in this region: low resolution (from inverse kinematics), low statistics and the energy levels being narrowly separated in energy. These issues resulted in the peaks overlapping on the spectra and meant that when summing over all detectors at a given angle the uncertainty of the resulting fits was too high to allow any conclusions to be drawn from the data. The solution was to use only one detector from each angular position. Since resolution was the dominant problem, the detector with the best resolution was chosen to represent each position. Table 3.4 highlights which detectors were used for each angle and lists each the resolution of each detector. This approach sacrificed counts (statistics) in

order to improve the resolution of the spectra. Even with this approach the overlaps made it impossible to identify by eye the position of individual energy levels. Fortunately, there was a solution.

A ^{20}Ne(d,p)^{21}Ne experiment had previously been run in forward kinematics at TUNL [30]. While this experiment suffered from ^{17}O contamination that obscured states in the Gamow window, most of the energy levels in the region of interest could be seen clearly at several angles. For a comparison of the resolution of the two experiments, see Fig.2.2. As the TUNL experiment was conducted at a similar centre-of-mass energy to this study across a similar angular range, the results from the TUNL experiment could be used to inform the fitting of the HELIOS spectra. Therefore, the fitting procedure for the HELIOS data only included those peaks clearly seen in the TUNL experiment. Peaks that appear very small in the TUNL data were treated as negligible in the HELIOS analysis in an attempt to avoid over-fitting the spectra. A list of the peaks used in the fitting can be found in Table 3.3. Fig.3.17 shows the fitting produced when using the TUNL data to restrict the free parameters available for each of the detectors used. Note that no background polynomial was included because, based on Fig.3.12, background events are expected to have been sufficiently removed with the two gating conditions (coincidence time and recoil gate).

The fits above the neutron threshold, as shown in Fig.3.17, fixed the peak widths using the resolution of each detector and did not include any energy dependence. The justification for this was to prevent over-fitting of the spectra. The fits shown in Fig.3.17 also include states at 8068 and 8198 keV. The justification for this is that, while these peaks have been observed in previous studies [29], above 8068 keV the level density becomes too great for HELIOS to resolve and therefore a reliable investigation of these states in this experiment was not possible. Their inclusion in the fits (particularly the 8068 keV state) was necessary since they both overlap the 7820 keV peak and therefore needed to be included in the fitting, lest their omission increase the uncertainty of the 7820 keV fits. The 8068 keV state was reasonably well separated from the 7981 keV state.

3.2.5.1 Chosen Detectors

Unfortunately, the detectors corresponding to the lowest angles (position 0; detectors: 0, 6, 12 & 18) could not be used in the analysis of the levels above the neutron threshold since these detectors were on the very edge of angular acceptance of HELIOS. The spectra are cut off around 7.7 MeV, below the excited states of interest (those being 7749 keV and 7820 keV). This can be seen on the plot for detector six in Fig.3.17.

Fig.3.18 shows that the response of each detector was different. For instance, some detectors had better resolution and some had a greater uncertainty in their energy calibration; these

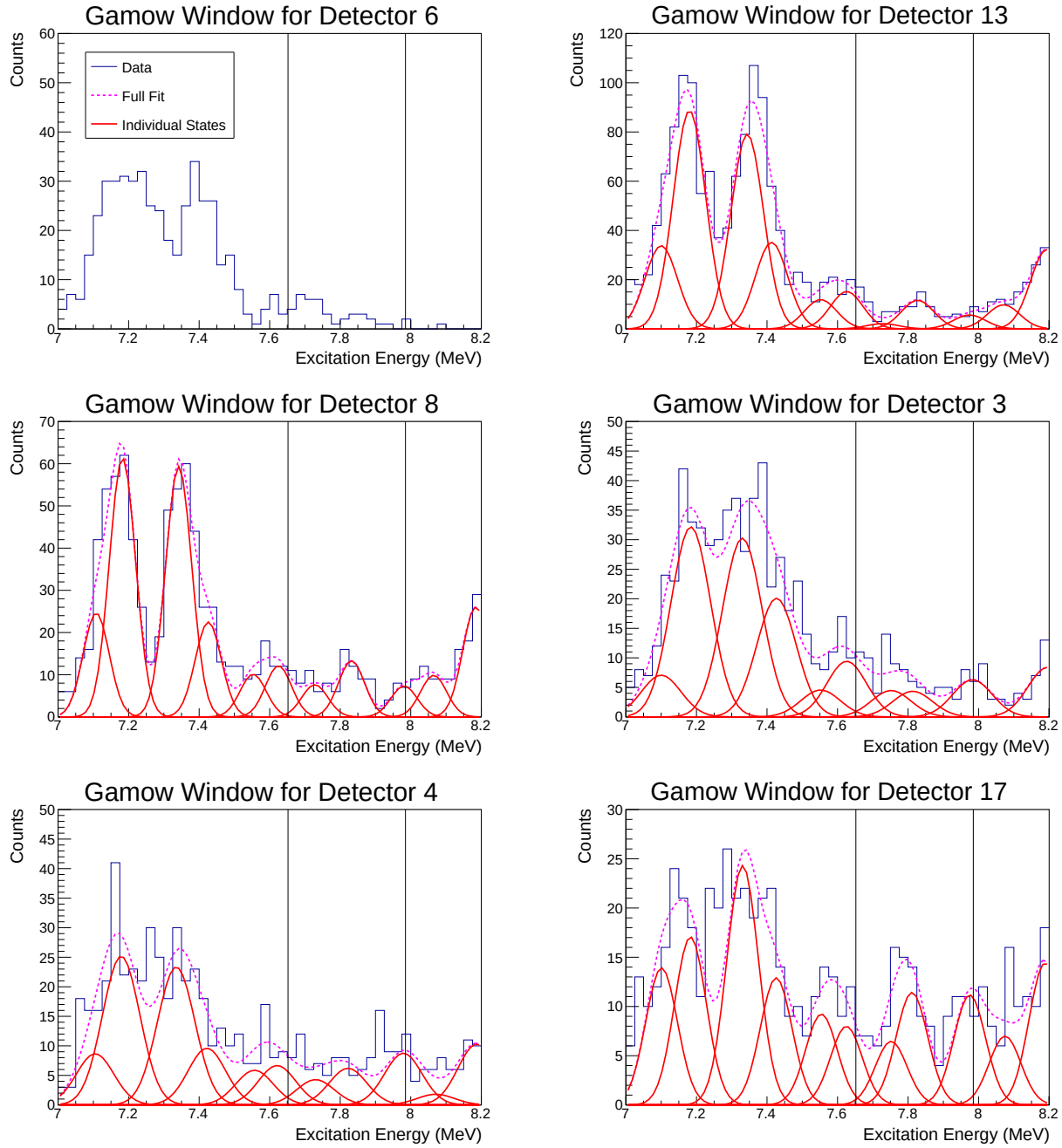

Figure 3.17: Fits of the excitation energy region of interest for each of the detectors used. The dashed magenta lines indicates the overall fits and the red Gaussians are the individual peaks that contribute. The two vertical black lines on each plot bracket the energy range of relevance for the *s*-process in rotating massive stars, which spans 7.65–7.99 MeV. χ^2 values for each detector fit shown are as follow: $\chi^2(6) = \text{n/a}$, $\chi^2(13) = 49.2$, $\chi^2(8) = 31.0$, $\chi^2(3) = 36.4$, $\chi^2(4) = 53.1$ and $\chi^2(17) = 41.4$.

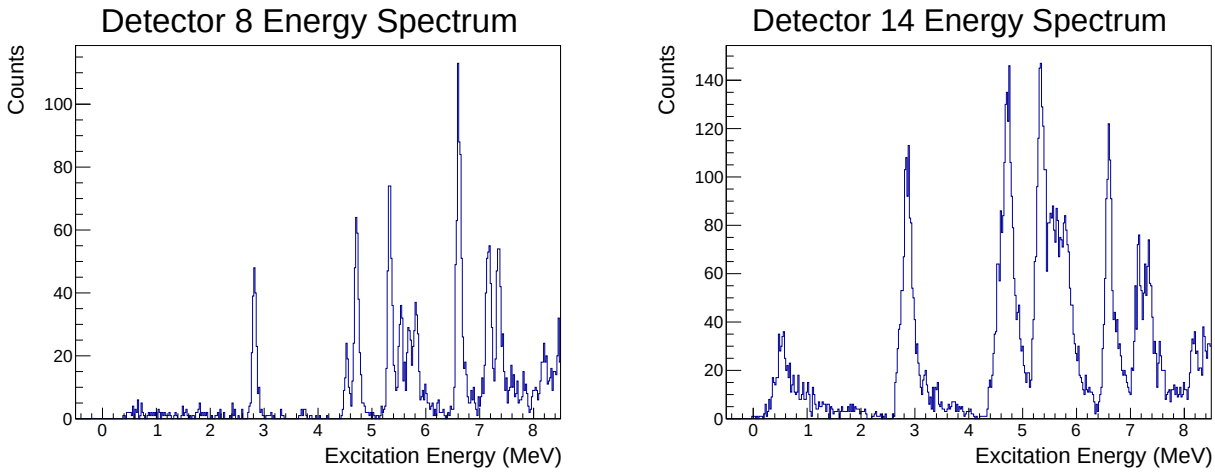

Figure 3.18: A comparison of detector 8 and detector 14, both of which at position 2 on the array, showing significant differences in resolution.

differences are summarised in Table 3.4. An additional problem was found in the positioning of the beam on the target. If the beam spot was off-centre it would result in one side of the array receiving a higher count rate than the others. When the data were tested it was found that there was indeed an asymmetry in the beam position. This asymmetry would not be an issue provided all detectors at a given position along the array were in use, however, this was not case. Those energy levels analysed below the neutron threshold took data from all detectors available, summing the spectra together to make a combined plot. However, as a number of detectors were not functioning during the experiment (cf. Table 3.4) the results at those angles would be affected by the beam position offset. In the case of the above threshold states, only the detectors with the best resolution were used meaning that once again, the beam position offset has to be accounted for when reporting results. This beam position offset was determined by evaluating the percentage contribution of each detector to the total counts at each position. This could only be calculated for positions where all detectors were functioning (positions 0,1 and 2). Taking the average of the standard deviations for each of these positions, the uncertainty in counts as a results of the beam offset for a given detector was calculated to be 10%.

3.2.6 ADWA Analysis

3.2.6.1 Potentials

Chapter 2.3 explained how differential cross section measurements are compared to DWBA predictions when determining the spin-parity of an energy level and the associated spectroscopic

Table 3.4: A summary of the detectors in the HELIOS coaxial array with their resolution calculated as an average of their measured sub-threshold widths.

ID	Position	$\sigma_{\text{calibration}}$ (keV)	Resolution (keV)	% total position counts	Comments
0	0	2.4	49	17.5	Acceptance limit
1	1	7.6	53	14.4	
2	2	1.7	70	21.0	
3	3	6.9	56	16.0	Used for analysis
4	4	0.7	53	n/a	Used for analysis
5	5				Not working
6	0	8.1	43	20.5	Acceptance limit
7	1	6.3	80	27.9	
8	2	6.1	37	14.7	Used for analysis
9	3	7.2	57	8.6	
10	4	6.6	52	n/a	
11	5				Not working
12	0	8.3	44	43.7	Acceptance limit
13	1	6.2	46	33.9	Used for analysis
14	2	3.3	79	37.3	
15	3	3.4	55	38.9	
16	4				Not working
17	5	5.1	45	n/a	Used for analysis
18	0	8.1	66	18.3	Acceptance limit
19	1	8.2	61	23.8	
20	2	4.6	65	27.0	
21	3	2.4	77	36.7	
22	4	12.4	75	n/a	
23	5	16.6	88	n/a	

factor (C^2S). Table 3.5 lists the OMPs that were used in the calculations; each of these potentials are global (cf. Chapter 2.6). The OMPs used in this study were chosen to match those used in Ref.[30], since it was desirable that the results be as comparable as possible for the later analysis. The only variations were the addition of the potential from Ref.[70] that introduced the adiabatic correction, as well as the necessary adjustment for a different reaction energy. One concern was that the global potential from Ref.[67] had originally been reported as appropriate for the mass range A=40–209, for which Neon is below. However, this potential had been used in the TUNL analysis [30] and successfully replicated known results for the spin-parities of energy levels in ^{21}Ne.

Table 3.5: The optical model potentials used in the ^{20}Ne(d,p)^{21}Ne analysis.

Index	Overlap	Potential	Reference
1	^{20}Ne + ^{2}H	An and Cai (2006)	[90]
		Wales and Johnson (1976)	[70]
2	^{21}Ne + ^{1}H	Varner *et al.* (1991)	[67]
3	^{20}Ne + n	Varner *et al.* (1991)	[67]
4	n + ^{1}H	A. M. Morro	[example]
5	^{20}Ne + ^{1}H	Varner *et al.* (1991)	[67]

The angular distributions extracted for each excited state in ^{21}Ne were compared to several ADWA predictions, each prediction was made assuming a different possible ℓ-transfer. Each excited state was assigned the spin-parity which produced the best agreement between the measured data and ℓ-transfer prediction. The comparisons between measured data points and theoretical predictions was made using chi-squared minimisation (cf. Chapter 3.2.6.3).

An important point to make is that because HELIOS measures all angular data points simultaneously, target density and the number of beam particles impinged is the same, therefore the shape of the differential cross section can be replicated without converting from measured counts to $d\sigma/d\Omega$ (mb/sr). As the spin-parity was determined independently of the absolute cross section, the J^π of the energy levels could be determined from the shape of the measured counts vs angle alone. The spectroscopic factor (C^2S), however, and by extension the neutron width (Γ_n), would require converting from arbitrary counts to mb/sr. Unfortunately, in the ^{20}Ne(d,p)^{21}Ne experiment the Elum, which is needed for reliable beam normalisation, was not in operation and therefore the HELIOS data alone could not be used to find the spectroscopic factor as defined in Eq.2.13.

3.2.6.2 Extrapolation

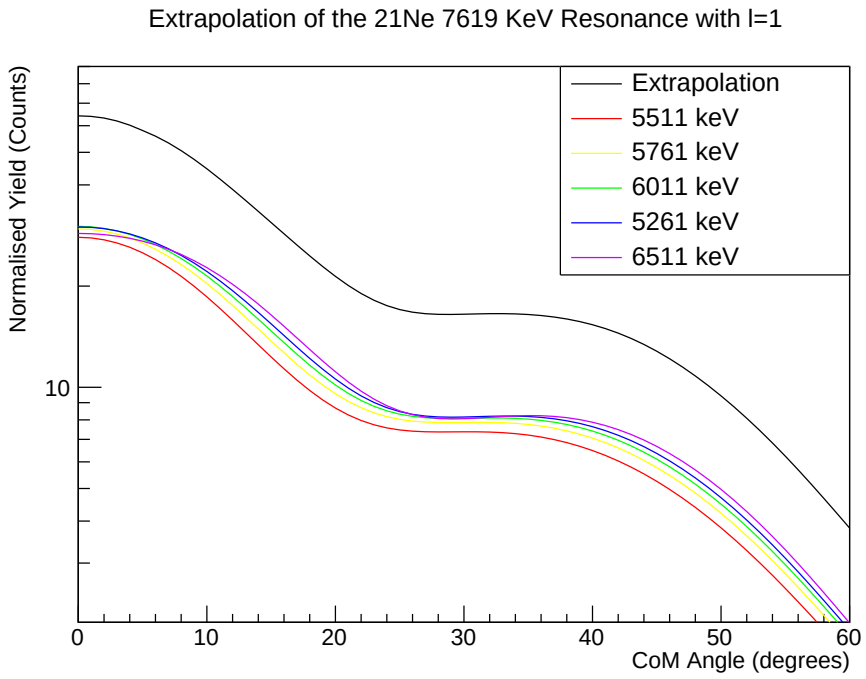

Figure 3.19: ADWA predictions for the differential cross section of the 7619 keV energy level in the ^{20}Ne(d,p)^{21}Ne reaction, calculated at a series of different binding energies below the neutron threshold. Each prediction is separated by a difference of 250 keV in binding energy. These calculations are indexed by the excitation energy used in FRESCO.

FRESCO can be used to produce DWBA predictions for bound states, however, once below zero binding energy for a state in the outgoing channel its predictions becomes unreliable. The neutron threshold for the ^{20}Ne(d,p)^{21}Ne reaction is 6761 keV and the excitation energy range of interest is 7.0–8.2 MeV. Therefore, a solution was needed to produce DWBA predictions above threshold; in this project the *extrapolation method* was used [91]. In this method, the assumption is made that the shape of the differential cross section varies smoothly with excitation energy and by determining this trend, the cross section can be computed at an energy just below threshold then scaled to the desired excitation energy using a linear extrapolation. Fig.3.19 shows the series of below threshold calculations for the angular distribution of the 7619 keV state in ^{21}Ne and the final prediction after extrapolation.

The extrapolation in this analysis is based on five FRESCO calculations at 250 keV intervals below the neutron threshold (listed on Fig.3.19). The average difference between these steps is then calculated and this average is used to extrapolate to 7619 keV from the 5511 keV prediction. This process is illustrated for one angle on Fig.3.20 as an example.

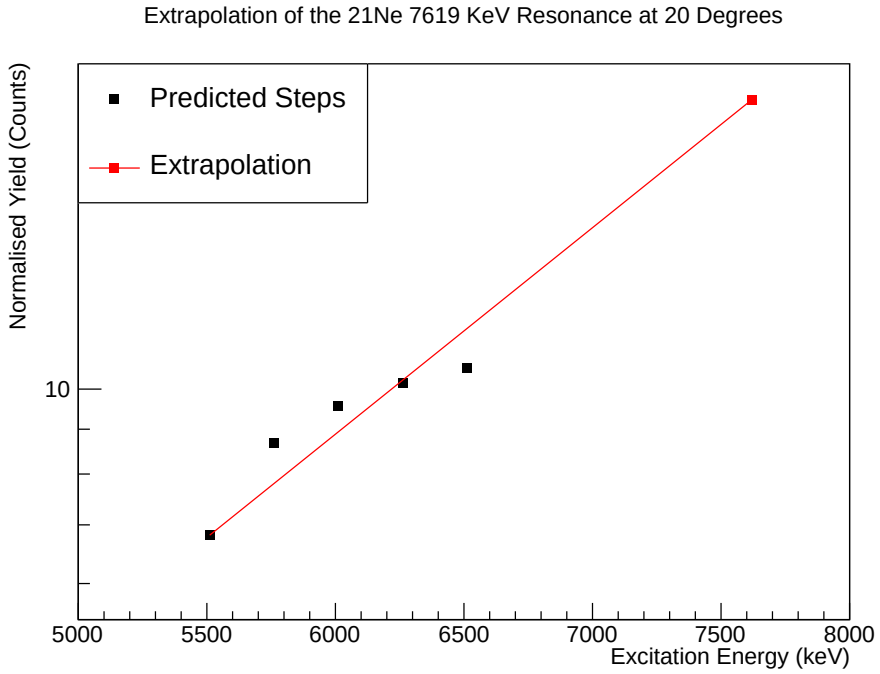

Figure 3.20: ADWA predictions for the differential cross section of the 7619 keV energy level in the ^{20}Ne(d,p)^{21}Ne reaction, calculated at an angle of 20°, for each of the binding energies listed on Fig.3.19. The final extrapolation to 7619 keV is also shown.

3.2.6.3 Chi-Squared Minimisation

After extrapolating the predictions to the required excitation energy the theoretical prediction of $d\sigma/d\Omega$ was compared to the data points measured in the experiment. This meant scaling the ADWA prediction to the measured data according to Eq.2.13. The scaling factor was found by using a chi-squared minimisation algorithm. The chi-squared test statistic compares the predicted differential cross section scaled by a factor S_f to the measured data, weighted by the uncertainty. The equation is

$$\chi^2 = \sum_i \frac{(x_i - \bar{x}_i)^2}{\sigma_i^2} \tag{3.12}$$

Where $\bar{x}_i$ is the expected value, x_i is the measured value and σ_i is the uncertainty on that measurement. The algorithm looped over Eq.3.12 and varied the scaling factor until the best fit between the theoretical predictions and the data was found. The best fit was defined as the smallest value of χ^2 that could be produced by the algorithm. From that minimum the best fitting value of S_f was determined.

3.2.6.4 FRESCO vs DWUCK

This analysis chose to use FRESCO to achieve consistency with other studies of the ^{21}Ne nucleus [30] and to combine it with the extrapolation method [91], enabling an investigation of those states above the neutron threshold. Extrapolating was a necessary with FRESCO as the program does not reproduce above-threshold states well. An alternative option would have been to use DWUCK [38], another commonly used program for modelling direct reactions. Unlike FRESCO, DWUCK incorporates the approach outlined in Ref.[92] which enables the code to converge the integrals of oscillatory wave functions for above-threshold states. Without that approach, the form factor integrals for transfers involving continuum states (above-threshold states) will not converge because the radial wave functions decay too slowly as the radius increases [64] - this is the reason FRESCO does not reproduce individual continuum states well. Using DWUCK therefore would have enabled the direct calculation of angular distributions for states above the neutron threshold, removing the extrapolation which is inherently an approximation. A full comparison between FRESCO and DWUCK with respect to measurements is beyond the scope of this project.

3.2.7 Partial Width Determination

As the HELIOS Elum was not in operation during the ^{20}Ne(d,p)^{21}Ne experiment there were no reliable measurements for beam intensity. Thus, absolute cross sections could not be determined and the partial widths could not be directly calculated since that required the spectroscopic factor, C^2S (cf. Eq.2.5). The data from HELIOS, however, could calculate a scaling factor (S_f) that was used to compare theoretical cross sections to proton counts. The conversion from counts to differential cross section requires first calculating the cross section as measured by each detector from the counts, beam intensity, target density and detector efficiency according to Eq.2.1. This value is then normalised to the solid angle of the detector.

Nevertheless, an attempt to provide estimates for the neutron widths was made. This was done using the TUNL data as a point of comparison and attempting to scale the HELIOS S_f to Γ_n. The procedure for doing this shall now be presented.

First the equation $\mathrm{C^2S_{TUNL}} = \kappa \times \mathrm{S_{f,\ HELIOS}}$ was defined where κ contains the experimental information missing from the HELIOS data. Next, κ was determined by comparing a state for which the HELIOS and TUNL spin-parity results were in good agreement, thus providing an estimate for κ; the 7620 keV energy level was used in this analysis. The HELIOS value of counts per steradian for the chosen state was then multiplied by $\mathrm{S_f}$ and κ to yield $\frac{d\sigma}{d\Omega}$. Then, using that $\frac{d\sigma}{d\Omega}$, the partial widths were calculated using Eq.2.162 in Ref.[62]. In this analysis, a

script written by Dr. P. Adsley was used to perform this step.

This method provided a means of estimating the neutron widths of these states, however, did contain a hidden uncertainty. The partial width of a state depends on the centre-of-mass energy of the reaction and the TUNL and HELIOS experiments were conducted at different centre-of-mass energies (13.984 MeV and 22.155 MeV respectively). Therefore the method described above, where the 7620 keV state is used to relate the TUNL data to the HELIOS data, is not comparing like-for-like. This systematic uncertainty could have been quantified had there been another state, besides 7620 keV, for which results from HELIOS and TUNL to be compared. Unfortunately, at the time of study there was no available results on other states for which HELIOS and TUNL showed agreement. Investigations of some of the lower energy states observed in the TUNL experiment are ongoing [89] and could be used in future to quantify the uncertainty due to the energy difference.

3.3 Results and Discussion

Table 3.6: Results from the ^{20}Ne(d,p)^{21}Ne experiment at HELIOS. Literature ℓ values come from NNDC [31] below the 6.0 MeV and from Ref.[30] and Ref.[89] above that energy. Values for $(2J+1)S_f$ are normalised to 6609 keV with $2J^\pi = 5^+$ and the literature comparison comes from Ref.[93].

E_x [keV]	$2J^\pi$	ℓ_n	ℓ_n *lit.*	$(2J+1)S_f$	$(2J+1)S_f$ *lit.*	Γ_n [eV]
2794	1^+	0	0	0.378 ± 0.531		
4526	$(3, 5)^+$	2	2	1.024 ± 0.240, 1.146 ± 0.260	1.56	
4725	$(5, 3)^+$	2	1	3.890 ± 0.779, 3.476 ± 0.703	3.19	
5334	$(5, 3)^+$	2	2 or 3	2.909 ± 0.621, 2.591 ± 0.567	0.84	
5549	$(5, 3)^+$	2	2	1.280 ± 0.716, 1.143 ± 0.183	0.74	
5822	$(7, 5)^-$ $(5, 3)^+$	3 2	2	0.792 ± 0.167, 0.703 ± 0.149 0.616 ± 0.113, 0.548 ± 0.102	0.34	
6609	$(5, 3)^+$	2	2	1.000 ± 0.160, 0.884 ± 0.147	1.00	
7106	$(5, 3)^+$	2	2	0.110 ± 0.033, 0.099 ± 0.029		
7176	$(5, 3)^+$	2	1	0.297 ± 0.046, 0.265 ± 0.042		
7337	$(7, 5)^-$	3	1	0.231 ± 0.052, 0.205 ± 0.047		
7420		undetermined	1			
7559	$(1, 3)^-$	1	2	0.036 ± 0.006, 0.042 ± 0.008		
7619	$(1, 3)^-$	1	1	0.043 ± 0.007, 0.051 ± 0.009		
7749		undetermined				< 7200
7820	3^-	1	2	0.034 ± 0.009		7600 ± 2100
7980	$(11, 13)^+$ $(11, 9)^-$	6 5	1	1.473 ± 0.204, 1.547 ± 0.221 0.295 ± 0.053, 0.263 ± 0.048		

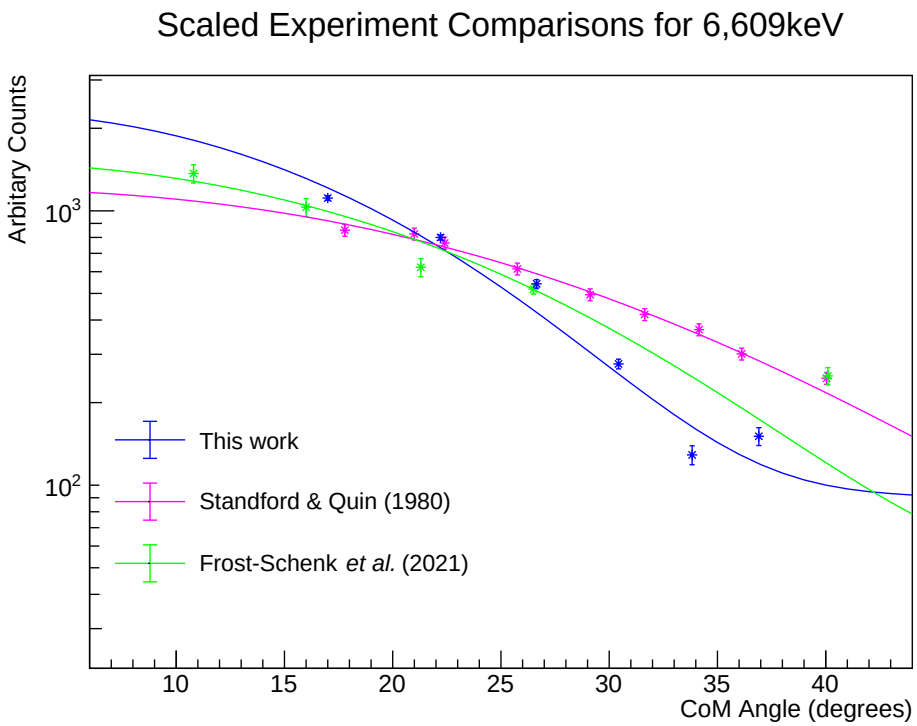

Figure 3.21: A comparison of three independent experiments studying the ^{20}Ne(d,p)^{21}Ne reaction, with DWBA fits for each. Data included from Ref.[30] (green: $\chi^2 = 5560$), Ref.[93] (hot magenta: $\chi^2 = 53215$) and this work (blue: $\chi^2 = 97$). Rescaled arbitrarily for comparison. DWBA preformed using the models in Table 3.5 (minus the Adiabatic correction) at the centre-of-mass energy of each experiment.

Some general observations shall be discussed here before the DWBA results are presented. A consistent problem with this analysis was the low resolution. The recoil gates shown in Fig.3.14 are quite restrictive and could have been expanded since the background is well controlled, which may have improved the number of counts under the peaks, however, the main source of uncertainty was the low resolution rather than counting statistics, therefore expanding the gates would likely not have significantly improved the uncertainty. Furthermore, the absolute cross section could not be measured without the Elum and therefore neutron widths for the various excited states could not be directly calculated. A method to indirectly calculate neutron widths by combining both these data and the results in Ref.[30] was used (cf. Chapter 3.2.7). An improved version of this experiment would use include the Elum so that cross sections could be determined and neutron widths directly calculated, also using an array of detectors with a consistently good resolution (ie. detector 8) would have reduced uncertainty when fitting individual resonances in the Gamow window.

Since this experiment and the TUNL [30] experiment were conducted at slightly different centre-of-mass energies, it provides an opportunity to compare the effects of these different

kinematics on the measured data and the associated DWBA predictions. Fig.3.21 shows the results for 6609 keV, which is known to be either a $\frac{3}{2}^+$ or $\frac{5}{2}^+$ state. Results from a third (d,p) experiment [93] have also been included and all three data sets have been arbitrarily scaled for an easy comparison of their shapes. The HELIOS experiment was conducted at a centre-of-mass energy of 22.155 MeV, the experiment of Ref.[30] at 13.984 MeV and the experiment of Ref.[93] at 9.091 MeV. Note the higher the centre-of-mass energy, the more forward peaked the angular distribution becomes. For the purpose of this comparison the HELIOS data has been fitted to DWBA predictions rather than ADWA.

3.3.1 ADWA versus DWBA

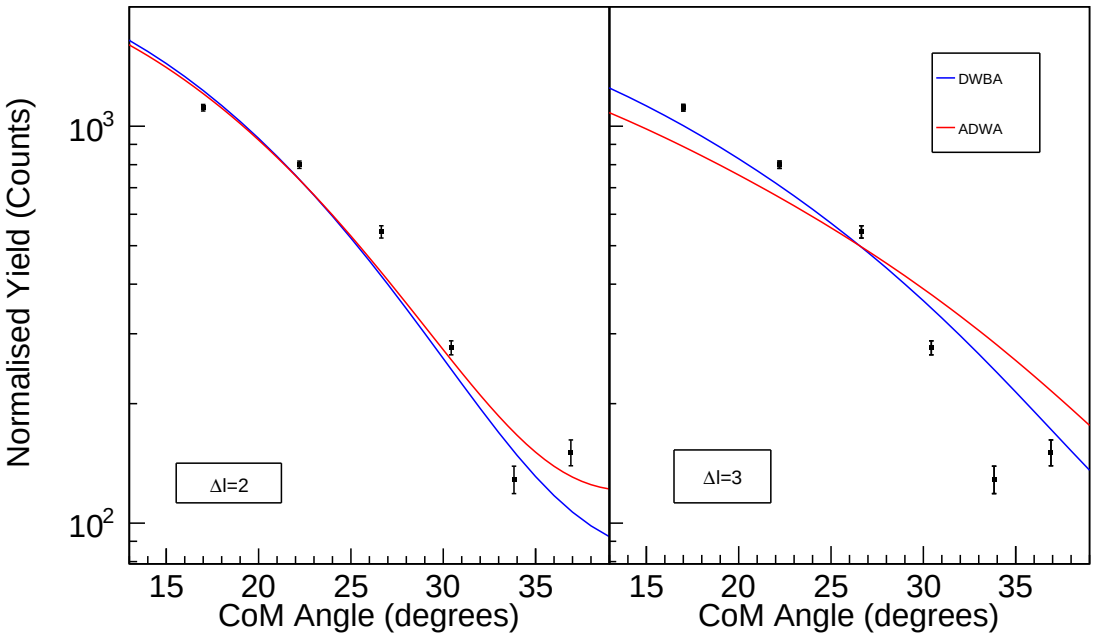

Figure 3.22: A comparison of two different ℓ-transfers predicted for the 6609 keV energy level (left is $\ell = 2$, right is $\ell = 3$) to illustrate the improved fit of ADWA model predictions (red) over DWBA model predictions (blue).

Fig.3.22 illustrates the improvement of ADWA over DWBA in modelling the data of this experiment. There is only a small difference between the two models (blue=DWBA, red=ADWA), which is to be expected as the ^{21}Ne beam energy of 11 MeV/u is close to the threshold for the ADWA regime (10 MeV/u) and using DWBA would still be reasonable. The two plots show the predictions compared to the data from the 6609 keV state for $\ell = 2$ (left) and $\ell = 3$ (right). The 6609 keV state is known to be $\ell = 2$ which is why it was chosen to compare the ADWA and DWBA predictions. As can be seen, both ADWA and DWBA yield a good fit with the data.

Turning to the $\ell = 3$ predictions, however, it can be seen that the DWBA predictions give a worse fit to the data than ADWA. Indeed, the DWBA analysis cannot fully reject $\ell = 3$. In contrast, the ADWA predictions can exclude the $\ell = 3$ predictions. Therefore, because ADWA reproduces literature results more reliably than DWBA for these data, ADWA was used in this analysis.

3.3.2 States Below the Neutron Threshold

All ℓ transfers for (d,p) have two possible J^π values (except $\ell = 0$, which has only one). These data cannot be used to discriminate between the possible J^π values for a given ℓ-transfer since the differences between the predictions are too small. Therefore, the following plots show the fits to the measured data for only the J^π with the smallest χ^2 for each ℓ-transfer.

2794 keV

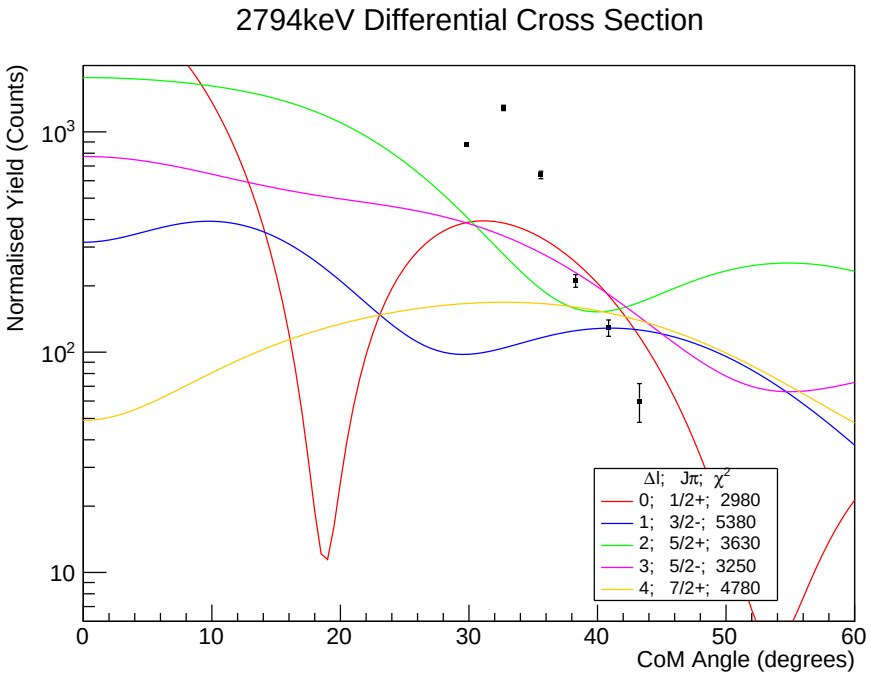

Figure 3.23: Measured differential cross section for the 2794 keV energy level compared to different ℓ-transfer predictions and the χ^2 value of each fit. The best fitting prediction is $\ell = 0$

This state was reported as prominent by Ref.[94] who assigned it a J^π of $1/2^+$ in their ^{20}Ne(d,p)^{21}Ne study. This analysis is in agreement with that study, as can be seen in Fig.3.23. While $\ell = 0$ did give the lowest χ^2 fit for these data, the measured shape was still somewhat different to the predicted shape for $\ell = 0$. A possible reason for this is that there is an unresolved peak at 2867 keV in the spectrum [31] that has erroneously been included in the fits for 2794 keV.

The 2867 keV peak has not previously been observed in (d,p) experiments, which seldom analyse states so low in excitation energy, and was therefore not included in the fitting here. Given the somewhat different shape of these data with respect to the predictions and taking into account the otherwise good agreement of the other results for both ADWA predictions and literature values, it is possible that this overlap is the source of the discrepancy. The 2867 keV state has a reported spin-parity of $9/2^+$ [31]. Further analysis, comparing measurements to combined predictions for these two overlapping states, might be able to determine if this overlap was the source of the poor agreement between data and predictions. Another reason may be that, since the measurements for this peak are relatively far from 0^o, the ADWA predictions are failing to reproduce the data. Such deviations between ^{20}Ne(d,p)^{21}Ne measurements and DWBA analysis have previously been observed at large angles above 40° [93, 30].

4526 keV

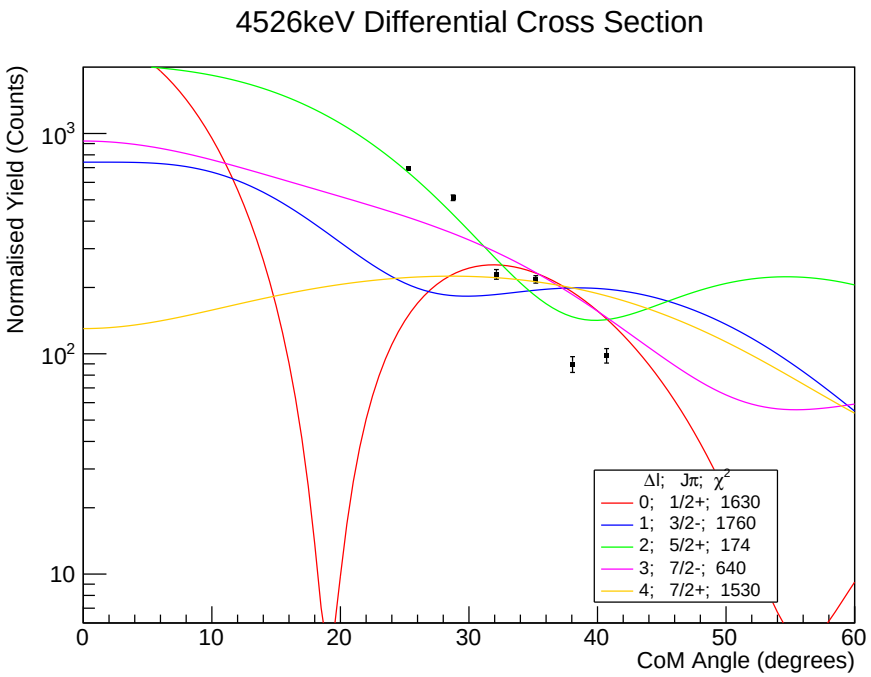

Figure 3.24: Measured differential cross section for the 4526 keV energy level compared to different ℓ-transfer predictions and the χ^2 value of each fit. The best fitting prediction is $\ell = 2$.

Previous ^{20}Ne(d,p)^{21}Ne studies have determined a spin-parity of either $5/2^+$ or $3/2^+$ [93, 94] and studies of ^{21}Ne states populated by other experiments such as the ^{16}O(^{7}Li,npγ)^{21}Ne of Ref.[95] confirmed $5/2^+$. This study is in agreement with the literature, finding that the smallest χ^2 fit is given by $\ell = 2$, meaning a J^π assignment of either $5/2^+$ or $3/2^+$. The predicted transfers are shown in Fig.3.24 where it can be seen by eye that $\ell = 2$ is the best fit.

4725 keV

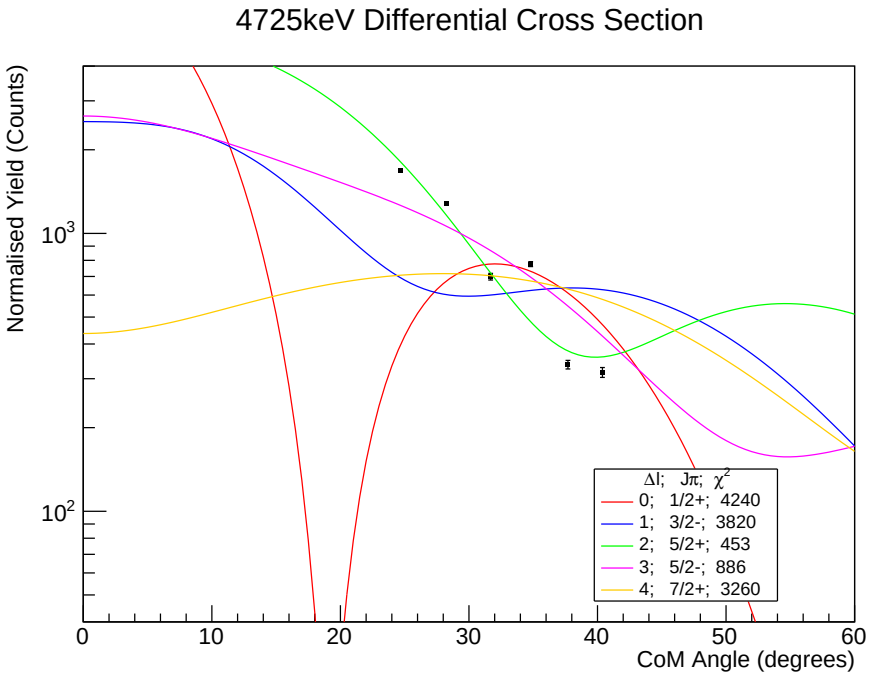

Figure 3.25: Measured differential cross section for the 4725 keV energy level compared to different ℓ-transfer predictions and the χ^2 value of each fit. The best fitting prediction is $\ell = 2$.

This state is an unresolved doublet with the 4685 keV state, which may be the source of the disagreement between this study, which from Fig.3.25 finds a best fit of $\ell = 2$, and the literature value of $\ell = 1$. The literature value was determined in another ^{20}Ne(d,p)^{21}Ne study [93]. This disagreement is unusual as the results for energy levels below the neutron threshold in this study are generally in agreement with previous experiments, including Ref.[93].

5334 keV

The spin-parity of $7/2^-$ adopted by Ref.[31] for this state would imply $\ell = 3$ in a ^{20}Ne(d,p)^{21}Ne reaction and comes from a ^{17}O(^{7}Li,npγ)^{21}Ne study [96]. Fig.3.26 shows that these data do not agree with that assignment. This study instead finds agreement with the previous ^{20}Ne(d,p)^{21}Ne experiment of Ref.[94] and the previous ^{18}O(α,nγ)^{21}Ne study of Ref.[97] that both found best fitting spin-parities of J^π of either $5/2^+$ or $3/2^+$. Ref.[96] reported using gamma-ray coincidence measurements to determine transitions and it is possible therefore that this energy level was wrongly associated with one of the observed cascades.

5549 keV

This study found that a spin-parity of either $5/2^+$ or $3/2^+$ yielded the lowest χ^2 value for these data points (another $\ell = 2$) as can be seen on Fig.3.27 and this is again in agreement with

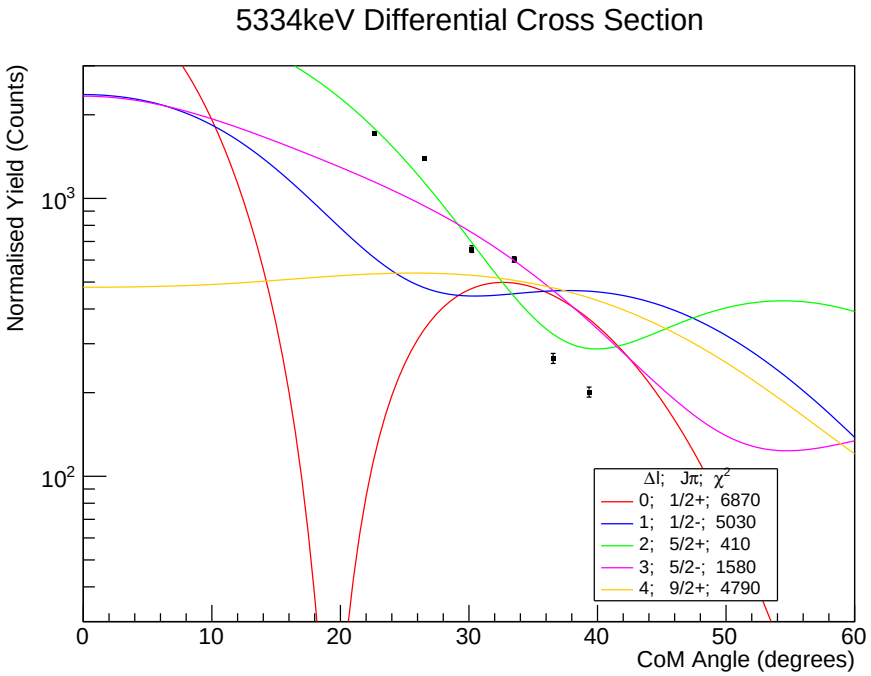

Figure 3.26: Measured differential cross section for the 5334 keV energy level compared to different ℓ predictions and the χ^2 value of each fit. The best fitting prediction is $\ell = 2$.

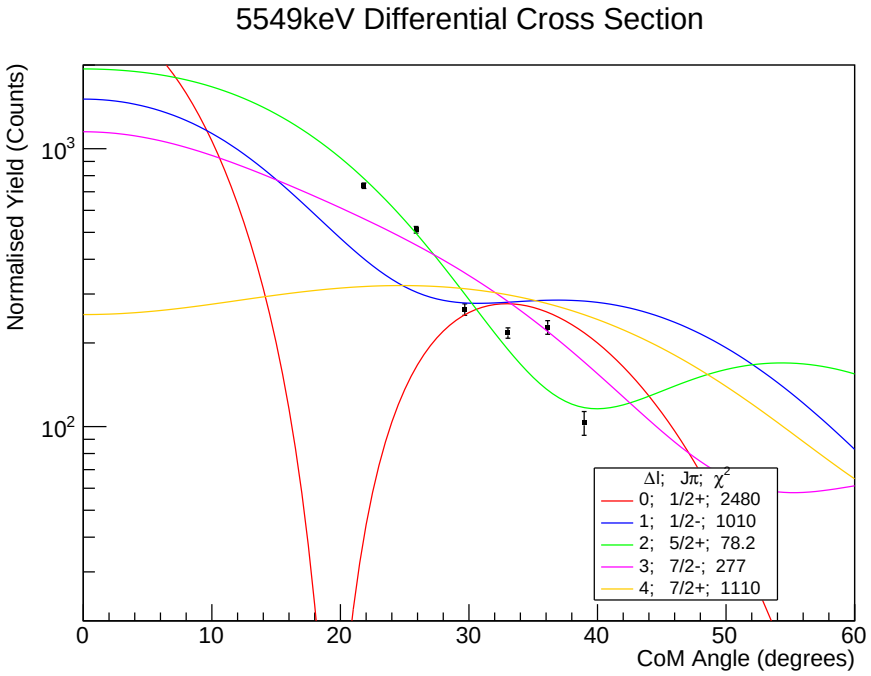

Figure 3.27: Measured differential cross section for the 5549 keV energy level compared to different ℓ-transfer predictions and the χ^2 value of each fit. The best fitting prediction is $\ell = 2$.

the previous ^{20}Ne(d,p)^{21}Ne study of Ref.[94] and the neutron pickup experiment of Ref.[98] that determined a spin-parity of $3/2^+$.

5822 keV

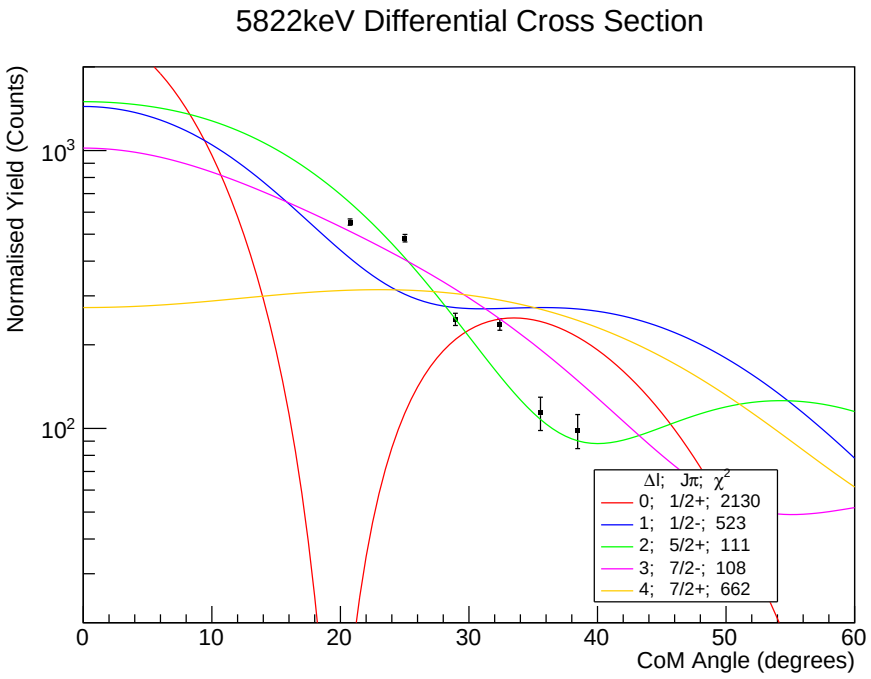

Figure 3.28: Measured differential cross section for the 5822 keV energy level compared to different ℓ-transfer predictions and the χ^2 value of each fit. The best fitting predictions are $\ell = 2$ and $\ell = 3$.

An $\ell = 2$ transfer produced the smallest χ^2 fit for this state, but Fig.3.28 shows that $\ell = 3$ is also a possibility, having a very similar χ^2 value and fitting well by eye. The literature J^π is $3/2^+$, based on a previous ^{20}Ne(d,p)^{21}Ne experiment [94] and a ^{18}O(α,nγ)^{21}Ne experiment [99], implying a transfer of $\ell = 2$. In these data, the 5822 keV energy level is unresolved with the 5818 keV state. 5818 keV has a spin-parity in literature of $7/2^-$ corresponding here to an $\ell = 3$ transfer. It is possible that the 5818 keV state is contributing to the peak labelled 5822 keV and is the source of the ADWA analysis uncertainty.

6609 keV

As seen in Fig.3.29 the smallest χ^2 fit for this state was $\ell = 2$, agreeing with the results of Ref.[30]. This state is very prominent in the ^{20}Ne(d,p)^{21}Ne spectrum and is close to the neutron threshold for ^{21}Ne at 6761 keV. Previous studies have taken advantage of the relative isolation of this energy level by using it to normalise the spectroscopic factors of all other levels [93]. By normalising the scaling factors from this analysis to that of 6609 keV comparisons can be made to literature values for C^2S of different states, even without the absolute cross section.

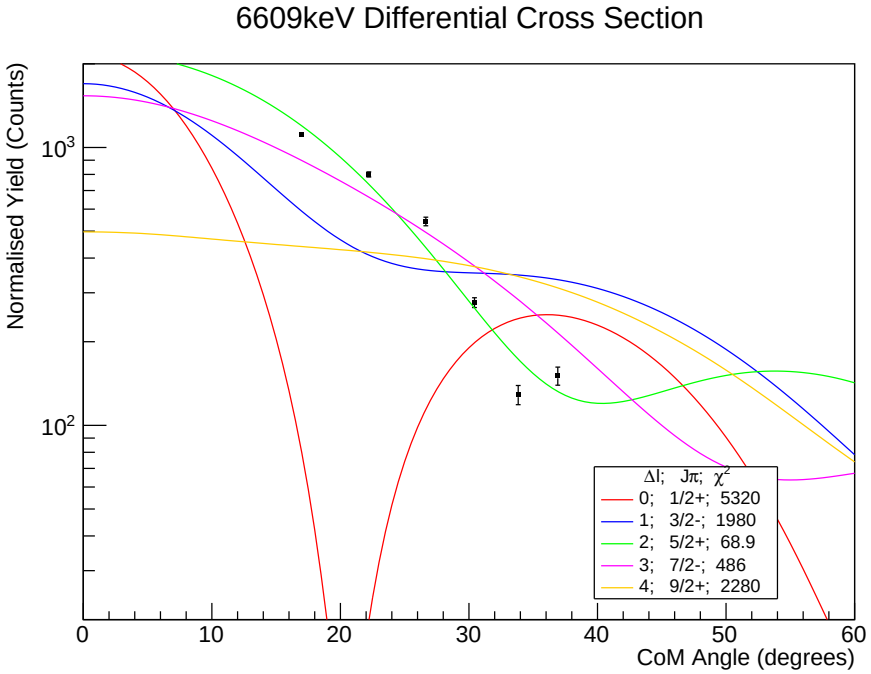

Figure 3.29: Measured differential cross section for the 6609 keV energy level compared to different ℓ-transfer predictions and the χ^2 value of each fit. The best fitting prediction is $\ell = 2$

3.3.3 States Above the Neutron Threshold

7106 keV

In this study the fit with the lowest χ^2 was $\ell = 2$, agreeing with the previous assignment from Ref.[30]. From visual inspection of 3.30 it can be seen that $\ell = 1$ and $\ell = 3$ also give reasonable fits to the data. This energy level is not fully resolved from the 7176 keV state in these spectra and it is possible that some 7176 keV counts have been included in the 7106 keV peak.

7176 keV

This state is not recorded in the compilations [31, 100, 101]. However, it was quite prominent in both this experiment and the TUNL experiment [30]. The TUNL study assigned a momentum transfer of $\ell = 1$ [89] for which this study is in disagreement. The best fitting ℓ-transfer in this study was $\ell = 2$, as seen in Fig.3.31 the predictions for $\ell = 1$ gave a relatively poor χ^2 minimisation. This state is unresolved with the 7106 keV state in the HELIOS spectra, meaning that the fits are less reliable than for other, better isolated energy levels. Another possible reason for the disagreement between these states is that there are several small ^{21}Ne peaks observed in the TUNL experiment that were not included in the fitting for the HELIOS data, such as the 7156(1) keV state. The reasons for treating these other states as negligible

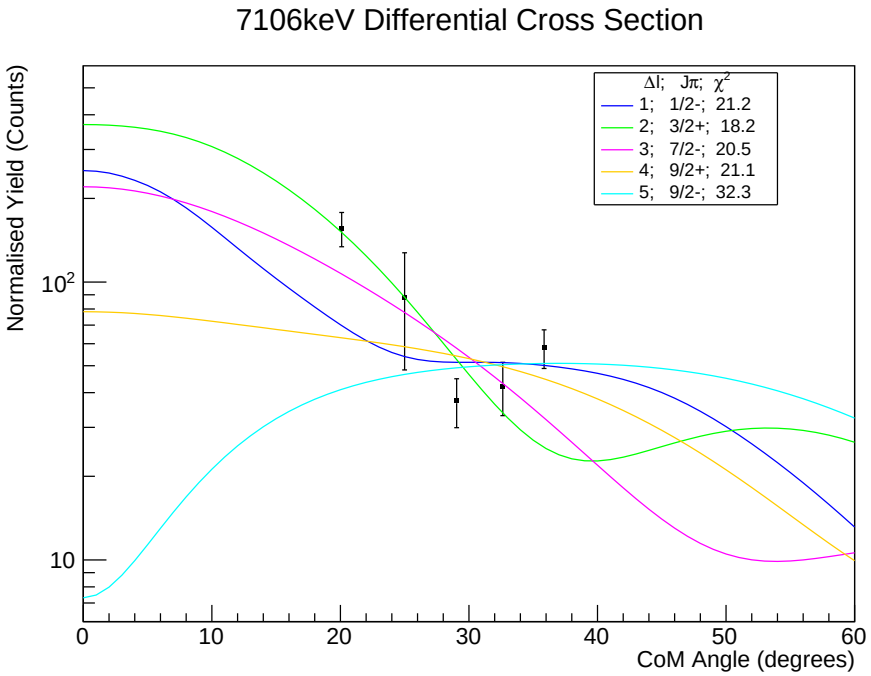

Figure 3.30: Measured differential cross section for the 7106 keV energy level compared to the five best fitting ℓ-transfer predictions and the χ^2 value of each fit. The best fitting prediction is $\ell = 2$.

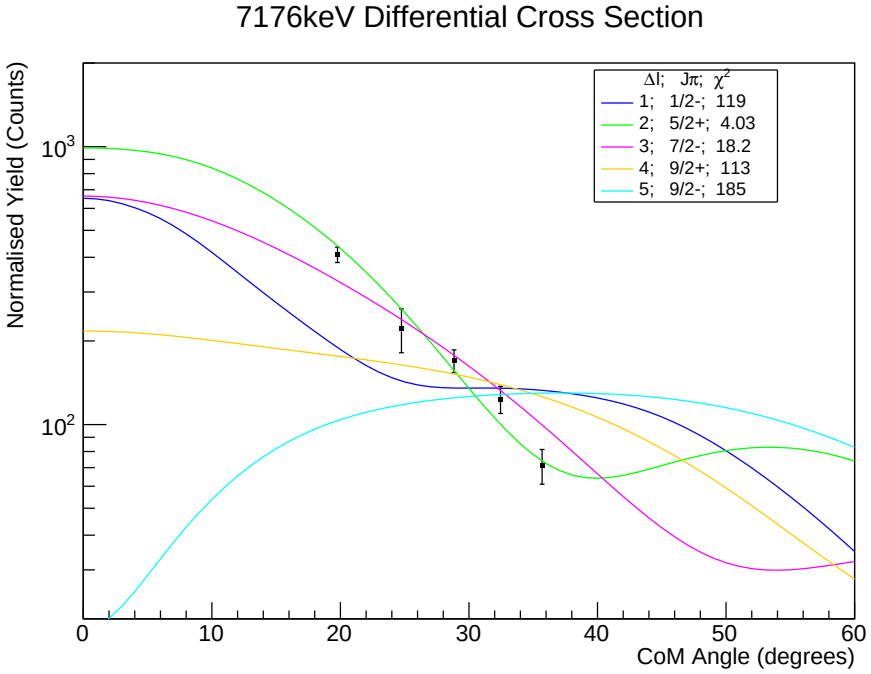

Figure 3.31: Measured differential cross section for the 7176 keV energy level compared to the five best fitting ℓ-transfer predictions and the χ^2 value of each fit. The best fitting prediction is $\ell = 2$.

was to avoid over fitting the data, as has already been discussed. However, the disagreement with previous measurements could be explained if those states are more strongly populated in this study than they were in the TUNL experiment. It is possible that some resonances are stronger in this study than in the TUNL experiment since this study was conducted at the higher centre-of-mass energy of 22.155 MeV compared to 13.984 MeV used at TUNL [30].

7337 keV

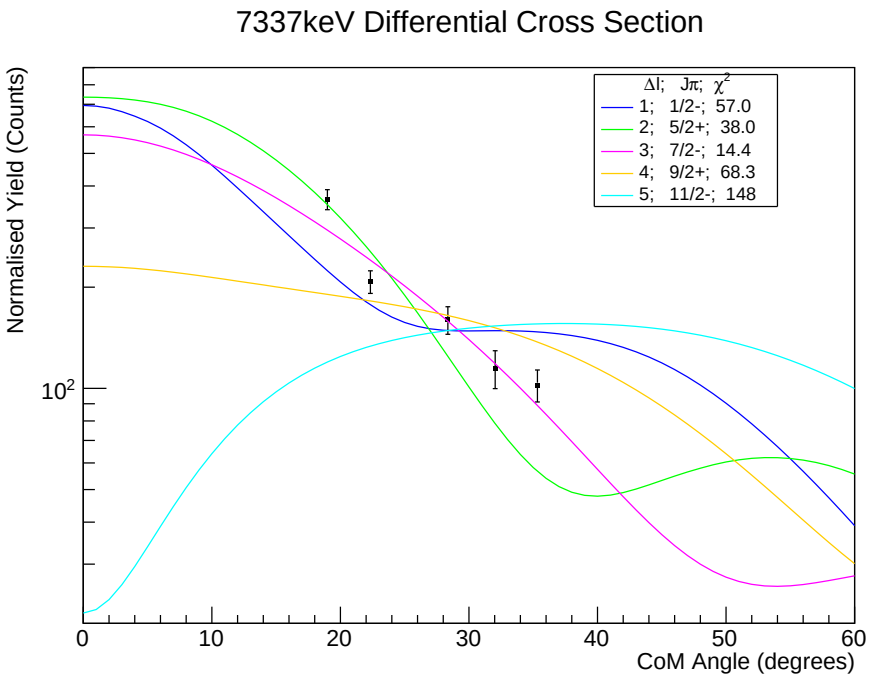

Figure 3.32: Measured differential cross section for the 7337 keV energy level compared to the five best fitting ℓ-transfer predictions and the χ^2 value of each fit. The best fitting prediction is $\ell = 3$.

This is another unresolved energy level in the HELIOS spectrum. The results, seen in Fig.3.32, give good agreement with several possible ℓ-transfers, in particular $\ell = 1, 2 \,\&\, 3$. The best fitting ℓ-transfer was $\ell = 3$, disagreeing with the much higher resolution analysis of the TUNL experiment [89] which found that $\ell = 2$ best fit their data (the data came from the same experiment as Ref.[30] but investigated lower energy levels). The peak fits for this state overlap with several other states, however, as previously discussed, only the levels prominent in the TUNL data were included in the fitting procedure for the HELIOS data. Therefore, the 7337 keV and 7420 keV states were fitted in this region, ignoring other known energy levels such as 7470 keV on the basis that they are negligible compared to the other peaks observed in the TUNL data. No state had been reported at this energy until the TUNL study. However, the compilations do include a state at 7320±5 keV [31, 100, 101] which may have been the same

level. It appeared prominently in the TUNL study and was therefore included in the fitting here.

7420 keV

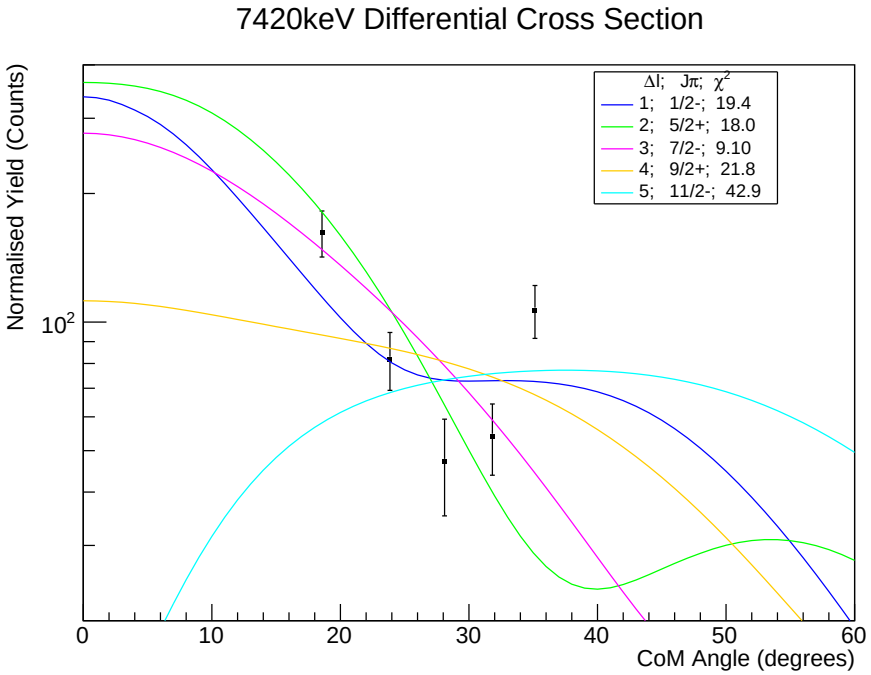

Figure 3.33: Measured differential cross section for the 7420 keV energy level compared to the five best fitting ℓ-transfer predictions and the χ^2 value of each fit. None of the predictions fit these data well.

This state overlaps with the 7337 keV state in the HELIOS data and could not be resolved. Unfortunately, the best fitting spin-parity could not be identified as the data fit three different predictions for ℓ (1,2 and 3), as shown in Fig.3.33 along with the χ^2 values for the minimisation of the predicted transfers to the measured data. The inability to separate this state from the 7337 keV peak satisfactorily is the likely reason for the strange shape of the data.

7559 keV

This state was observed in the TUNL data and reported $\ell = 2$ despite also fitting the $\ell = 1$ predictions [30]. The basis for this was that an $\ell = 1$ transfer would mean a neutron width large enough to be seen in the neutron resonance experiment of Ref.[102], since such a strong neutron resonance was not observed it was assigned a spin-parity of either $\frac{3}{2}+$ or $\frac{5}{2}+$. As seen on Fig.3.34, in this study $\ell = 2$ is not a good fit for these data and therefore must be reported as $\ell = 1$, despite not agreeing with the results of Ref.[102]. A more detailed discussion on the disagreements between this study and Ref.[102] can be found in the 7820 keV section of this chapter.

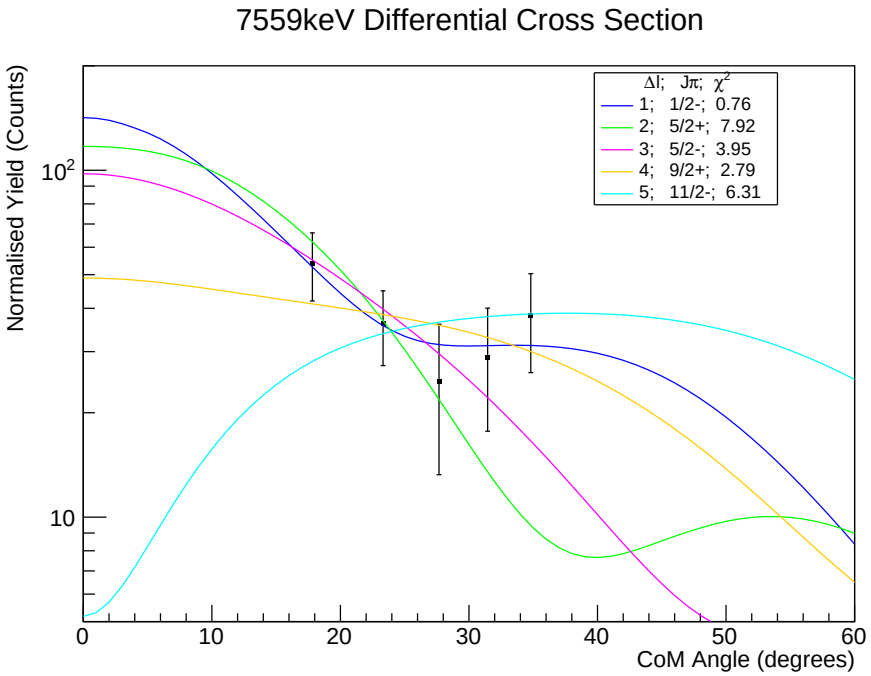

Figure 3.34: Measured differential cross section for the 7559 keV energy level compared to the five best fitting ℓ-transfer predictions and the χ^2 value of each fit. The best fitting prediction is $\ell = 1$.

7619 keV

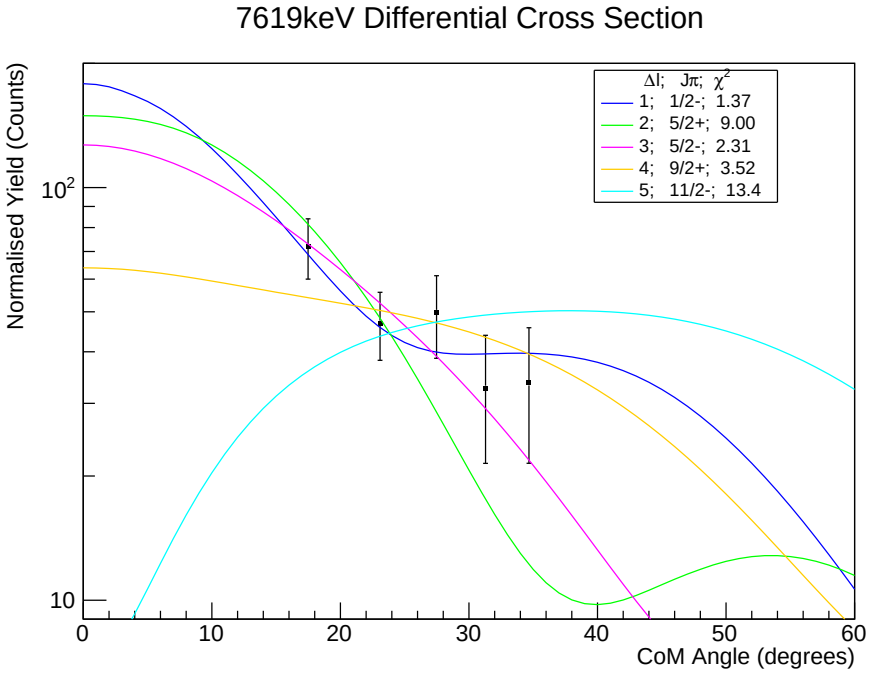

Figure 3.35: Measured differential cross section for the 7619 keV energy level compared to the five best fitting ℓ-transfer predictions and the χ^2 value of each fit. The best fitting prediction is $\ell = 1$.

This study is in good agreement with the $\ell = 1$ assignment of Ref.[30] as seen on Fig.3.35. Because this state was the only one above the neutron threshold for which the was a clear agreement between this study and Ref.[30], this energy level was chosen for use in estimating the partial widths of the 7820 keV and 7749 keV states observed in this experiment. The partial width adopted by Ref.[30] was 8000(1000) eV; for a detailed explanation of how these data were used to estimate the Γ_n for other states in this experiment without a measured C^2S see Chapter 3.2.7.

7749 keV

Determining the spin-parity of this state was one of the aims of this experiment. It is worth noting at the outset that the excitation energies in the compilations [31, 101] do not agree, the reason being that Ref.[31] has not been updated with the energy correction to Ref.[103] made by Ref.[101]. This correction to Ref.[103] was made to fix a systematic error in the results of that study and increased the measured energies of the excited states in ^{21}Ne. The energy used in fitting these data came from Ref.[30] and had a value of 7748.8(17) keV.

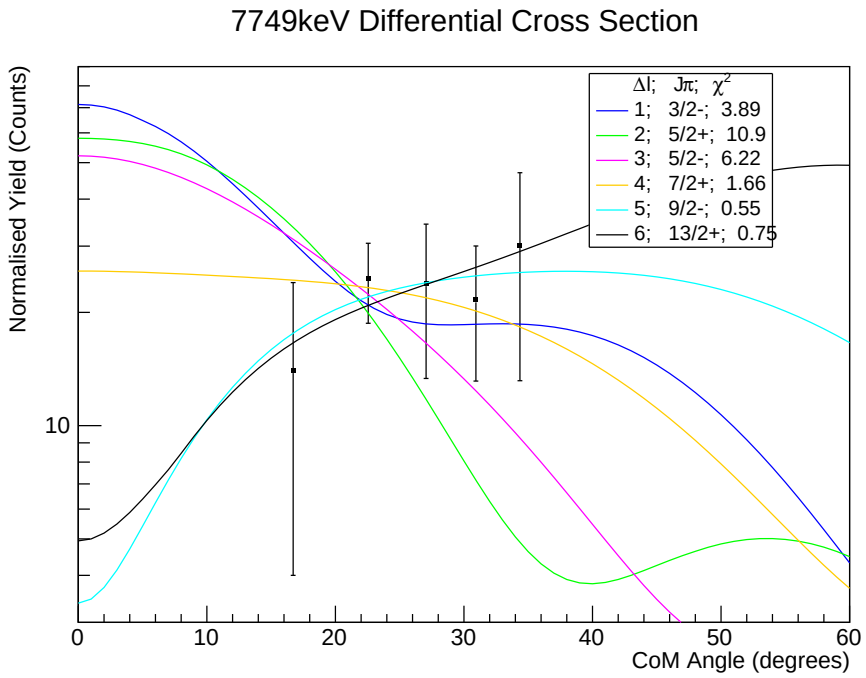

Figure 3.36: Measured differential cross section for the 7749 keV energy level compared to all ℓ-transfer predictions trialled (except $\ell = 0$) and the χ^2 value of each fit. The large uncertainties on the measurements mean that many predictions fit these data.

Unfortunately, due to the combination of low statistics and low resolution this study has been unable to determine the ℓ-transfer from the measured differential cross section, which is consistent with being flat, as shown on Fig.3.36. It is worth recalling here that these resonances

are assumed to arise from direct reactions. Given the flat shape of the differential cross section at this energy, it could mean that other reaction mechanisms are contributing, such as multi-step reactions. In which case, ADWA analysis would not be a good representation of the ongoing physics.

The only ℓ-transfer that could be excluded from these data was $\ell = 2$. As this state is above the neutron threshold $\ell = 0$ transfers are unlikely, since without either a Coulomb barrier or an angular momentum barrier there is nothing to hold the transferred neutron in the nucleus. $\ell = 0$ would therefore mean the peak should be broad, as is the case for the 7211 keV state [104] and while it is difficult to tell from these data, past observations of this state have found it to be narrow [30]. Therefore, the minimum possible transfer is assumed to be $\ell = 1$. Based on an assumption of $\ell = 1$, and using the method detailed in Chapter 3.2.7, the neutron widths were calculated to be 4800±2400 eV and 2400±1000 eV for $J^\pi = \frac{1}{2}^-$ and $\frac{3}{2}^-$ respectively.

A state with a neutron width greater than 1000 eV should have been observed in neutron resonances studies such as Ref.[102]. Because no such state was observed in that experiment, it suggests the width is much smaller making a transfer of $\ell = 1$ unlikely. In that case, since Fig.3.36 can exclude $\ell = 2$ the minimum transfer for this state would be $\ell = 3$. This study disagrees with Ref.[102] over other results (see the results for 7820 keV) and so it was decided that an upper limit for the neutron partial width would be reported assuming $\ell = 1$. That limit was 7200 eV. For completeness neutron widths were calculated assuming several different spin-parity combinations (including $\ell = 2$) and are shown in Table 3.7.

Table 3.7: Neutron widths and spin factors for 7749 keV calculated using the method described in Chapter 3.2.7 for several different possible spin-parities and limits for the $^{17}O(\alpha,n)^{20}Ne$ resonance strengths calculated using the alpha width from Ref.[37].

ℓ	$2J^\pi$	Γ_n (eV)	ω	$< \omega\gamma_n$ (μeV)
1	1-, 3-	4800±2400, 2400±1000	$\frac{1}{3}$, $\frac{2}{3}$	7.2×10^{-3}
2	3+, 5+	120±100, 80±64	$\frac{2}{3}$, 1	14.4×10^{-3}
3	5-, 7-	4.6±2.8, 3.2±2.5	1, $\frac{4}{3}$	21.6×10^{-3}

Since the rate of a nuclear reaction through a narrow resonance is linearly dependent on the resonance strength ($\omega\gamma$). Table 3.7 includes a column for the spin-factor ($\omega = \frac{(2J_r+1)}{(2J_1+1)(2J_2+1)}$ cf. Chapter 2.4) calculated for the $^{17}O(\alpha,n)^{20}Ne$ reaction using different spin-parities. $2J^\pi = 5+$ for ^{17}O and $2J^\pi = 0+$ for ^4He, therefore the spin factor reduces to $\omega = \frac{(2J_r+1)}{6}$ for an $^{17}O+\alpha$ reaction. The alpha width is assumed to be $\Gamma_\alpha << \Gamma_{n,\gamma}$ meaning $\omega\gamma_n = \omega\Gamma_\alpha$, therefore the resonance strength can be calculated using these new results and alpha widths calculated from

Table 2 in Ref.[37]. Γ_α is assumed to be 0.022 μeV for 7749 keV and with the limit of $\ell = 1$ the resonance strength is $\omega\gamma_n < 7.2 \times 10^{-3}\mu$eV. Table 2 of Ref.[37] reported a strength of 0.022 μeV meaning that this result is a factor of three lower than the literature value; this would imply a reduced rate of ^{17}O(α,n)^{20}Ne reaction compared what has previously been used in models [30] and would result in reduced s-process nucleosynthesis due to fewer neutrons being recycled after the ^{16}O(n,γ)^{17}O reaction.

7820 keV

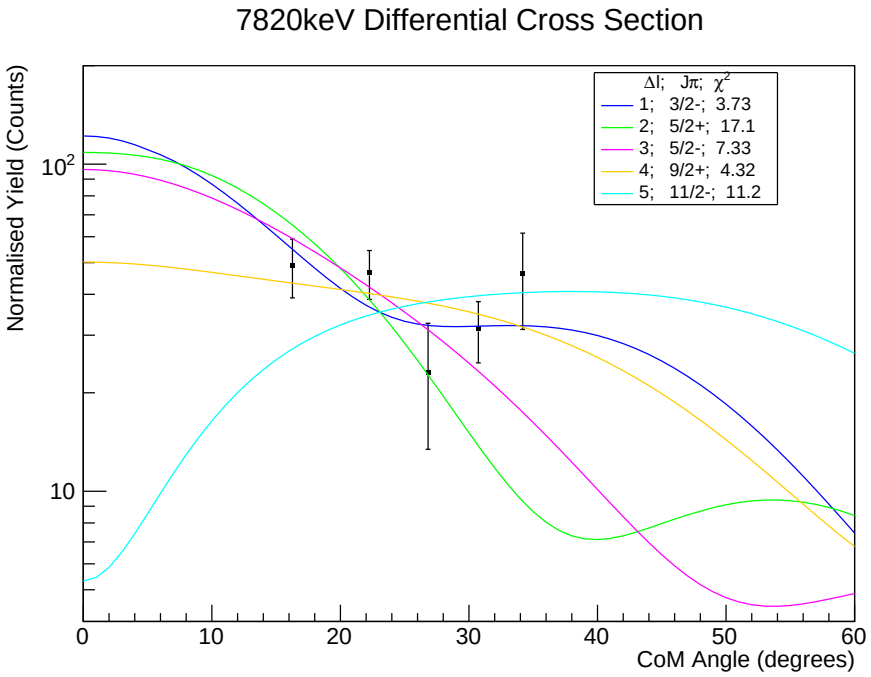

Figure 3.37: Measured differential cross section for the 7820 keV energy level compared to the five best fitting ℓ-transfer predictions and the χ^2 value of each fit. The best fitting prediction is $\ell = 1$.

This state is also of significant interest for nuclear astrophysics, sitting in the energy range of interest for alpha reactions on ^{17}O in rotating massive stars. The best fitting ℓ-transfer for this state was $\ell = 1$, which is shown in Fig.3.37. Ref.[30] reported an ℓ-transfer of $\ell = 2$ despite their data better fitting the $\ell = 1$ prediction because the resulting value for $\Gamma_n(\ell = 1)$ should have been large enough to be observed in the earlier neutron resonance experiment by Ref.[102]. This new ^{20}Ne(d,p)^{21}Ne measurement by HELIOS shows that $\ell = 2$ fits poorly to the data for 7820 keV. The best fitting spin-parities are $J^\pi = 1/2^-$ or $3/2^-$ for the 7820 keV state and the corresponding neutron widths are 15400 ± 4500 or 7600 ± 2100 eV respectively. A partial width of 7600 ± 2100 eV is consistent with the experimental width observed on the TUNL spectra [30]. However, the higher Γ_n can be ruled out, therefore the assignment of $J^\pi = 3/2^-$ was made. A

spin-parity assignment of $3/2^-$ begs the question as to why, if for this level $\Gamma_n = 7600 \pm 2100$ eV, did Ref.[102] not observe this state, since that study did report other resonances of a similar width? On Fig.4 of Ref.[102], there is a weak feature at approximately 7860 keV which was not investigated. No energy level has been reported in ^{21}Ne at that energy but the nearest known state is 7820 keV. If this feature does arise from the 7820 keV energy level then that could resolve the disagreement between ^{20}Ne(d,p)^{21}Ne studies and neutron resonance experiments. Ref.[102] was in good agreement with Ref.[30] for the energies of the excited states, but since that region was not studied closely the granularity of the energy measurements is large compared to other parts of the spectrum; this makes it possible that a peak could have been missed. For these reasons, a future neutron resonance study investigating ^{21}Ne resonances in this energy region is recommended.

The spin-factor in the ^{17}O(α,n)^{20}Ne reaction calculated for $2J^\pi = 3^-$ is $\omega = \frac{2}{3}$. As with the 7749 keV state, the resonance strength of the neutron channel can be calculated using literature values for the alpha width, once again from Table 2 in Ref.[37]. The resonance strength calculated assuming $2J^\pi = 3^-$ is $\omega\gamma_n = 0.36\mu$eV, a third lower than reported by Ref.[37] suggesting the ^{17}O(α,n)^{20}Ne is less favourable, reducing the reaction-rate ratio and so reducing the efficiency of the *s*-process in rotating massive stars. The values for alpha width reported in Ref.[30] are upper limits calculated from a Porter-Thomas distribution [105] and are therefore inappropriate to use in a direct comparison with this result for $\omega\gamma_n$. A Porter-Thomas distribution is based on experimental data and calculates the width of a resonance from the square of a Gaussian-random variable. The lower spin-parity reported by Ref.[30] produces the same value for the spin-factor as this result meaning that these studies would be in agreement if the Γ_α value from Ref.[30] was used to calculate resonance strength instead of the value from Ref.[37].

7980 keV

This state is a doublet of two levels at 7980 keV and 7982.1 keV. Because the state at 7982.1 keV has a reported J$^\pi$ of ($7/2^+$, $11/2^+$) [31] it was thought that in this study the main contribution would come from the 7980 keV state, since previously reported spin-parities for 7982.1 keV would mean ℓ-transfers of either 4 or 6 (respectively) and as this was a ^{20}Ne(d,p)^{21}Ne experiment the states with higher ℓ-transfers are not expected to be significantly populated. However, the ADWA analysis of the HELIOS data, shown in Fig.3.38, indicates the best fitting ℓ-transfers are either 5 or 6, which disagrees with the TUNL study assignment of $\ell = 1$. This discrepancy could have originated in the poor separation between this state and the nearby 8068 keV energy level, however, could also indicate that the 7982.1 keV energy level is more prominent than expected. After this state, the energy level density is high enough that, with

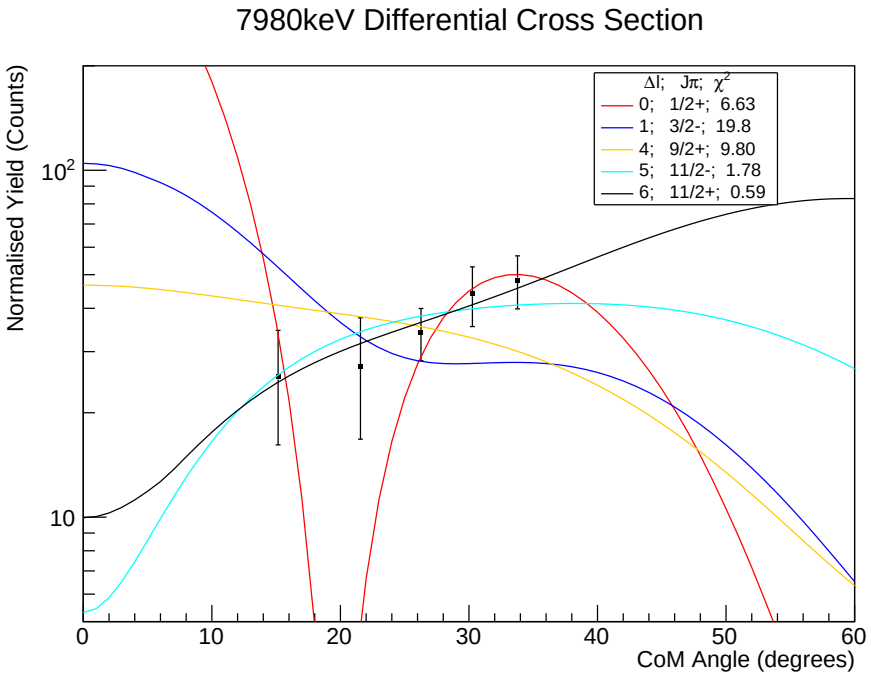

Figure 3.38: Measured differential cross section for the 7980 keV energy level compared to the five best fitting ℓ-transfer predictions and the χ^2 value of each fit. The best fitting predictions are $\ell = 5$ and $\ell = 6$.

the resolution of HELIOS, analysis of individual levels is not possible, therefore this is the last energy level that was analysed.

3.3.4 Summary

In summary, spin-parities have been determined for energy levels in ^{21}Ne using ADWA analysis of differential cross sections measured in a ^{20}Ne(d,p)^{21}Ne reaction. Results have generally shown agreement with measurements reported in literature. Two energy levels of particular interest to the s-process in rotating massive stars are 7749 keV and 7820 keV, which had either unknown or uncertain spin-parity assignments prior to this study.

The differential cross section of the 7820 keV state was best described with an $\ell = 1$ transfer. By combining data from this experiment and a previous study [30] the neutron widths of 7820 keV and 7749 keV were estimated. These estimates for width were compared to literature to rule out a spin-parity of $\frac{1}{2}^-$ for the 7820 keV state, therefore the assignment of $J^\pi = \frac{3}{2}^-$ was made. The ^{17}O(α,n)^{20}Ne resonance strength for the 7820 keV state was calculated to be $\omega\gamma_n = 0.12\,\mu$eV; this result is in agreement with theoretical calculations in literature. The estimate for neutron width was 7600(2100) eV. A previous neutron resonance experiment [102] observed other states with similarly wide resonances yet did not report a state at 7820 keV;

this discrepancy suggests a future investigation into the neutron resonances of ^{21}Ne could be warranted.

The spin-parity for the 7749 keV state could not be determined in this study due to high uncertainties in the differential cross section, which had their origin in the low statistics of the data. Despite this, an upper limit of $\Gamma_n < 7200$ keV for the neutron width was determined by assuming an $\ell = 1$ transfer. This assumption was justified based on a previous observation showing that the 7749 keV state was narrow, thus excluding an $\ell = 0$ transfer. A minimum resonance strength for ^{17}O(α,n)^{20}Ne was determined as $\omega\gamma_n < 7.2 \times 10^{-3}$ μeV, which is a factor of three below what has previously been assumed in reaction-rate models that used theoretical calculations from literature and suggests a reduced rate of ^{17}O(α,n)^{20}Ne reactions. A reduced rate of reaction implies the *s*-process is less efficient in rotating massive stars than has previously been assumed in models due to more efficient neutron poisoning by ^{16}O.

Determining the overall impact of these results on predictions for *s*-process nucleosynthesis in rotating massive stars would require computer simulations using these results to update the model. Ideally these simulations would also include new measurements for alpha widths, which remain a source of uncertainty in models, as well as new measurements for gamma width which combined with these results for neutron width would improve Γ_n/Γ_γ estimates. Two separate studies are currently underway aiming to measure both alpha widths and gamma widths using the ^{17}O(^{7}Li,t)^{21}Ne reaction [106, 107].

Chapter 4

^{86}Kr(α,n)^{89}Sr for the Weak *r*-process

4.1 The EMMA Recoil Mass Spectrometer

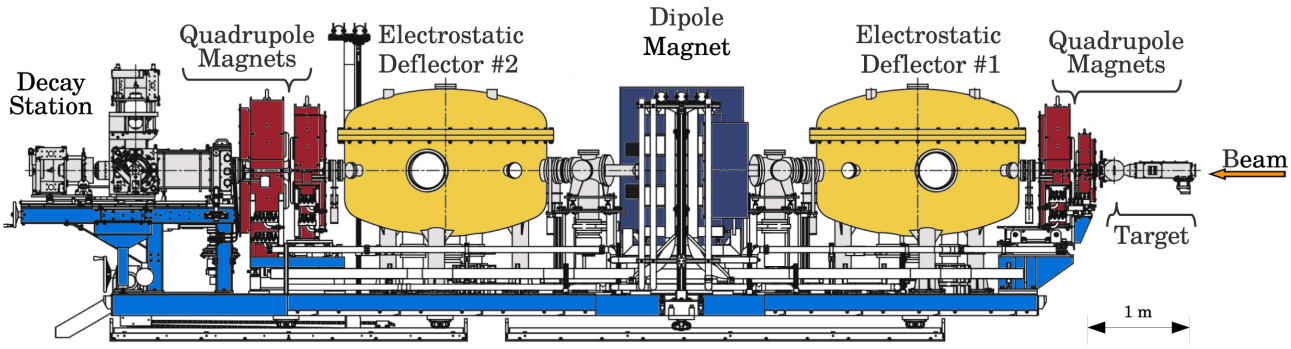

Figure 4.1: The Electromagnetic Mass Analyser with the field generating sections labelled [108].

The Electromagnetic Mass Analyser (EMMA) is part of the ISAC-II facility at TRIUMF in Vancouver, Canada. It is a recoil separator designed for studying nuclear reactions, often in inverse kinematics (cf. Chapter 2.1.2), and its role is to separate ions recoiling from a nuclear reaction by their mass-to-charge ratio (M/q value) and disperse them accordingly across the focal plane. By passing the recoiling nuclei through a series of electric and magnetic fields (cf. Fig.4.1), the trajectories of the recoils are deflected and the scale of that deflection is proportional to the deviation of the M/q value of each ion with respect to the set value. At the end of EMMA, quadrupole magnets focus the ions onto the focal plane of the spectrometer where the recoils are detected [108]. Recoiling ions with different mass-to-charge ratios are dispersed across the focal plane and can be identified using the x-position at which they are detected.

The deflection induced by EMMA on recoil trajectories is quantified by the Lorentz equation

$$\boldsymbol{F} = q(\boldsymbol{E} + \boldsymbol{v} \times \boldsymbol{B}) \tag{4.1}$$

which describes the force exerted on a moving ion in an electromagnetic field. In Eq.4.1, q is the charge of the ion, $\boldsymbol{v}$ is the velocity of the ion, $\boldsymbol{B}$ is the transverse magnetic field, $\boldsymbol{E}$ is the transverse electric field and $\boldsymbol{F}$ is the resulting force. When a moving charge enters either a magnetic or an electric field the force exerted upon it is centripetal in nature and the Lorentz equation can be substituted into

$$F = \frac{mv^2}{r} \tag{4.2}$$

to find the radius of curvature, r, for an ion moving through either type of field. In Eq.4.2, m is the mass of the particle, F is the magnitude of the centripetal force on the particle, v is the magnitude of the velocity of the particle.

The result for a magnetic field is

$$r = \frac{mv}{q|\boldsymbol{B}|} \tag{4.3}$$

and for an electric field

$$r = \frac{mv^2}{q|\boldsymbol{E}|} \tag{4.4}$$

By appropriately setting the strengths of the fields generated by the electrostatic deflectors and the dipole magnet, EMMA can be tuned to disperse a specific range of M/q values across the focal plane and, importantly, to screen out undesired isotopes such as the unreacted beam. EMMA is also equipped with a series of slits which can be moved in and out as required to block certain trajectories thus preventing all recoils except those with a given M/q value from reaching the focal plane.

EMMA can be used with either stable or radioactive beams. Stable beams originate in OLIS (the Offline Ion Source), whereas radioactive rare isotope beams (RIBs) are developed using the Isotope Separation On-Line (ISOL) technique. This method first directs a beam of protons accelerated by the TRIUMF 520 MeV cyclotron into a target (such as Uranium Carbide); some target nuclei are fragmented into various nuclides which are ionised, magnetically separated and the desired isotope extracted.

As ^{86}Kr is a stable isotope, OLIS [109] was the source for the beam in the ^{86}Kr(α,n)^{89}Sr experiment. OLIS is designed to ionise gaseous atoms using either a microwave-cusp ion source, a charged surface or a hybrid source comprised of a ionising surface and an arc-discharge circuit. For atoms that are not gaseous under standard conditions, a set of ovens can be used to evaporate them beforehand. During this experiment, the microwave source was used to ionise

the ^{86}Kr atoms to a distribution of charge states centred on 14+. Secondary stripping of the ^{86}Kr ions was also required to push the beam ions' central charge state to 20+ by passing the beam through a thin foil which removes yet more electrons from the ions, further increasing the charge state of the beam.

The target chamber of EMMA contains the target wheel, a Faraday cup and two silicon surface barrier (SSB) detectors set at 20^o to the beamline. SSB detectors are silicon detectors with their depletion region close to the front face of the detector. This is achieved by making the silicon wafer mostly from n-doped silicon, with only a thin layer of p-doped silicon. A thin film of gold is evaporated onto the surface to act as an electrode for the electronic readout. For more on silicon detectors, see Chapter.3.1.1. The SSBs detect elastically scattered ions which are used for beam normalisation as well as for online monitoring of target composition. The total area of each SSB is 150 mm^2 [108], however, they can be fitted with apertures to restrict the surface area and prevent the SSBs being saturated by high rates of scattering (for example, beam scattering from gold-backed targets). For the ^{86}Kr(α,n)^{89}Sr experiment, circular apertures with a diameter of 3 mm were used to define the active area and prevent saturation of the detectors by the scattered beam without preventing the collection of sufficient statistics of scattered target nuclei for beam normalisation.

Focal-plane Detectors: the PGAC

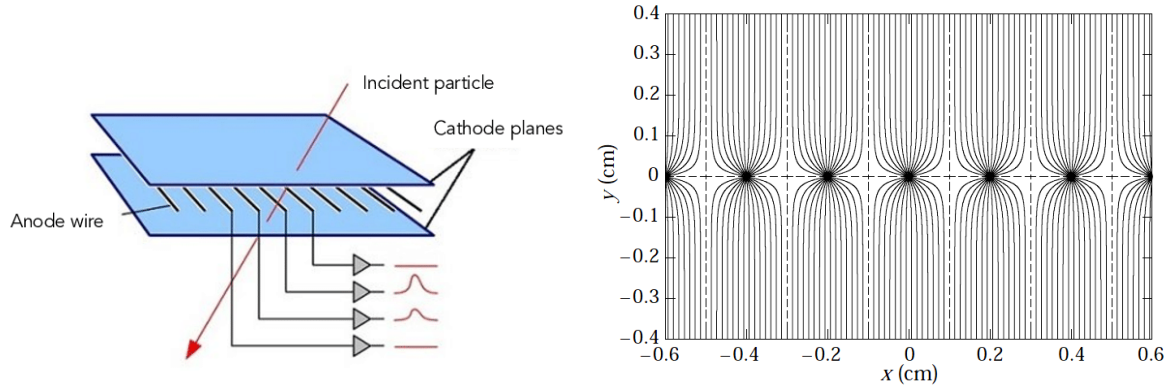

Figure 4.2: Left) Diagram of a position-sensitive parallel grid avalanche counter [110]. Right) Cross section of the electric field generated by a series of parallel anode wires such as are found in the EMMA PGAC [111].

There are several focal-plane detectors that EMMA can use but most important for this experiment is the position-sensitive parallel-grid avalanche counter (PGAC). The PGAC provides information on the position at which each recoil impinges upon the focal plane, thus allowing for M/q determination [108]. It is filled with 2 Torr of isobutane gas contained by 0.9 μm mylar windows which have layers of aluminium on both sides, $10 - 75$ nm thick; the recoiling nuclei

ionise this gas as they pass through the PGAC. Dividing the PGAC chamber are three wire grids: the middle grid is positively charged whereas the front and rear grids are negative, as illustrated in Fig.4.2. The electric field lines produced in such a set up are mostly parallel to one another except very close to the wires themselves, again shown in Fig.4.2. The electrons released in ionisation events accelerate towards the positive wire grid (the anode) and induce a signal on the wires as they move towards them. The positive ions drift to the cathodes. Which wires register a signal depends on the position in the chamber that the initial ionisation occurred: providing for position sensitivity in the detector. The signal registered by these wires is amplified by Townsend avalanches, which is an effect where by electrons released in the primary ionisation reaction accelerate towards the anode wire and collide with neutral gas particles that are ionised by the collision. The secondary electrons released in these collisions increase the charge collected by the wires.

PGAC pulses are passed through a pre-amplifier and then an amplifier before being processed by the data-acquisition (DAQ) system. The signals from the anodes are fed into a Constant Fraction Discriminator (CFD) and then a time-to-digital converter (TDC). Each wire in the cathode grid has a known read-out delay time depending on its position which is set by a inductor-capacitor circuit. After this delay, their signals are fed into a CFD and then on into a TDC. The anode acts as the trigger of the DAQ system and the start for the TDC signal. The time difference between the anode and the cathode signals are used to reconstruct the position information of each event.

Focal-plane Detectors: the Ionisation Chamber and the Si Detector

The remaining detectors at the focal plane are the ionisation chamber (IC) and a silicon detector. Between them, these two detectors provide energy loss and residual energy signals. The ionisation chamber operates in a similar fashion to the PGAC in that it is a chamber filled with isobutane gas at 2.5 – 10 Torr which is ionised when a heavy recoil passes through. The liberated electrons drift towards the anode which is positioned along the side of the chamber. The amplitude of the signal measured by the ionisation chamber is proportional to the energy lost by the recoil as it passes through the ionisation chamber. This proportionality is described in the classical model known as the Bethe-Bloch formula, which was introduced in Chapter 3.1.3 and is shown in Eq.3.4.

The focal-plane silicon detector can be either a 3000 mm^2 ion-implanted detector or a double-sided silicon strip detector, depending on the needs of the experiment [108]. When in use, it is set behind the ionisation chamber to record the residual energy of ions after they have passed through both the PGAC and IC. The ions that impinge upon the silicon generate a number of electron-hole pairs proportional to the energy deposited into the detector. The electrons are

excited into the conduction band of the semi-conductor and the voltage pulse is recorded by the DAQ. The SSBs in the target chamber work according to the same principle. When used together, the IC and the focal plane silicon detector yield $\Delta E - E$ measurements which, with the Bethe-Bloch formula, help identify the proton number of the recoiling nuclei.

4.1.1 The TIGRESS Gamma-ray Spectrometer

The TRIUMF-ISAC Gamma-ray Escape Suppressed Spectrometer (TIGRESS) can be coupled to EMMA to allow for the detection of gamma rays produced in nuclear reactions in the EMMA target chamber [112]. By measuring both gamma rays and recoiling nuclei, coincidence gates can be placed on the data to improve the signal-to-noise ratio on the gamma-ray energy spectrum measured by TIGRESS for a specific recoiling nucleus detected by EMMA. Coincidence gating involves vetoing any gamma ray that was detected in TIGRESS but did not coincide with an event on the EMMA focal plane within a certain time frame.

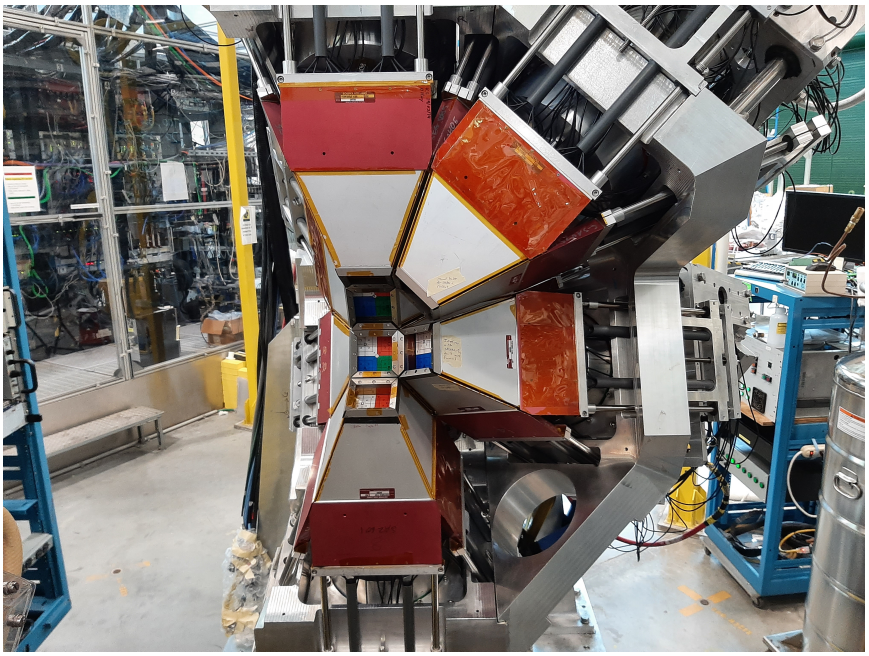

Figure 4.3: A picture of one half of the TIGRESS array from the point of view of the EMMA target chamber.

In this experiment, TIGRESS consisted of twelve High-Purity Germanium (HPGe) clovers, four set at an angle of 135° and eight at an angle of 90° [113]. These angles give the array maximum angular coverage, while still allowing TIGRESS to couple to EMMA. The need to couple to EMMA preventing additional HPGe detectors being placed at more forward angles. Each clover is comprised of four HPGe crystals and is surrounded by Bismuth Germanate (BGO)

scintillator shields which are used to suppress Compton scattering. The clovers within can be pushed forward past the shields to maximise detection efficiency or kept withdrawn behind the BGO shields to maximise the peak-to-noise ratio [114]. In the ^{86}Kr(α,n)^{89}Sr experiment the BGO clovers were withdrawn behind the Compton suppressors. TIGRESS can be seen in Fig.4.3, which shows half of the array. TIGRESS is divided into two wings which can be pulled back to allow access to the EMMA target chamber. Each clover consists of thirty-two segments which provide position sensitivity and are shown in Fig.4.4. Each segment has one readout and each crystal has an additional readout for the full-energy signal. The thirty-six readouts for each clover, plus the twenty readouts from the suppressors, are fed into a pre-amp and then into a 100 MHz flash ADC which digitises the signal. The signal is then passed through a field programmable gate array (FPGA), allowing pulse shape analysis and extraction of information on the timing and shape of the pulse. The timing of each signal is of particular importance when coupled to EMMA since it is needed to determine whether events in EMMA and TIGRESS are coincident.

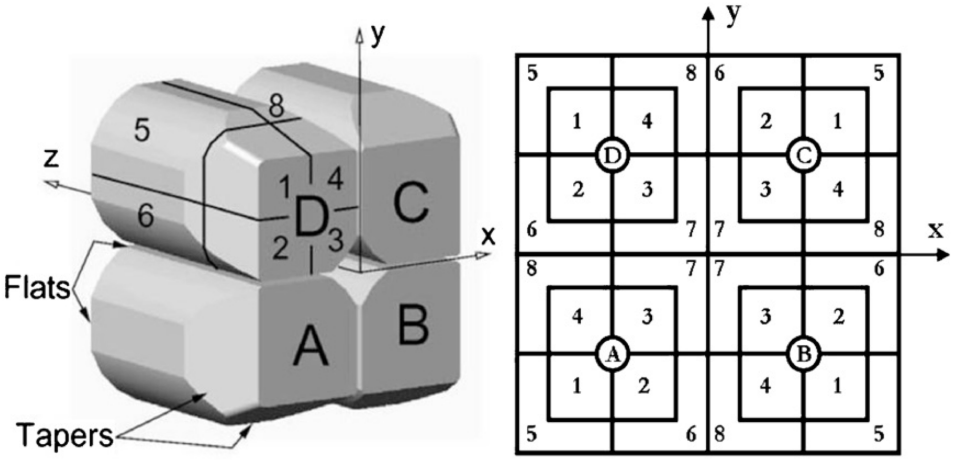

Figure 4.4: Diagram of a TIGRESS clover showing the segmentation of the readout for each crystal [114].

Like the silicon detectors discussed previously, high-purity Germanium detectors are semiconductors. HPGe arrays are preferred for the detection of gamma rays and X-rays owing to the higher atomic number of germanium, which makes the mean free path of a photon shorter than it would be in silicon and therefore reduces the physical size of the detector that is needed. Another advantage of HPGe is that less energy is required to generate an electron-hole pair: 2.9 eV compared with 3.6 eV for silicon, giving germanium based detectors much better resolution. The downside of these detectors is that they must be cooled to around 77 K to reduce thermal generation of electron-hole pairs.

The BGO scintillators are used as a veto to suppress Compton scattering; that is, the

scattering of photons from electrons within the HPGe crystals themselves. It is necessary to attempt to suppress this phenomenon because the scattered photons that leave the detector will not transfer their full energy into the germanium and thus represent incomplete measurements, this Compton background must be accounted for in the analysis. The BGO scintillators are used in shields that surround the HPGe clovers and detect those Compton scattered photons that escape the HPGe crystals. A scintillator such as bismuth germanate has a high atomic number and when a photon passes through it excites electrons in the crystal. The excitation of the electrons in the scintillator leads to a flash of light, or luminescence, when the electrons de-excite. The flash is read out using a photo-multiplier tube (PMT). A photo-multiplier tube consists of a photo-cathode, which releases electrons through the photoelectric effect when a photon impinges upon it. These photo-electrons pass through the PMT, interacting with a series of dynodes that multiply the number of electrons associated with the original photon thus amplifying the signal. These electrons are collected to form an electrical signal which is recorded by the DAQ. Detections from the BGOs allow any coincident signals in the HPGe detectors to be vetoed, removing a significant source of background events.

4.1.2 Helium-containing Targets

The targets used the ^{86}Kr(α,n)^{89}Sr experiment are a recent development and were first described in Ref.[115]. They have a helium density comparable to gas targets, reported to be 3.3 – 5.4 $\times 10^{18}$ atoms cm^{-2}, but avoid the drawbacks of expensive pumping stations, such as are needed for windowless gas-target set ups, and the issues that arise from using gas-target chambers, in particular the introduction of contaminant nuclei in the chamber window as well as the loss of energy and intensity by the beam as it passes through the window. Since these targets are relatively new, practical considerations arising from their use are still being investigated. Concerns include: whether heavy ion beams would cause the He atoms to leak from the targets due to heating, the physical stability of the targets (brittleness) and contamination during fabrication, although any contamination can be quantified by proton elastic back-scattering experiments.

These targets are fabricated through magnetron sputtering silicon onto a sodium chloride backing in the presence of helium. This technique produces a silicon matrix which contains helium in pores throughout the foil, as can be seen in Fig.4.5. The NaCl backing is then dissolved in water leaving only the self-supported Si:He foil behind. The density of the original targets was determined using proton elastic back-scattering. Ref.[115] reported the results when different He pressures were used in the production of these targets and found that medium pressure

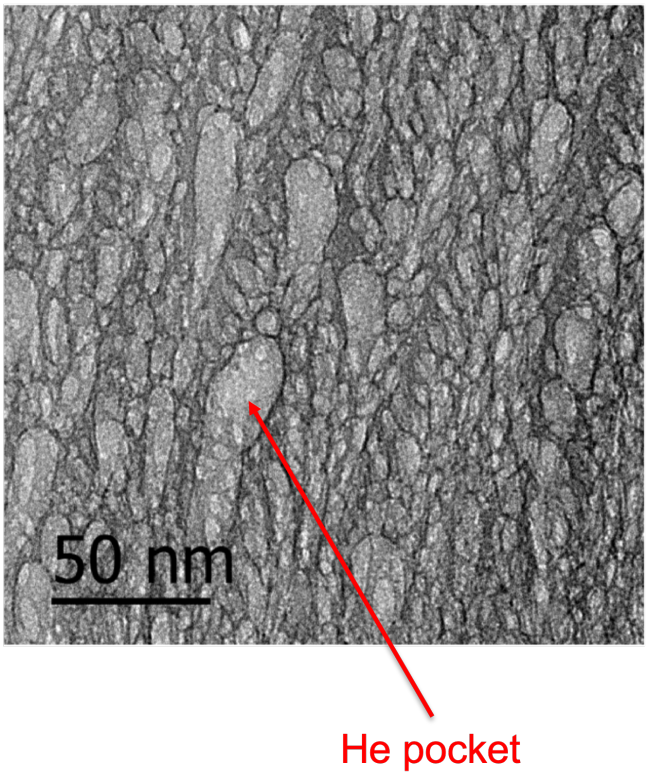

Figure 4.5: The appearance of the novel helium containing targets under a transmission electron microscope, with the He pocket labelled [115].

conditions (4.9 Pa) were optimal for maximising helium content. Two years later another proton back-scattering experiment on the same targets yielded the same results, demonstrating stability over time [115]. The scattering cross section determined for these targets was in good agreement with literature, confirming their viability for use in reaction experiments [115].

Given the high helium density and stability of these targets, they are of interest for use in inverse-kinematics reactions. The ^{86}Kr(α,n)^{89}Sr reaction was the first time a reaction other than scattering has been studied using these targets. The targets used in this experiment had a thickness of 2.6(1) μm and a density of 1.465(73) gcm^{-3} and were produced and characterised by the University of Seville researchers. The measured ratio of He to Si in these targets was 0.44 He:Si, which gives an equivalent helium density of 3.38×10^{18} atoms cm^{-2} with an associated uncertainty of 5%.

4.1.3 Experimental Setup

The experiment targeted the upper limit of the energy range of astrophysical interest for the ^{86}Kr(α,n)^{89}Sr reaction. The beam energy was set to 223 MeV producing a centre-of-mass reac-

tion energy of 9.583 MeV, which is the most favourable energy for ^{86}Kr(α,n)^{89}Sr reactions in an astrophysical site at a temperature of T = 4.95 GK according to Eq.2.2. EMMA was set for a central trajectory of $^{89}Sr^{20+}$ ions with an energy of 107.8 MeV. The fields were set for rigidities of $R_E = 10.77$ MV and $R_B = 0.7049$ Tm in order to bend the recoils. The slits of EMMA were used to block beam trajectories not associated with $^{89}Sr^{20+}$, effectively placing a mass gate on which recoils reach the focal plane. The final slits were opened to a width of 15 mm. The recoils emerged from the target in a range of charge states, among which 20+ was strongly populated.

The PGAC was set up at the focal plane, as was the Ionisation chamber and the focal-plane silicon detector. The Ionisation chamber and the focal-plane silicon detector were not needed in the later analysis as the ^{89}Sr gamma-ray energy spectrum was sufficiently isolated without them. As stated, the SSB detectors were set at 20° with 3 mm apertures restricting their effective area. Two targets were available for use in this experiment and were installed on the target wheel, these were made in the same batch and therefore had the same nominal thickness. The 2.5 μm gold degrader was placed on the 3°$\times$ 3° aperture downsteam of the target to reduce recoils' kinetic energies such that EMMA would be able to bend their trajectories. It is unusual to place the degrader on the aperture, since the aperture is normally used to restrict the entrance angles of the ions entering EMMA and by fixing a foil of high Z material such as gold to the aperture the benefits of this angular restriction were lost, particularly since the scattering was dominated by the degrader. However, because the targets in this case were self supported, the scattering of the recoils in the targets was not expected to result in deflection of recoils beyond a laboratory angle of 2° (based on simulations in GEANT4), therefore the aperture was not needed whereas the degrader was and the aperture provided a convenient place to mount the gold foil.

4.2 Data Analysis

The data from the ^{86}Kr(α,n)^{89}Sr experiment were sorted into histograms using the GRSISORT code [116]. The ultimate aim of the analysis was to deduce the cross section using Eq.2.1. The target density was known, so the only remaining values required were the measured yield, beam intensity and the experimental efficiency.

The first step of the analysis was to plot a histogram showing counts against the time difference between events in EMMA and TIGRESS to look for a coincidence peak. EMMA was tuned to select $^{89}Sr^{20+}$ recoils (and the slits were extended to block other M/q values) which effectively placed a mass gate on the data, however, because the scattered beam was not suppressed perfectly background was present. Then, the coincidence peak was used to remove

the time-random background in the energy spectrum measured by TIGRESS. Gamma rays known to originate from ^{89}Sr, and which are therefore associated with the (α,n) reaction, were identified and the number of counts observed for each gamma ray was calculated by fitting a Gaussian function and a linear background to the energy spectrum. This number was less than the total number of reactions that took place, partly because of efficiency losses but also because not all reactions released that particular gamma ray. After that, the beam normalisation was performed and the various experimental efficiencies were calculated in order to finally calculate a partial cross section which represented the probability of populating the energy level whose de-excitation produced the gamma ray used to tag the reaction. To compare this partial cross section to model predictions, it was necessary to combine information on the branching ratios of the ^{89}Sr energy levels with the predicted cross section for reactions leading to a recoil in a particular excited state. Using information on the gamma-decay branching of ^{89}Sr from Ref.[31] and cross section predictions calculated using Hauser-Feshbach theory, the measured partial cross sections for ^{86}Kr(α,n)^{89}Sr were compared to predictions.

4.2.1 EMMA-TIGRESS Coincidence Time

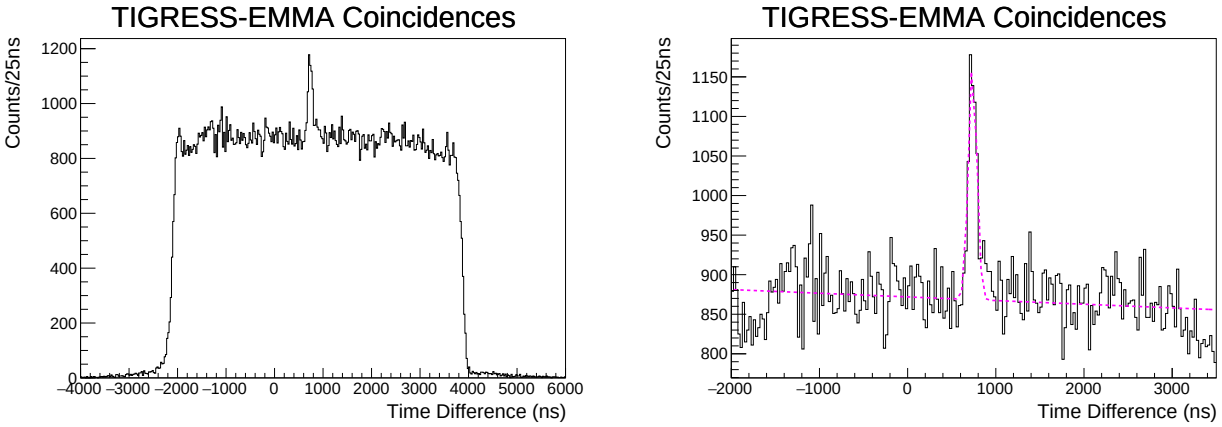

Figure 4.6: Left) Time difference between events registered in EMMA and TIGRESS. Right) Close up of the same spectrum, with a Gaussian fit to the (α,n) coincidence time peak, $\chi^2 = 294$.

As discussed in Chapter 4.1.1, EMMA and TIGRESS can be used together to remove the random background counts measured over the course of the experiment which otherwise would make analysis either difficult or impossible. The principle was that any background events recorded by EMMA and TIGRESS would be uncorrelated in time, simply being random coincidences between scattered beam particles and gamma rays released either in unrelated nuclear interactions in the target chamber or with gamma rays released naturally, such as

in the decay of ^{40}K. These random coincidences were not related to nuclear reactions and needed to be cut from the data. When an (α,n) reaction did take place the recoiling nucleus would emit gamma rays that could be detected in the HPGe crystals of TIGRESS. Each ^{89}Sr nucleus recoiled from the reaction with a known range of possible kinetic energies and would take a corresponding time to pass through EMMA before it could be detected at the focal plane. The average time-of-flight between EMMA and TIGRESS was 580 ns. However, the total time difference includes factors such as cable length, electronic processing of the signals and detector latency period, all of which delay the signal from EMMA and so the total time difference averaged 740 ns. The time delay between the detection of an ^{89}Sr gamma ray and the detection of the correlated recoil stood out from the random background as a peak of coincident measurements, as can be seen in Fig.4.6. This coincidence peak was used to place a coincidence gate on the data when plotting the gamma-ray energy spectrum. It could also be used to inform sampling of the time-random background. The gate used in this analysis is shown in green on Fig.4.7 and the limits were defined as being 2σ from the centroid of the coincidence time peak. The values for σ and the centroid came from the Gaussian fit shown in Fig.4.6. The fit includes a linear function to describe the random-coincidence background events; varying the slope of this line, while impacting the result for the yield under the peak, did not significantly affect the result for σ and therefore did not significantly affect the position of the timing gates. Setting the gates this close to the peak was an attempt to maximise the signal-to-noise ratio when background subtracting, however, introduced an efficiency loss of approximately 5%, since the 2σ gate will only include 95% of the coincidence timing peak.

The $\Delta E - E$ functionality of EMMA was not used in the end since the small number of ^{89}Sr recoils prevented their tracks from being identified. Attempts estimate their position on the $\Delta E - E$ plot resulted in a reduction in the relative height of the coincidence time peak above the time-random background. The coincidence time peak is shown in Fig.4.6. Concerned that attempting to gate on the $\Delta E - E$ was resulting in valid ^{89}Sr events being cut from the data, attempts to use the $\Delta E - E$ data as a gate were abandoned.

4.2.2 Energy Spectrum

Because the nuclei that emitted gamma rays were moving, the frequencies of the gamma rays were Doppler shifted and therefore, before the energy spectrum could be plotted, their measured energies ($E = h/\nu$) were corrected. The Doppler correction was performed using the equation

$$\nu_{obs} = \frac{\nu_s}{\gamma(1 + \beta cos\theta_{obs})} \tag{4.5}$$

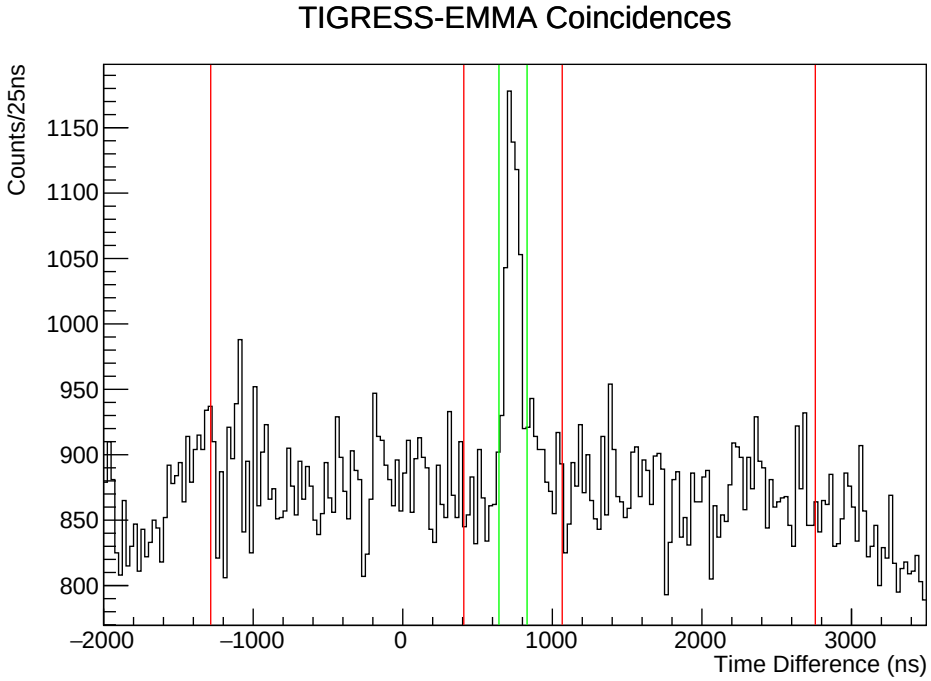

Figure 4.7: Time of flight plot including the gates set both on the coincidence peak (green) and on the random background (red).

Where, ν_{obs} is the frequency of a gamma ray observed in the Laboratory frame, ν_s is the frequency in frame of the gamma ray in the moving frame of the source, $\beta = \frac{v}{c}$ is the speed of the source in the laboratory frame in units of the speed of light in vacuo, $\gamma = \frac{1}{\sqrt{1-\beta^2}}$ is the Lorentz factor and θ_{obs} is the angle of observation. In the ^{86}Kr(α,n)^{89}Sr experiment $\beta = 0.075$, calculated from the beam energy of 223.6 MeV.

Since Eq.4.5 depends on the angle with respect to the beamline, the exact orientation of each HPGe crystal in the TIGRESS array matters. Because each clover consisted of four crystals they each covered two angular bins. Those bins were centred on: 80°, 100°, 125° and 145° [113] covering ranges of: 76.6° – 88.0°, 92.0° – 103.6°, 121.6° – 132.1° and 136.5° – 147.8° , respectively [117]. In addition, the crystals are further subdivided into eight segments (cf. Fig.4.4), each with a given angular coverage within those ranges and therefore a different Doppler correction was necessary for each ring of segments. Fig.4.8 shows the result of applying the Doppler correction to the gamma-ray energy spectrum as measured by TIGRESS. Since the strongest room-background peaks were emitted by stationary sources in the laboratory frame, when the Doppler shift was applied to the measured spectrum these background peaks were shifted along with the signal peaks.

The Doppler correction caused the recoil gamma rays measured by each detector to be combined into one peak but also caused the background peaks to be spread into different peaks

on the Doppler corrected spectrum, one for each ring of segments. For example, the decay of ^{40}K released a gamma ray at 1460 keV; in the uncorrected TIGRESS spectrum this narrow peak is strongly populated, but after the Doppler correction is applied the peak is spread out across several energies, as shown in Fig.4.8.

The segmentation of TIGRESS allowed for a much more precise Doppler correction than would have been possible if four crystals had been used as a whole, since the segments have a reduced angular coverage compared to a full crystal. Weighting for the different surface area of each segment, the resolution of the Doppler corrected peaks is improved by a factor of 3 due to the crystal segmentation.

Background Subtraction

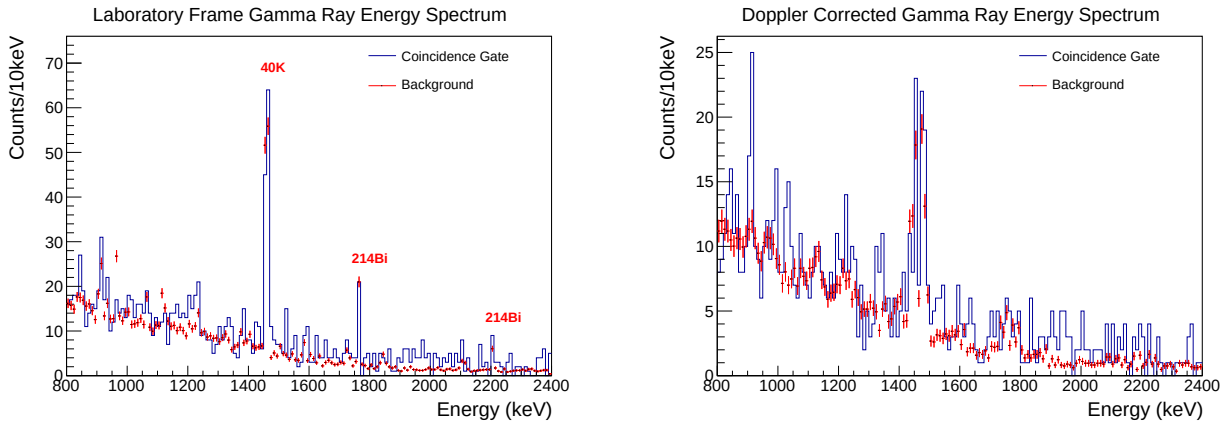

Figure 4.8: Left) Laboratory frame gamma-ray energy spectrum compared to time-random background with no Doppler correction. Right) Doppler-corrected rest frame gamma-ray energy spectrum compared to the time-random background which still remains.

The next step was to remove the random background from the energy spectrum. Uncorrelated gamma rays can be seen in Fig.4.9 as the horizontal lines indicating the same gamma ray is being observed by TIGRESS across multiple coincidence times between TIGRESS and EMMA, suggesting that these gamma rays are released independently of the reaction being studied. One way to estimate the background would be by placing gates on the time difference plot in Fig.4.7 to either side of the coincidence peak before normalising and subtracting the resultant spectrum from that produced when gating on the coincidence peak. During analysis, however, this approach did not fully remove certain peaks known to have originated from room background, particularly the ^{40}K decay line at 1460 keV, the ^{214}Bi decay lines at 1764 keV and 2204 keV and the ^{208}Tl decay line at 2614 keV from the ^{232}Th decay chain. After some effort to reproduce the background by sampling either side of the time-of-flight peak, it was decided to

make use of these room-background gamma rays. The background was sampled across a range of times-of-flight which are shown in red on Fig.4.7. The background was scaled to reproduce the height of the 1764 keV ^{214}Bi decay peak observed in the laboratory frame using the time difference gate; this is shown in on the left-hand panel of Fig.4.8. The 1764 keV transition was chosen rather than the larger 1460 keV peak as some events were expected from the 1473 keV gamma ray of ^{89}Sr. The result of this procedure was a background spectrum normalised to the prominent and well known 1764 keV ^{214}Bi decay peak which could then be shifted into the ^{89}Sr rest frame and used for background subtraction. The 2614 keV ^{208}Tl decay line was not chosen to normalise the background since it had fewer counts than the 1764 keV state and would result in a normalisation with a greater uncertainty. The ^{214}Bi line at 2204 keV was not used either, with the same justification.

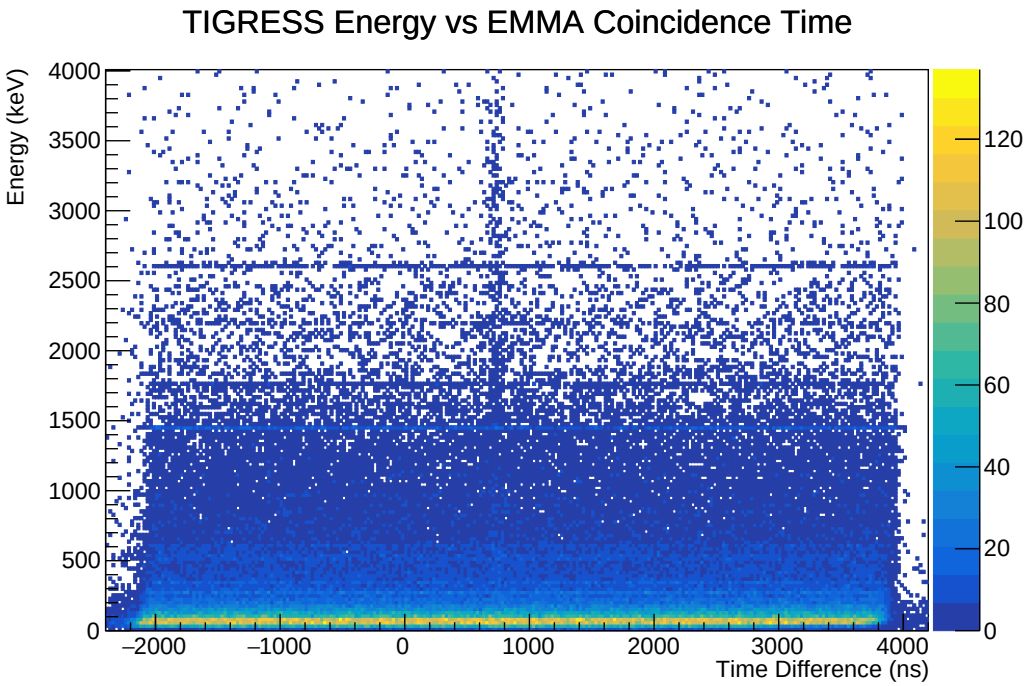

Figure 4.9: Doppler-corrected gamma ray energy vs EMMA-TIGRESS time difference.

Fig.4.10 shows the spectrum produced when gating on the signal region after the background has been subtracted. Note that there are counts below the zero line. Such negative counts are a result of the background having been estimated by statistical averaging.

Peak Fitting

Once the spectrum had been plotted it could be used to look for gamma rays known to be associated with electromagnetic decay of the ^{89}Sr nucleus. These gamma rays should appear as approximately Gaussian shaped peaks in the spectrum since the statistics here are low enough

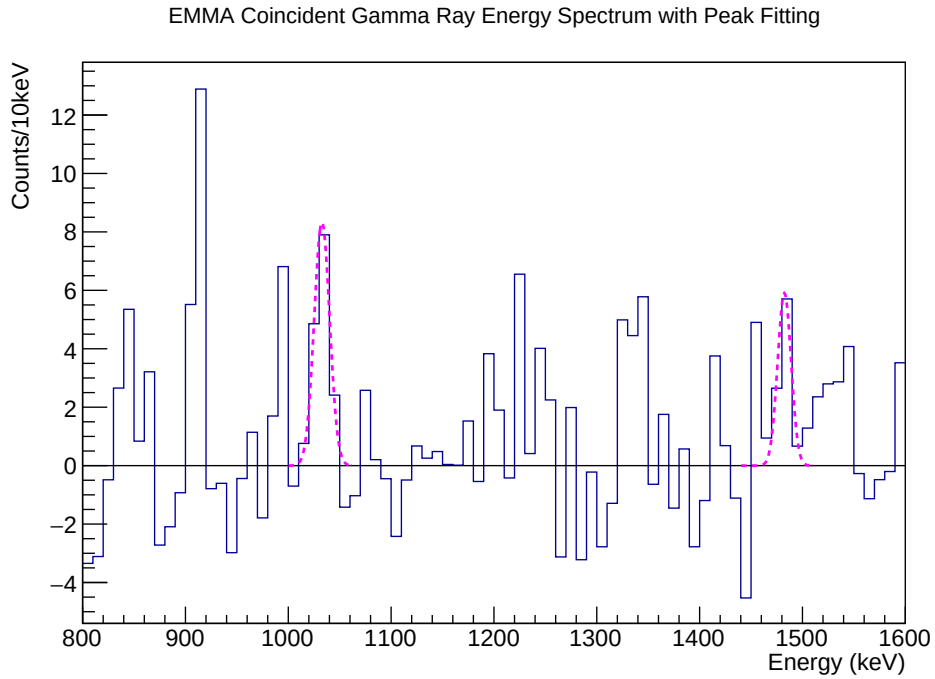

Figure 4.10: Background-subtracted, Doppler-corrected ^{89}Sr gamma-ray energy spectrum. $\chi^2(1032) = 66.9$ and $\chi^2(1473) = 71.2$.

that the low energy tail on the photopeaks can be treated as negligible. A previous experiment studied this same reaction in forward kinematics and reported the measured energy spectrum [118] without an associated cross section. That experiment was conducted at a slightly higher centre-of-mass energy than in this study and therefore the energy spectrum was not expected to be the same, because the relative strengths of each gamma ray vary with centre-of-mass energy (cf. Fig.3 in Ref.[118]). It nevertheless proved useful in informing this analysis. As can be seen in Fig.4.10, there is a peak at 1032 keV in these data which corresponds to a known gamma ray associated with the de-excitation of the first excited state of ^{89}Sr. By fitting a Gaussian to this peak, the number of 1032 keV gamma rays observed can be extracted from the spectrum. An alternative was to simply count the number of gamma rays in the bins around 1032 keV Fitting a Gaussian curve, however, to the data had advantages that shall be discussed in due course.

It should be noted that there are other gamma rays, besides 1032 keV, associated with ^{89}Sr expected in this energy region, one has an energy of 1025 keV and originates from the 2057 keV energy level. Since each bin covers 10 keV on the spectrum, the 1025 keV peak would be unresolved from the 1032 keV peak. Any fits of the 1032 keV peak are expected to include some contribution from this gamma ray and that must be accounted for when trying to calculate the cross section in the next step of analysis. The same procedure was followed for the gamma

ray expected at 1473 keV, the peak for which also included a similarly unresolved gamma ray at 1489 keV that originated from the 2962 keV state in ^{89}Sr.

The expected widths could be calculated using the equation for Doppler broadening

$$\frac{\Delta E}{\gamma} = E_\gamma^0 \beta \sin(\theta) \Delta\theta \tag{4.6}$$

Where ΔE is the broadened full width at half maximum (FWHM) for the gamma ray being studied, γ is the Lorentz factor, β is the magnitude of the velocity of the nucleus, normalised to the speed of light, E_γ^0 is the energy of the gamma ray in the source frame, θ is the angle of the detectors relative to the beamline and $\Delta\theta$ is the angle subtended by the detectors. The angles used were for each of the TIGRESS segment rings and are shown in table 4.1, along with their respective angular ranges. Doppler broadening has a greater impact on the higher energy gamma ray and therefore the same width could not be assumed for both peaks. The FWHM calculated using Eq.4.6 could be converted to the Gaussian σ parameter with the relation: FWHM $= 2\sqrt{2\ln(2)}\sigma$. The expected FWHM calculated for the 1032 keV gamma ray was 6.8 keV and for the 1473 keV gamma ray was 9.8 keV.

The Doppler broadened width calculated using Eq.4.6 was initially used in the fitting procedure for Fig.4.10, since fixing the widths of the peaks, and thus constraining the fits, was deemed desirable due to the low statistics of the data. Unfortunately, using widths calculated from Eq.4.6 resulted in a very poor fit for both peaks. It was decided therefore, to use these values as a lower limit for the peak widths and allow the fits to vary above that value until a reasonable fit to the data was achieved. These fits are shown in Fig.4.10 and the widths have values of 17.67 keV for the 1032 keV gamma ray, and 15.35 keV for the 1473 keV gamma ray.

Since the beam energy was below the Coulomb barrier for reactions with silicon (which has a barrier height of 81.2 MeV) the recoils observed should only be produced in the (α,n) reaction. However, Fig.4.10 shows there are several other features in this spectrum besides the 1032 keV and 1473 keV peaks. Although the background was subtracted in the previous step, that was an averaged sample and the actual background will not be perfectly represented. Therefore, the low statistics on Fig.4.10 means that some of these "peaks" could simply be fluctuations in the background, while others are genuine gamma rays. To be certain that the photopeaks being investigated were statistically significant Fig.4.10 was replotted, this time with the associated uncertainty on each bin to form Fig.4.11.

The statistical significance of the detection of the 1473 keV transition above the estimated background was 1.24σ (approximately 78% confidence level). This was our adopted detection threshold. Suspected photopeaks were fit with Gaussians which provided both the counts

Table 4.1: The assumed central angles of each ring of TIGRESS segments and their associated opening angles.

Segment Central Angle, θ (degrees)	Subtended Angle, $\Delta\theta$ (degrees)
79.6	5.7
80.4	3.8
84.2	3.8
85.2	5.7
90.0	5.8
91.9	3.9
95.7	3.9
100.7	5.8
124.2	5.3
125.2	3.5
128.7	3.5
129.5	5.3
139.3	5.7
140.3	3.3
144.1	3.3
145.0	5.7

under each peak and the uncertainty on those counts. It is important to note that the error bars on Fig.4.11 include the uncertainty propagated from the background subtraction. Those peaks observed in the spectrum are shown on Fig.4.12 and listed in Table 4.2 where they are compared to gamma rays originating from ^{89}Sr. Most of these peak locations do correspond to known gamma rays, which support the treatment of the 1032 keV and 1473 keV photopeaks as gamma rays. However, the photopeak at 993(4) keV did not match any known gamma ray in ^{89}Sr but was almost as strongly populated as the nearby 1032 keV peak. For further discussion see Chapter 4.3.

4.2.3 Beam Normalisation

Now that the measured yield had been found, the beam intensity, measured in particles per second (pps), for the entire duration of the experiment was calculated. The method used is

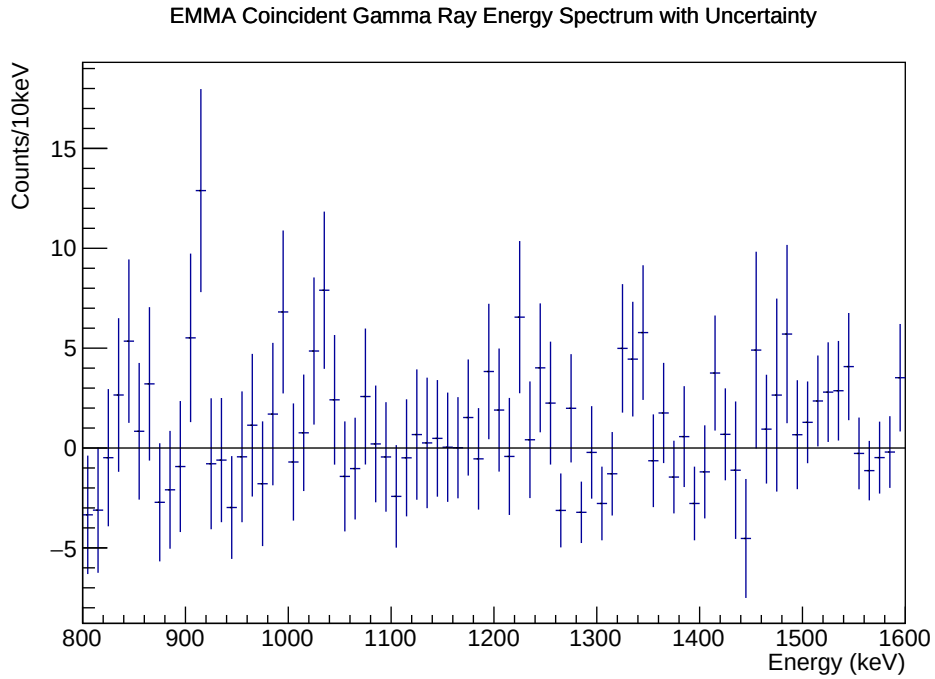

Figure 4.11: The uncertainties associated with the counts in each bin of the background-subtracted spectrum shown in Fig.4.10.

known as a relative beam normalisation.

The experiment was sub-divided into runs each of a known duration usually lasting an hour. Before each run a Faraday cup reading of the absolute beam current was taken. Current measurements had an associated uncertainty of 10%, which is comparable to experiments of a similar set up [119]. Over the course of the experiment, the current does not remain stable at a single value, rather it varies over time and scattering is used to infer the current. It was necessary to have an estimate for the average beam current to use to calculate the number of beam particles incident on the target, as required by Eq.2.1. To calculate the average beam current for the whole experiment, the rate of the scattered silicon calculated for the whole experiment was normalised to that for each individual run.

When a beam particle impinges upon the target, there is a probability of the incident particle reacting to produce ^{89}Sr, but there is a much higher probability of the beam particle simply scattering off the target. These scattered particles can be detected by the EMMA SSBs, which are positioned in the target chamber at 20^o to the left and right of the beamline. The cross section of nuclear scattering depends upon the atomic number of the nuclei involved and therefore there are independent cross sections for each of the nuclei in the target (He and Si). This Z dependence is shown in

Table 4.2: A list of gamma rays associated with ^{89}Sr detected with a significance of 1.24σ or greater above background compared to known gamma rays in the literature. Energies sourced from Ref.[31].

Measured Energy (keV)	Literature Energy (keV)	Confidence (σ)
843(7)	852	1.337
912(3)	906.0(1)	2.99
993(4)	?	1.71
1033(3)	1032.00(4)	2.28
1482(6)	1473.35(6)	1.63
1538(9)	1538.08(6)	1.71

$$\frac{d\sigma}{d\Omega} = \left[\frac{Z_1 Z_2 \alpha(\hbar c)}{4E\sin^2(\frac{\theta}{2})}\right]^2 \tag{4.7}$$

which is the equation for Rutherford scattering. Z_1 and Z_2 are the atomic numbers of the two interacting nuclei, E is the centre-of-mass energy, θ is the centre-of-mass scattering angle and α is the fine structure constant ($\alpha \approx \frac{1}{137}$ with $\hbar c \approx 197$ fm MeV). It should be noted that while the Rutherford scattering model describes the krypton and silicon scattering well, the centre-of-mass energy for krypton-helium scattering is above the threshold for being modelled purely with Rutherford scattering [120].

Eq.4.7 produces a cross section that can be used with

$$\text{Rate} = I_b N_t \Omega \left(\frac{d\sigma}{d\Omega}\right) \tag{4.8}$$

to calculate the expected rate of scattering for two nuclei at a given measurement angle, where I_b is the beam intensity in particles per second (pps), N_t is the areal target density for the nuclei in question and Ω is the solid angle coverage of the detectors.

Eq.4.8 was used to determine the beam intensity throughout the whole experiment by comparing the scattering of the beam nuclei to the scattering of the silicon nuclei in the target. The silicon was chosen over the helium because the scattering rate was higher which gave better statistics; also over time the helium in the target may deplete, whereas silicon would remain effectively constant. The helium content of the targets was monitored with the ratio of scattered helium to scattered silicon for each run, normalised to beam current and did not significantly change during the experiment. Plots showing the total scattering into each SSB

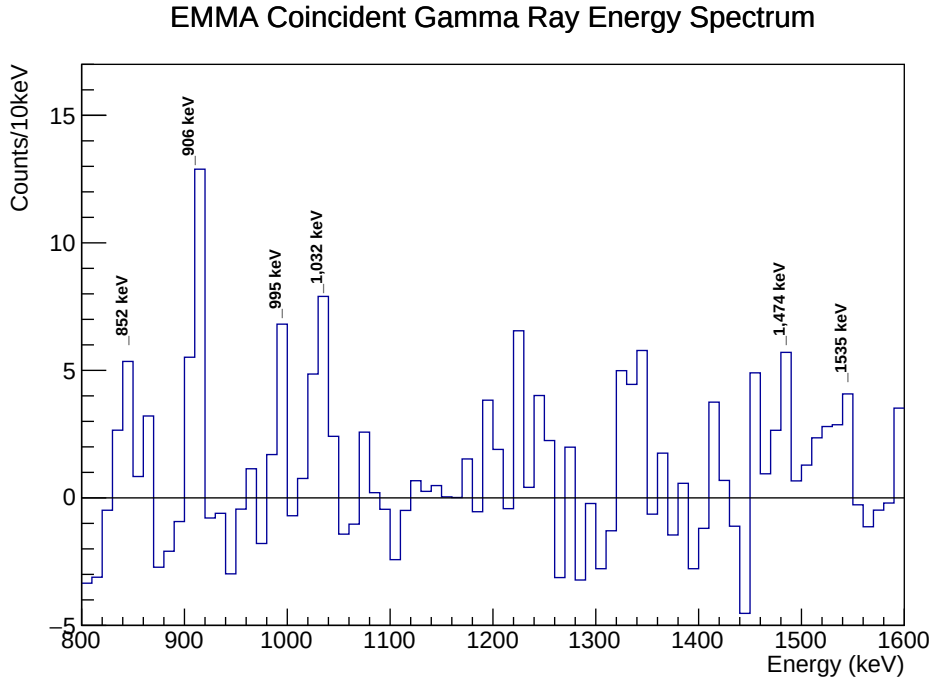

Figure 4.12: Background-subtracted, Doppler-corrected ^{89}Sr gamma ray energy spectrum from the reaction ^{86}Kr(α,n)^{89}Sr with observed gamma rays labelled.

are shown in Fig.4.13. The highlighted peaks each correspond to a different nucleus that has been scattered into the SSBs; red is the helium, green is the beam (krypton) and magenta is the silicon. The highlighting lines also indicate the ranges between which the SSB spectra were integrated to get the counts in each peak. These ranges were needed as although statistics in Fig.4.13 are good enough for a Gaussian fit, the spectra for individual runs could not be fitted reliably. An alternative option was simply to integrate all counts within a given range. This range needed to be consistent for each peak across all runs (and the summed spectrum) and it was preferable that these ranges be defined empirically. Therefore, a Gaussian function was fitted to each of the observed peaks in the summed spectrum and the integration limits were set to 1.25σ. This range was chosen as it was wide enough for statistical purposes but did not overlap with the integration ranges of the other peaks. The widths of the peaks depend on the kinematics of the scattering interaction, with different ions having different ranges of energies scattered across the 3 mm aperture of the SSBs.

Background in the He peak from the scattered beam did not impact the beam normalisation since the He was not used for that purpose; the He peak was only used to monitor the target content. While calculations for the ratio of He-to-Si counts did therefore include some background from scattered ^{86}Kr, so long as these ratios compared the same spectral bins the target content could be monitored, even if the exact He content was not accurately represented, the

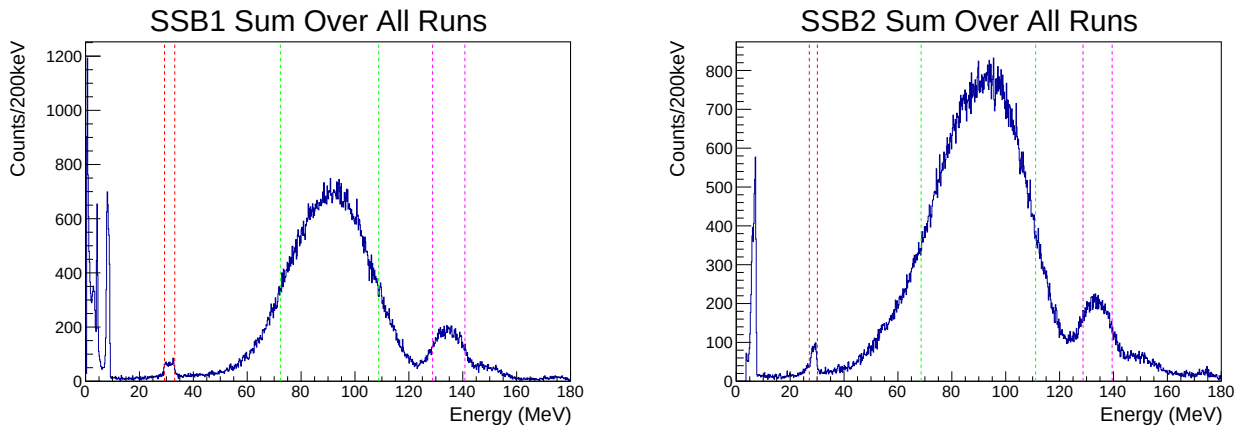

Figure 4.13: SSB energy spectra taken over the duration of the experiment. The red bracketed peak is the scattered helium, green is the ^{86}Kr and magenta is the scattered silicon.

trend in the ratio over time was what was important. The trend did not show a decrease over the course of this experiment suggesting the beam current was too low to significantly deplete the target; this will be discussed further in Chapter 4.3.

Relative beam normalisation uses the average rate of scattering from the whole experiment ($<$ Rate $>$), which is calculated by summing all scattered silicon detected by the SSBs and dividing by the total duration of the experiment, and dividing it by the rate of a single run Rate(i) to produce

$$< I >= I(i) \times \frac{< \text{Rate} >}{\text{Rate}(i)} \tag{4.9}$$

for the average current throughout the experiment. Because the current will vary somewhat during the course of any given run, the best estimate for average beam current, $< I >$, is to take the measured current for every run, $I(i)$, and find the mean. Fig.4.14 shows the normalised beam current calculated from the data for each individual run in the experiment. The average was 15.8(16) pA, which for ^{86}Kr ions was equal to $4.93(50) \times 10^6$ pps. The discrepancy between the earlier runs and later runs shown in Fig.4.14 will be discussed in Chapter 4.3.

4.2.4 EMMA Efficiencies

Compiling the various efficiencies of the experimental setup was the last stage of analysis before the cross section could be calculated. The TIGRESS HPGe detectors and the EMMA PGAC are not perfect and will only record a fraction of the true number of events. In addition, the EMMA spectrometer itself has certain associated efficiency losses that must be taken into

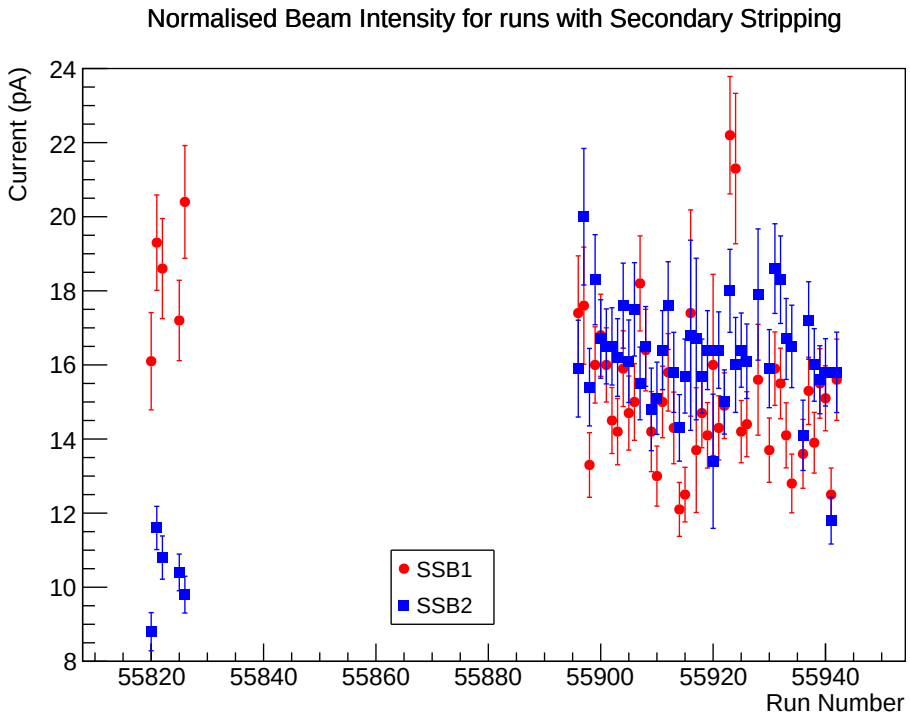

Figure 4.14: Normalised beam current calculated from each run in the experiment.

account.

The PGAC has a (relatively high) efficiency of 94.0 % [121]. This efficiency is a geometric transmission efficiency and arises from the presence of the wire grids in the PGAC gas volume. Should a recoil passing through the PGAC impinge upon one of these wires, it will be scattered or blocked. This represents an efficiency loss. The estimated efficiency of 94.0 % is calculated purely from the geometry of the PGAC and has a negligible uncertainty.

The EMMA detectors also have a livetime efficiency associated with the fraction of the time that the DAQ system is able to record events. The opposite is dead time, which is the time after an event during which the detector cannot record another event. The livetime efficiency for each individual run was calculated as the ratio of accepted triggers to presented. The total livetime efficiency for the experiment was calculated as an average of the measured livetime of each run and the uncertainty was calculated from the standard deviation. The value for this experiment was 86.3(31)%.

Charge State Efficiency

Recoils from the ^{86}Kr(α,n)^{89}Sr reaction emerge from the He:Si target and gold degrader with a range of charge states, each with a different associated M/Q value. EMMA is set up to screen out all but one of these M/Q values and therefore, there is an associated efficiency loss

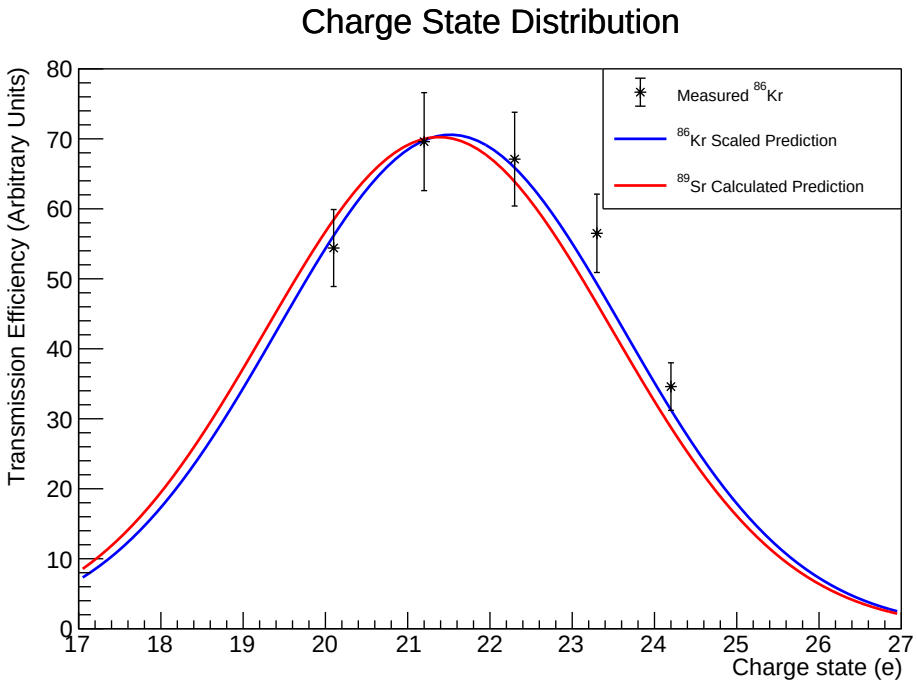

Figure 4.15: Shows the measured charge state distribution for the ^{86}Kr beam at a central energy of 125 MeV compared with the theoretical prediction calculated from Ref.[122], scaled to the measurements as described.

that must be determined.

A charge state distribution (CSD) is a plot of the transmission efficiency through EMMA for a given isotope with a varying charge state. Each charge state will be populated differently. The shape of a CSD can be modelled as a Gaussian distribution with the area underneath normalised to unity. The fraction of the total number of recoils that a given charge state makes up is known as the charge state fraction (CSF). This fraction needs to be estimated to determine the efficiency loss introduced by selecting only one charge state.

Estimating the CSF for the ^{89}Sr recoils required the CSD. This presents a problem since there are not sufficient numbers of recoils to directly measure the ^{89}Sr CSD. Therefore, the ^{89}Sr CSD must be estimated from a measurement of the ^{86}Kr CSD. The ^{86}Kr beam also emerges from the target and degrader with a range of charge states and unlike the ^{89}Sr recoils, the ^{86}Kr nuclei are sufficiently populous that the ^{86}Kr CSD can be measured.

To measure the ^{86}Kr CSD, EMMA was systematically tuned to a series of charge states in ^{86}Kr and the total number of nuclei that made it through EMMA was measured for each. After normalising to run time and beam intensity, the CSD could be plotted from these measurements, which are the data points shown in Fig.4.15.

Now the measured ^{86}Kr CSD was fitted with a Gaussian curve to find the measured values

for CSD centroid and width. These values were then compared to theoretical predictions, calculated using the model found in Ref.[122]. The model in Ref.[122] was chosen due to the good agreement for the CSD centroid value predicted by that model and the measurements conducted with EMMA. The model predictions for the centroid and width of the ^{86}Kr CSD were then scaled to match those of the measured CSD, with their uncertainties propagated as described in Appendix A. The reason for this step was to gain an estimate for the difference between the predicted CSD and the measured CSD and add this difference to the uncertainties on the predicted centroid and width. The scaled prediction from Ref.[122] is also shown on Fig.4.15.

Now that the uncertainty between the predicted and measured CSD had been established, it was time to turn to the ^{89}Sr recoils. The model was used to calculate a prediction for the ^{89}Sr CSD. Then, a ratio of the predicted ^{89}Sr CSD centroid to the ^{86}Kr CSD centroid was calculated (i.e. μ_{89Sr}/μ_{86Kr}) and used to multiply the measured ^{86}Kr centroid. This yielded an estimate for the value of the ^{89}Sr centroid which included the uncertainty between the measurements and predictions, after once more propagating the uncertainties in the manor in Appendix A. The same procedure was followed to estimate the width of the ^{89}Sr CSD. With these parameters now found, the ^{89}Sr CSD could be plotted, and the result is again shown on Fig.4.15.

Now that the ^{89}Sr CSD has been estimated, the CSF was simply the height of the CSD at the charge state that was used in the experiment. In this case, EMMA was tuned to the $^{89}Sr^{20+}$ charge state which had an associated efficiency of $15.06^{+3.42}_{-8.77}$ %. The CSD for ^{86}Kr was calculated for a central energy in EMMA of 125 MeV and the ^{89}Sr was calculated for a central recoil energy of 107.8 MeV. The lower energy value is due to the reaction, and different energy losses of the two nuclei.

Transmission Efficiency

Not all those $^{89}Sr^{20+}$ recoils will make it through EMMA. While, in theory, EMMA is tuned to accept a single M/Q value, the field strengths are calculated assuming that the recoils enter EMMA at zero degrees to the beamline. Due to the kinematics of the reaction and scattering in the target and (more significantly) the degrader, the recoils enter EMMA at a range of angles to the beamline. If a recoil's angle of entry is too large, it will not make it to the end of EMMA and will be stopped either by the slits of from impinging on the side of the beamline. This is another efficiency loss which must be estimated.

Estimating the transmission efficiency is a two-step process. First, a Monte Carlo simulation was conducted to simulate the energy loss and multiple scattering of the recoils as they leave the target and pass through the degrader foil; which, in this experiment, was mounted 8 cm downstream of the target. The Monte Carlo simulations were carried out using GEANT4 [123,

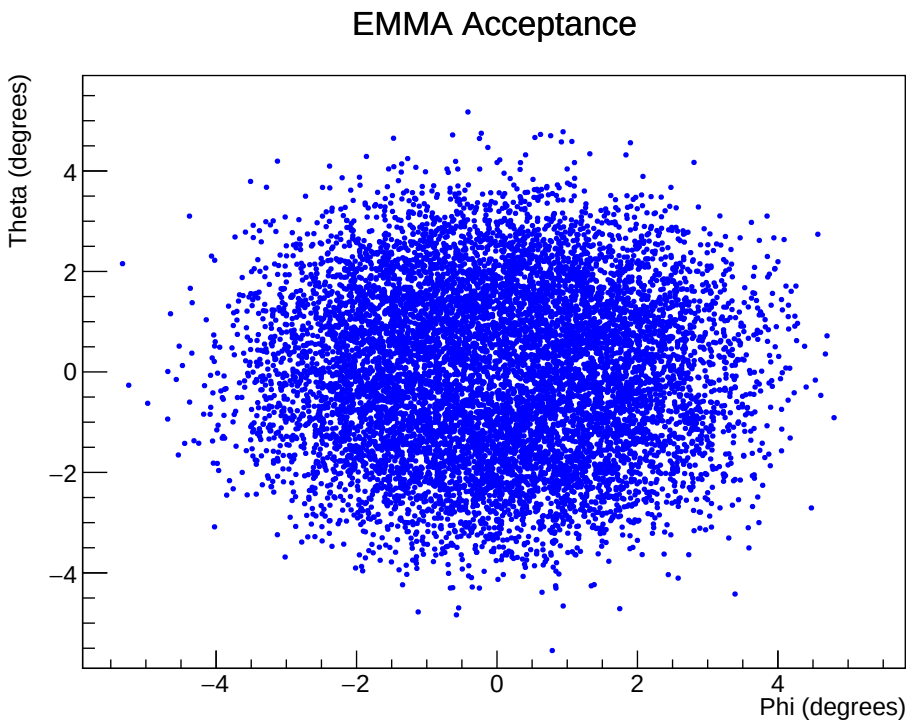

Figure 4.16: Horizontal (Phi) and vertical (Theta) projections of the scattering angles in spectrometer coordinates for simulated recoils after multiple scattering from the target and gold degrader in EMMA.

124, 125] and calculated the trajectories for 10,000 simulated recoils. Fig.4.16 shows the results of that simulation, and shows the angle at which each recoil enters EMMA, with θ being the horizontal projection of the scattering angle and ϕ being the vertical projection of the scattering angle.

With these simulated recoils, a second simulation was then run. This second simulation used empirical fitting functions that were derived from measurements to estimate the transmission efficiencies of the simulated recoils [126]. The functions were based on a set of extensive measurements of the transmission efficiency through EMMA, conducted with an alpha source placed in the target chamber. During these measurements, the central energy to charge ratio to which EMMA was tuned was systematically varied and a set of six angular apertures were installed at the entrance of EMMA so as to study the transmission efficiency of ions through EMMA as a function of energy per unit charge and the horizontal and vertical angles of their trajectories relative to the optic axis. The result was an empirical parameterisation, dependent on θ and ϕ for each of 9 relative energy/charge deviations ranging from -20% to +20% of the central energy/charge setting. The empirical fits at each of these energies are products of asymmetric Gaussian functions. The transmission efficiencies of recoils with energies in between the fitted energies are interpolated using the two nearest energy fits. The estimated transmission

efficiency was 65(9)% for this experiment.

4.2.5 TIGRESS Efficiency

The last remaining efficiency needed before the final cross section could be calculated was the efficiency of gamma ray detections by TIGRESS. The detection efficiency for gamma rays depends on the geometry of the experiment and energy of the photopeak of interest. To calibrate the detector efficiency several radioactive sources of known activities were placed sequentially into the target chamber, the array was then closed to mimic the set up used in the experiment and data were collected for a known period of time. Once complete, the energy spectra from these calibration runs were analysed and the counts in the photopeaks associated with the gamma rays from the calibration sources were extracted by fitting Gaussian functions to the measured spectra. The total expected counts in each photopeak was calculated using the decay equation and known information about each source: the measured activity, the date it was last measured (so as to calculate the time that has since passed) and the absolute intensity per 100 decays of each observed gamma ray (taken from Ref.[31]). The efficiency with which each gamma ray was measured is the ratio of observed to expected counts. The calculated efficiency was plotted on a graph of efficiency vs energy for each gamma ray and is shown in Fig.4.17. The sources used for this efficiency calibration were ^{60}Co, ^{147}Eu, ^{133}Ba and ^{56}Co.

With the measured efficiencies now plotted, a polynomial function was fitted to these data in order to interpolate the efficiency trend. The polynomial function used was

$$\epsilon = \exp\left[\sum_{i=0}^{6} a_i ln(E)^i\right] \tag{4.10}$$

Where, ϵ is the efficiency, E is the energy of the photopeak, a is a calibration constant and i is the order of the polynomial (integer values). The resulting efficiency for a photopeak energy of 1032 keV was 7.9(14)% and 6.5(12)% for a photopeak energy of 1473 keV. The uncertainties on these values arise from the uncertainty in the efficiency curves fit.

4.2.6 Partial Cross Sections Predictions

A partial cross section is associated with only those reactions producing a recoiling nucleus in one specific energy level. In this experiment gamma rays were used to tag the de-excitations of the first and second excited states. These states both have branching ratios of 100% to the ground state through a single gamma ray (1032 keV and 1473 keV, respectively). It is important to note that these states are both directly populated in reactions and fed from above as recoils

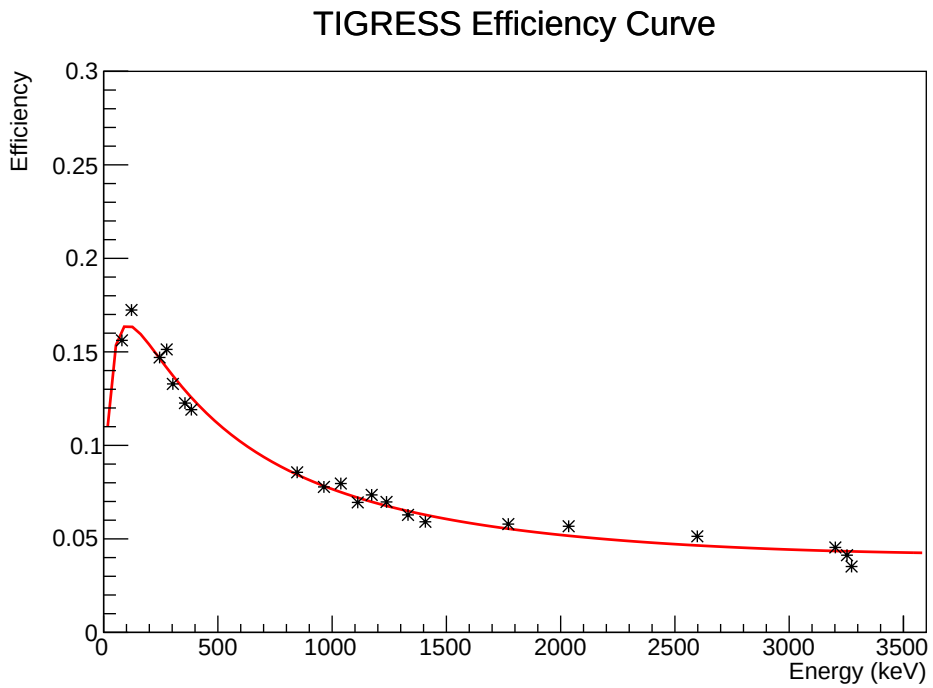

Figure 4.17: Measured photopeak efficiency versus energy for each gamma ray investigated for efficiency calibration in this experiment. The red line is a polynomial that was fitted to these data with a Chi-Squared value of $\chi^2 = 0.005$. The error bars on the data of this plot are negligible.

produced in higher lying states de-excite to the ground state. This indirect feeding from higher energy levels must be included when making partial cross sections predictions. Figures 4.19 and 4.20 show those levels that are known to feed into the first and second excited states, respectively, from above.

Making comparisons between measured partial cross sections and theoretical predictions required combining Hauser-Feshbach models with information on the energy levels of ^{89}Sr and their decay pathways. The code TALYS [79] predicts cross sections leading to the population of individual excited states in the recoiling nucleus. The uncertainty on the predictions for the cross section of an individual excited state was estimated to be 10% in a similar analysis [119]. Fig.4.18 shows the cross section of the ^{86}Kr(α,n)^{89}Sr reaction leading to the ^{89}Sr recoil being in its first excited state and illustrates that each individual energy level in the recoil accounts for only a small fraction of the total cross section. To calculate partial cross section predictions for these excited states therefore, it was not enough to include only the cross section for the direction population of the targeted energy levels, but it was also necessary to include the contributions from all those higher lying states that fed into it. It was important that this information was as complete as possible since the gamma rays chosen for study (1032 keV and 1473 keV) are emitted by states known to be fed from above. Further complicating the analysis

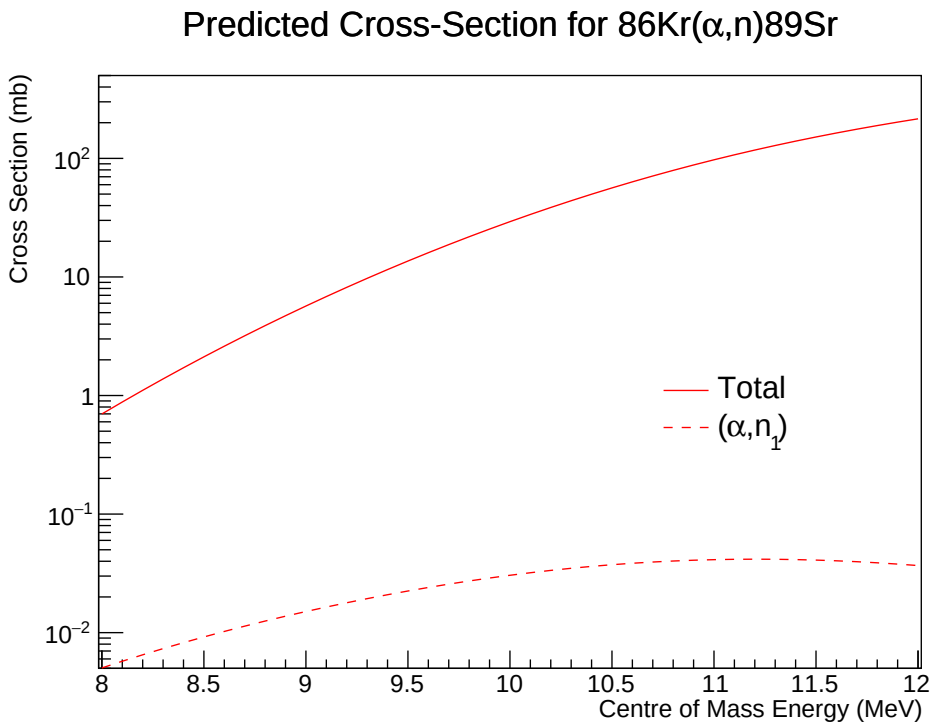

Figure 4.18: Hauser-Feshbach predictions for total cross section and the first excited state contribution of the ^{86}Kr(α,n)^{89}Sr reaction. Calculated using the potential from Ref.[71].

is the fact that energy levels can have multiple decay branches and so not all reactions that produced ^{89}Sr in a higher lying energy level would lead to a 1032 keV or 1473 keV gamma ray. A formal description of the process will now be laid out. Starting from

$$\sigma' = \sum_{i}^{N} p_i \sigma_i \tag{4.11}$$

σ' is the partial cross section for a given energy level calculated using the predicted cross section σ_i for level i and p_i the branching proportion from the populated energy level to the targeted energy level.

The branching proportion p_i is calculated from the gamma ray intensity information in Ref.[31] for each state. p_i is calculated in

$$p_i = \frac{b_z}{\sum_j^J b_j} + \sum_{\ell}^{L} \left[\frac{b_\ell}{\sum_j^J b_j} \prod_{u}^{U} \left(\frac{c_n}{\sum_k^K c_k} \right)_u \right] \tag{4.12}$$

which is written to include not only all the de-excitations that lead immediately to the targeted energy level, but also de-excitations that proceed via other intermediary energy levels. These intermediate energy levels may also have decay branches that also must be included.

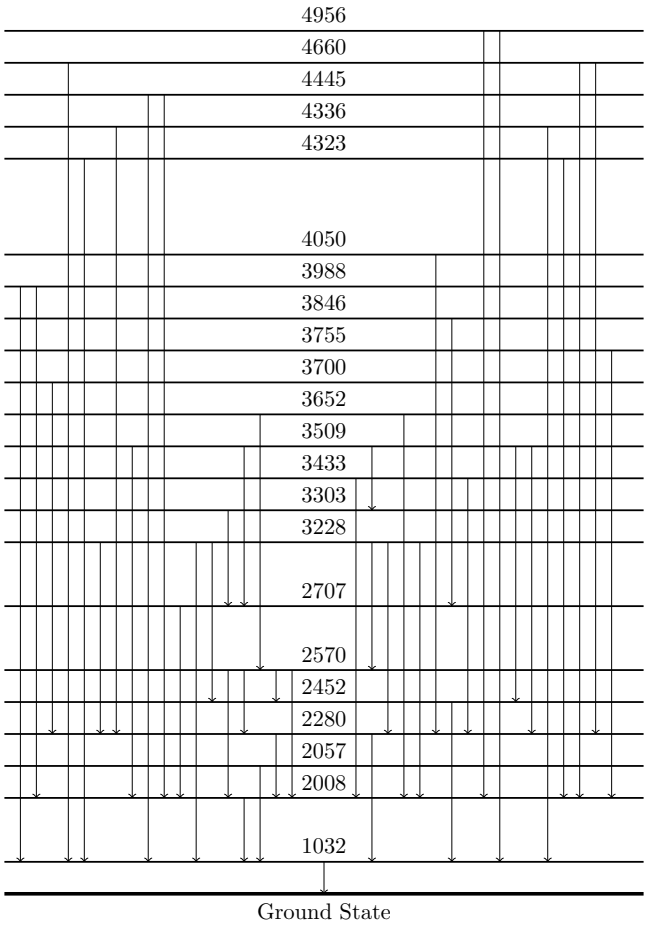

Figure 4.19: Shows a level diagram for ^{89}Sr with the known transitions leading to the population of the first excited state at 1032 keV.

In 4.12, $\frac{b_z}{\sum_j^J b_j}$ is the branching ratio leading straight to the targeted state, with b_z being the intensity of the gamma ray leading to the targeted state and $\sum_j^J b_j$ being the sum of the intensities for all known gamma rays associated with the de-excitation of that energy level, the number of which is J. The next term begins with a sum over all other decays from the populated state that feed into the target state via intermediate states (the number of these decays is given by $L = J - 1$ if there was a z branch directly populating the targeted state). b_l is the intensity of the gamma ray leading to the targeted state. As each intermediate state has its own set of branches, its branching ratio must also be included and is represented by $\frac{c_n}{\sum_k^K c_k}$ where c_n is the intensity of the branch leading towards the targeted state and $\sum_k^K c_k$ is a sum of the intensities of each branch from that state; K is the number of branches available to each intermediate state. Extending this to the case where there are multiple intermediate levels in between the populated state and the targeted energy level (the total number being U) gives Eq.4.12, which includes a product over U terms to account for the branching ratios of all

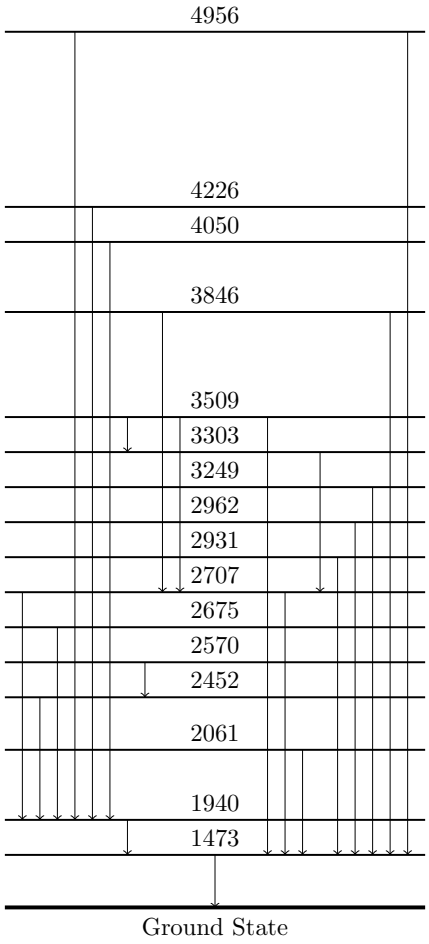

Figure 4.20: Shows a level diagram for ^{89}Sr with the known transitions leading to the population of the second excited state at 1473 keV.

intermediary energy levels.

If the decay scheme of ^{89}Sr were sufficiently well known, the partial cross sections could also be scaled to the total cross section by taking the ratio between the Hauser-Feshbach predictions for the partial cross sections and the predictions for the total cross section. Table 4.3 lists the energy levels that feed into the first and second excited states of ^{89}Sr and includes the proportion of the de-excitations for each energy level that produce a 1032 keV or a 1473 keV gamma ray.

Scaling to the Total Cross Section

Once the partial cross sections had been calculated, it was possible to use them to try to estimate the total cross section. Estimates were made by taking a weighted average of the counts for each gamma ray and, after multiplying by the corresponding TIGRESS efficiency for each gamma ray, that value was used with Eq.2.1 to calculate a combined partial cross section for both the 1032 keV and 1473 keV states. This cross section was then divided by a scaling factor, calculated by summing the predictions made for the two partial cross sections

Table 4.3: The list of energy levels whose de-excitations feed the population of the first and second excited states in ^{89}Sr as defined in Eq.4.12. Branching information from Ref.[31].

Excitation Energy (keV)	Proportion feeding 1032 keV	Proportion feeding 1473 keV
1032	1.000(0)	
1473		1.000(0)
1940		0.174(43)
2008	0.023(5)	
2057	0.495(219)	
2062		0.087(1)
2280	0.965(49)	
2452	0.422(57)	0.056(15)
2570	0.239(18)	0.000(0)
2675		0.148(33)
2707	0.000(0)	0.027(10)
2931		1.000(36)
2962		1.000(0)
3228	0.749(40)	
3249		0.248(104)
3303	0.000(0)	0.0219(11)
3433	0.308(93)	
3509	0.084(12)	0.033(17)
3652	0.075(22)	
3700	0.846(230)	
3755	0.009(4)	
3846	0.222(119)	0.228(119)
3988	0.137(69)	
4050	0.568(207)	0.052(25)
4226		0.087(29)
4329	0.230(35)	
4336	0.067(50)	
4445	0.555(125)	
4660	0.729(77)	
4956	0.030(5)	0.009(29)

and dividing by the predicted the total cross section (for each individual αOMP). The result was an estimate for the total cross section. Despite disagreeing on the absolute value for the cross section, the αOMPs are in good agreement for the relative contribution to the total cross section from individual excited states, giving confidence in the use of this method.

The total cross section could not simply be estimated by counting recoils that were measured in coincidence with events in TIGRESS since some reactions induce ^{89}Sr de-excitations that cascaded through several energy levels and released multiple gamma rays. If one of those gamma rays was in random coincidence with a beam particle that reached the EMMA focal

plane, it could be counted as a "false positive". Since this uncertainty could not be constrained, simply counting those gamma ray-recoil coincidences could not be used to estimate the total cross section. There was also concern that the Compton suppression offered by TIGRESS was not complete, in which some coincidence events above the random background in Fig.4.6 may not in fact be associated with gamma rays emitted by ^{89}Sr. Because of these reasons, it was necessary to follow the procedure described above.

4.3 Results and Discussion

The primary results of the ^{86}Kr(α,n)^{89}Sr experiment are the partial cross sections for the energy levels 1032 keV and 1473 keV. These partial cross sections are $\sigma_{1032} = 1.0^{+0.6}_{-0.8}$ mb and $\sigma_{1473} = 0.8^{+0.7}_{-0.8}$ mb and include both direct population of the first and second energy levels, respectively, plus feeding from higher energy levels. The values were calculated from parameters either directly measured in the experiment or known prior to it (both cases are listed in Table 4.4 with their associated uncertainties). The uncertainty in the partial cross sections originates chiefly from the statistical uncertainty in the measured counts of the two photopeaks. This uncertainty could have been reduced by using a higher beam current and/or by measuring for longer. This is particularly relevant for the 1473 keV partial cross section, which is consistent with zero. The beam current averaged 15.8(16) pA, a relatively conservative value chosen so as not to damage the targets since it was not known how high a beam current they could safely take, this being the first use of these targets in this sort of experiment. The performance of the targets will be discussed after the results from the experiment have been presented.

The partial cross section results are plotted in Fig.4.21 and Fig.4.22 against several predictions from different αOMPs, with all other parameters (level density and gamma-strength function) held constant. Of those αOMPs available for use in TALYS, only some were appropriate to use in this case. The Koning–Delaroche potential [72] (the TALYS default) was not developed to model complex incident particles such as alphas [127] and the Nolte potential [76] is less reliable for incident alphas below 80 MeV (the equivalent incident alpha energy here is 10.5 MeV); therefore neither model was considered. The dispersive model from the potentials of Ref.[73] was also used (labelled DGG02). This potential combines parts of the other two potentials presented in that paper using the dispersion relation and it was used for comparison here because it has previously reproduced experimental data for α-captures below 12 MeV on $A < 100$ nuclei [73]. The McFadden and Satchler model [71] (labelled McF66) was compared since it is commonly used and has been shown to be a good model for elements Ca-Zr with incident alpha energies around 25 MeV. The two Avrigeanu potentials, [74, 75], were also

Table 4.4: The inputs used to calculate the cross section of ^{86}Kr(α,n)^{89}Sr and their associated uncertainties.

Description	Value	Units	Uncertainty (%)
PGAC efficiency	0.94	dimensionless	~ 0
CSF efficiency	0.151	dimensionless	$^{+22.7}_{-58.2}$
Transmission efficiency	0.65	dimensionless	14
ToF Peak fit	0.95	dimensionless	~ 0
Livetime efficiency	0.863	dimensionless	3.1
Beam intensity	4.9×10^6	s^{-1}	10
Target density	3.3×10^{18}	cm^{-2}	5
Duration	161390	s	~ 0
Counts (1032)	15	dimensionless	40
TIGRESS efficiency (1032)	0.075	dimensionless	18
Counts (1473)	10	dimensionless	61
TIGRESS efficiency (1473)	0.061	dimensionless	18

tested. The optical model potential reported in Ref.[75] (labelled Av94) is an extension of the Nolte potential [76] to lower energies, the potential in described in Ref.[74] is a separate model (labelled Av14), good for elements satisfying $45 < A < 209$ at energies below Coulomb barrier.

All αOMPs trialled against these results were found to be in agreement with both partial cross sections at the 1σ level. The large uncertainties on the partial cross sections prevents the cross section uncertainty being constrained further than the uncertainty associated with Hauser-Feshbach predictions. The method for predicting partial cross sections relies on the decay scheme of the recoil nucleus being well known which for ^{89}Sr is not the case. The predictions included cross section contributions from only twenty-two excited states for the 1032 keV partial cross section and sixteen for the 1473 keV partial cross section. The contribution to the predicted partial cross sections from direct population of the first and second energy levels is 10% and 17%, respectively, showing that the contribution from higher energy levels is already significant. If, as is likely, there are other energy levels that feed into either the first or second excited state then the predicted partial cross sections will be underestimates. Indeed, a comparison of the two predicted partial cross sections shows that the 1032 keV gamma ray is predicted to be stronger than that of 1473 keV at energies above 10 MeV. Results from a previous experiment do not support this prediction [118] and suggest that there are indeed

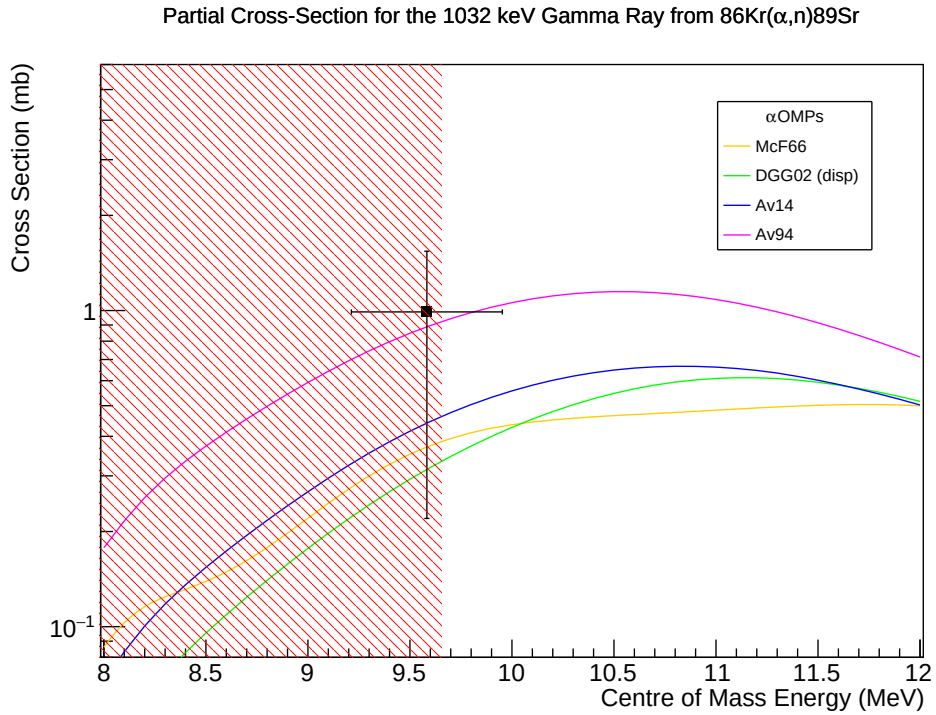

Figure 4.21: The partial cross section for ^{86}Kr(α,n)^{89}Sr yielding a 1032 keV gamma ray. The coloured lines are partial Hauser-Feshbach predictions calculated with different αOMPs and decay information from Ref.[31] and the shaded area indicates the astrophysical region of interest for the weak r-process.

unknown decay pathways leading to at least the 1473 keV excited state. This suggests that a study of the coincident gamma rays from the ^{86}Kr(α,n)^{89}Sr reaction is necessary to better quantify the decay scheme of ^{89}Sr so that more robust predictions for the partial cross sections can be made. Identifying the need for a better understanding of the ^{89}Sr gamma decay scheme is an important conclusion for future measurements using this method whose results will also be compared to theoretical cross sections. The lack of information on the higher excited states may also be the source of the unknown gamma ray observed at 995 keV, shown in Fig.4.10. Since this gamma ray was observed in coincidence with mass 89 recoils it is likely that is is associated with ^{89}Sr. Considering the coincidence time gating and Doppler shift correction, it is unlikely that this is a simply a prominent background peak, especially since Fig.4.8 suggests that the background has been well controlled.

Fig.4.23 shows an attempt to scale the partial cross sections to a total cross section. Because it is unknown how many other higher lying states may feed into the 1032 keV and 1473 keV levels, the resulting estimate for the total cross section is an upper limit. That limit was estimated to be $\sigma_{\text{total}} < 71.8$ mb and was not able to exclude any of the αOMPs, including the new Atomki V2 potential [57] (labelled Moh21 on Fig.4.23) since the scaling method assumes

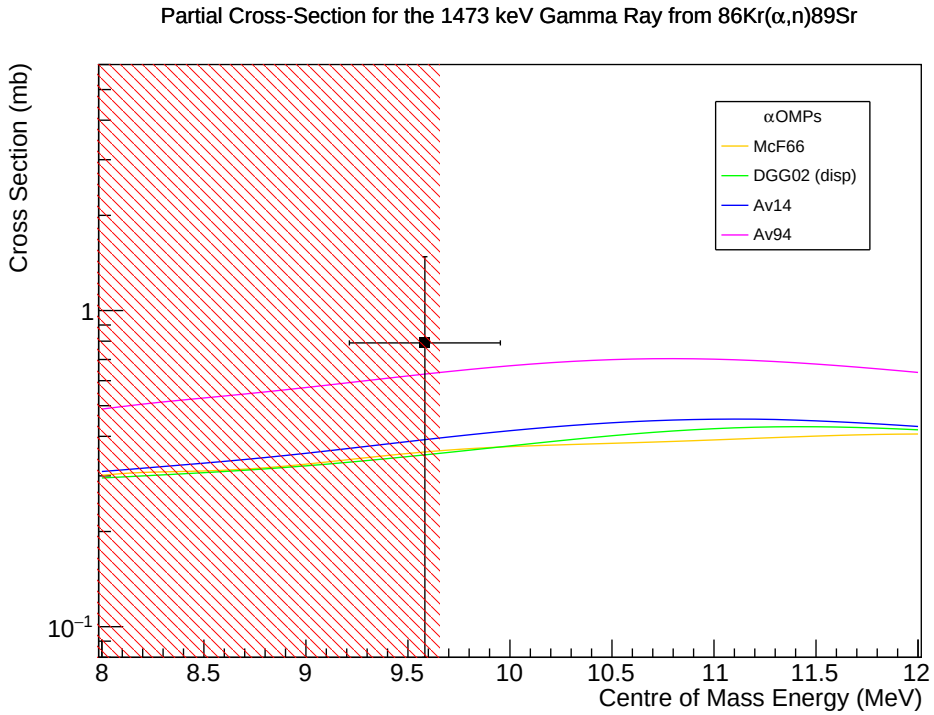

Figure 4.22: The partial cross section for ^{86}Kr(α,n)^{89}Sr yielding a 1473 keV gamma ray. The coloured lines are partial Hauser-Feshbach predictions calculated with different αOMPs and decay information from Ref.[31] and the shaded area indicates the astrophysical region of interest for the weak r-process.

a well known decay structure for the recoiling ^{89}Sr nucleus. The upper limit does not exclude the possibility that the total cross section for the ^{86}Kr(α,n)^{89}Sr reaction may be larger than has previously been used in models such as those used by Ref.[50] and Ref.[51]. Those abundance ratios that would be most affected by this change would be: Sr/Zr, Y/Zr and Mo/Zr, as discussed in Chapter 1.4.3, which would be increased relative to current models. The final abundance of elements 38–42, 44, 45 and 47 would also be expected to be greater than the currently assumed, based on the correlation coefficients reported in Ref.[51] and listed in Table 1.1.

Since the results for total cross section is a limit, the uncertainty is not reduced by this result. Future measurements of ^{86}Kr(α,n)^{89}Sr are planned and will take place at higher energies, enabling the shape of the new Atomki V2 potential (shown in Fig.4.23) to be trialled against measured data. That investigation would again be more reliable with a better quantification of the ^{89}Sr gamma decay scheme. Investigating gamma-gamma coincidences in the higher energy version of this experiment could improve the understanding of the ^{89}Sr decay scheme.

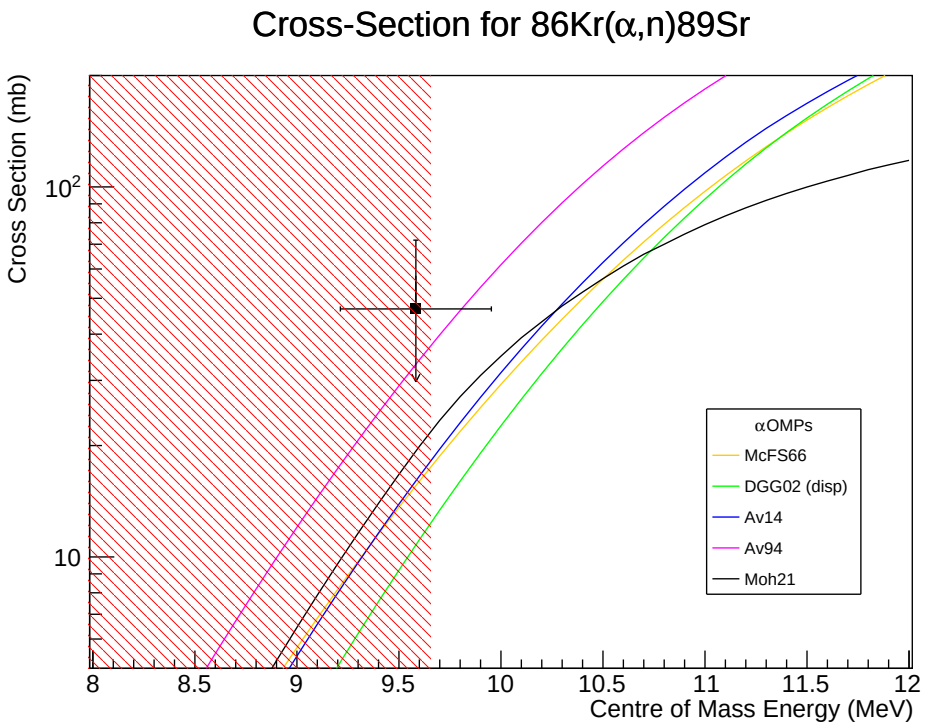

Figure 4.23: Total ^{86}Kr(α,n)^{89}Sr cross section estimated by scaling from the combined partial cross sections. The shaded area indicates the astrophysical region of interest for the weak r-process. Credit: Dr A. Psaltis for the Atomki-V2 data [57].

Magnetron-sputtered Targets

Since this was the first use of the He:Si targets the beam current was kept low at 15.8(16) pA. The targets used held up throughout the experiment and there was little evidence of degradation or depletion, based on Fig.4.24, which shows the He:Si scattering ratio run by run for both SSBs. The scatter in the data on Fig.4.24 comes from the low helium counts recorded for each run relative to the silicon counts. This indicates that it is possible to move to higher beam currents in future experiments; something which is desirable given the low statistics in the gamma-ray energy spectrum. One concern about the targets used was their brittleness. This brittleness did not impact the success of this experiment. However, there was some damage sustained to one of the three targets sent to TRIUMF during transport. The damage consisted of a planar shearing of the central section of the target, which meant that the areal density was no longer well known and so that target could not be used. Fortunately, the other two targets were in better condition. These were self-supported He:Si foils and were grown on a layer of NaCl before being floated in water so that the NaCl dissolved away. Interestingly, some evidence of this procedure may be observed on the SSB scattering spectra in Fig.4.13. The slightly raised section of the spectrum around 150 MeV corresponds to the expected position of

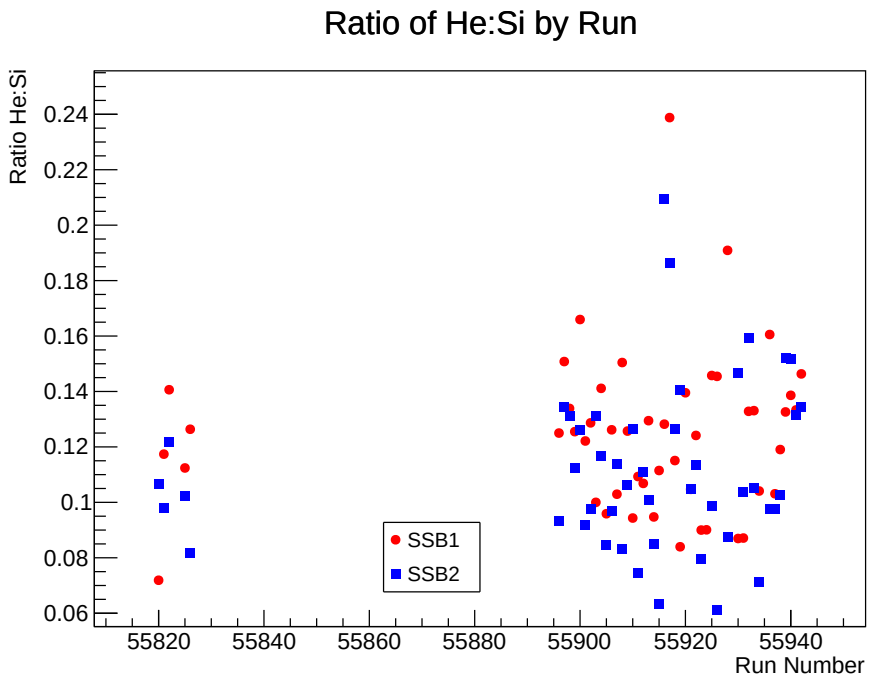

Figure 4.24: The ratio of helium to silicon scattered into the SSBs by run as a measurement of target helium content.

scattered chlorine atoms. Any scattered sodium would be obscured behind the scattered beam. Other examples of these targets sputtered on to other backing materials (rather than being self-supported as was used here) have proved to be more physically robust.

Fig.4.14 shows the beam normalisation based on scattering calculations and it can be seen that there was an interruption to the data taking runs. This was due to problems with the beam. In between the earlier and later data taking runs, the targets were switched. It can be observed that SSB2 has a significantly lower estimated current during these earlier runs which is not replicated later on in the experiment. It is likely that this was a product of the target switch, possibly caused by the target frame partially obscuring SSB2. The targets were delivered on a frame that was unsuitable for use in EMMA and had to be fixed to a second EMMA target frame before they could be placed into the target chamber. The secondary target frames were attached in slightly different orientations for each target possibly leading one to fall partly into the beam spot which would explain the discrepancy in the estimated current. Despite this being the likely case, however, these values were still used in normalising the beam current as it could not be empirically confirmed that the orientation of the target frame was the cause, therefore these runs were included. On the other hand, these early runs represent a small subsection of the total experimental time therefore the difference in the average beam current calculated when excluding these runs was negligible for an average weighted by the

number of scattered silicon events per run.

Chapter 5

Conclusion

This thesis has presented the results from two separate experiments, each investigating a different astrophysical process that may be a source of light heavy elements at early times in the universe additional to the r-process.

The possible contribution to early light heavy element production by the s-process in rapidly-rotating metal-poor stars was investigated in an ^{20}Ne(d,p)^{21}Ne experiment with the HELIOS spectrometer at ANL in the United States. The aim was to make spin-parity assignments for important energy levels in the ^{21}Ne nucleus. These levels, form resonances at the right energies to impact the ^{17}O(α,n)^{20}Ne reaction rate. The ^{17}O(α,n)^{20}Ne/^{17}O(α,γ)^{21}Ne reaction rate ratio determines the efficiency of neutron poisoning by ^{16}O in rotating massive stars and, according to computer simulations, governs whether or not the s-process contributes significantly to the abundance of lighter heavy elements at early times. The experiment was conducted in inverse kinematics since previous studies had suffered from target contamination which obscured the energy region of interest. Unfortunately, this resulted in poor resolution making it challenging to resolve levels close in energy. Nevertheless, attempts were made to extract spin-parities for those energy levels observed using ADWA analysis. Analysis of the stronger populated peaks in the spectrum generally produced good agreement with literature, lending credibility to the results for previously unanalysed states.

Through comparisons with previous experiments, predictions were made for the neutron widths of two states that are key for ^{17}O+α reactions in rotating massive stars. The 7820 keV state was best described with a spin parity of $\frac{3}{2}^-$ with a neutron width of 7600(2100) eV. The calculated resonance strength using literature estimates for alpha width is $\omega\gamma_n = 0.12\mu$eV, which is in agreement with literature. A disagreement between two (d,p) studies and a neutron resonance experiment could warrant a future investigation into the neutron resonances of ^{21}Ne.

An upper limit on the neutron width for the 7749 keV energy level was calculated to be

$\Gamma_n < 7200\,\text{eV}$, assuming $\ell = 1$ on the basis that it has previously been observed as a narrow peak which excludes an $\ell = 0$ transfer. Assigning a minimum $\ell = 1$ transfer in a (d,p) reaction suggests a resonance strength of $\omega\gamma_n < 7.2 \times 10^{-3}\mu\text{eV}$ which is a factor of three below what has previously been assumed in reaction rate models. A lower resonance strength implies a reduced rate of $^{17}\text{O}(\alpha,\text{n})^{20}\text{Ne}$ reactions making s-process nucleosynthesis in rotating massive stars less favourable. To determine the overall effect on s-process nucleosynthesis in rotating metal poor stars, a model simulation incorporating these results would need to be run. Combining these results with anticipated future results from studies aiming to measure Γ_α and Γ_γ for states in ^{21}Ne would produce the most up-to-date predictions for s-process nucleosynthesis in rotating massive stars.

Secondly, the experiment conducted with EMMA at TRIUMF aimed to study $^{86}\text{Kr}(\alpha,\text{n})^{89}\text{Sr}$; a reaction which, according to models, is important to the weak r-process in core-collapse supernovae. It has been found that in the weak r-process (α,n) reactions are the primary drivers of nucleosynthesis, however, cross section predictions for (α,n) reactions are a major source of uncertainty in nucleosynthesis predictions for this site and reducing these uncertainties will help determine if this process can contribute significantly to the abundances of lighter heavy elements at early times in the universe. Analysis of the experiment yielded partial cross sections for two gamma rays associated with the recoiling ^{89}Sr nucleus. The results are $1.0^{+0.6}_{-0.8}\,\text{mb}$ for the 1032 keV gamma ray and $0.8^{+0.7}_{-0.8}\,\text{mb}$ for the 1473 keV gamma ray; both agreeing with model predictions. Unfortunately, the decay scheme for ^{89}Sr is not well enough known to allow a meaningful estimate for the total cross section. A second measurement of this reaction (at a higher centre-of-mass energy) has already taken place with a third measurement planned for the summer of 2023. The results presented here are for the lowest energy that is planned for study and could be used to calculate a total cross section with sufficient knowledge of the gamma decay scheme for ^{89}Sr. It is recommended here that, if possible, gamma-gamma coincidences for ^{89}Sr should be investigated during analysis of the other measurements to attempt to identify which energy levels are contributing significantly to the partial cross sections of the reaction.

In summary, the light element primary process is a hypothetical mode of nucleosynthesis that is needed to explain an observed over abundance of the lighter heavy elements with respect to model predictions at early times in the universe. Two candidate processes have been analysed in the project: the weak r-process in core-collapse supernovae and the s-process in rotating massive stars. This project has contributed measurements that when applied to astrophysical models will help reduce uncertainties in the nucleosynthesis predictions for both sites.

Appendix A

Charge State Fraction Efficiency

$$y = He^{\frac{-(x-\mu)^2}{2\sigma^2}} \tag{A.1}$$

Theoretical modelling of the charge state distribution (CSD) as a Gaussian curve (Eq.A.1) yields values for peak centroid (μ_t) and width (σ_t). Both parameters have an associated theoretical uncertainty. The experimentally measured CSD also has values for centroid (μ_e) and width (σ_e); each has an experimental uncertainty. The area beneath the curve is normalised to unity and the equation

$$\text{Area} = 1 = \sigma H\sqrt{2\pi} \tag{A.2}$$

is used to calculated H, the height of the CSD peak.

The ratio of measured parameters to predicted parameters is found and used to scale the predicted values to the measured values allowing the combination of theoretical and experimental uncertainties. The equation

$$S_\mu = \frac{\mu_e}{\mu_t} \tag{A.3}$$

for example, shows the scaling factor (S_μ) for the centroid. Once the uncertainties have been propagated using

$$\Delta S = S\sqrt{\left(\frac{\Delta A}{A}\right)^2 + \left(\frac{\Delta B}{B}\right)^2} \tag{A.4}$$

the CSD can be used to determine the fraction of the beam represented by each different charge state and to calculate the associated uncertainty on that fraction. Eq.A.4 is a general equation, shown for the case of $S = \frac{A}{B}$, where A and B are uncorrelated; S is used to represent either the scaling factor calculated for either μ or σ, as equation Eq.A.4 is used in both cases.

To determined the fraction of the beam each charge state represents, the charge state used in the experiment is first identified, then the height of the Gaussian curve is calculated at that

charge state using Eq.A.1; this value is the Charge State Fraction (CSF). To calculate the lower limit of the CSF, the CSD centroid is moved as far from the chosen charge state as the one sigma uncertainty on μ allows (i.e. if the charge state is lower than the centroid, $\mu' = \mu + \Delta\mu$) and the width is made as narrow as the one sigma uncertainty limit on σ allows (i.e. $\sigma' = \sigma - \Delta\sigma$). Eq.A.1 is now solved again at the chosen charge state with these values for centroid and width (μ' and σ') and the result is the lower limit for the CSF.

The upper limit on the CSF is calculated by moving the centroid as close to the chosen charge state as the one sigma limit on μ allows and again setting the width to the minimum within the one sigma limit of σ, then solving Eq.A.1 at the chosen charge state. Credit to Dr. M. Williams for this method [128].

Appendix B

^{20}Ne(d,p)^{21}Ne Results Data Tables

2749 keV		4526 keV	
Angle (Degrees)	Normalised Yield (Counts)	Angle (Degrees)	Normalised Yield (Counts)
29.8 ± 1.3	821 ± 16	25.3 ± 1.0	694 ± 17
32.7 ± 1.2	1189 ± 24	28.8 ± 1.1	511 ± 15
35.6 ± 1.1	604 ± 18	32.1 ± 1.2	230 ± 12
38.3 ± 1.1	138 ± 8	35.2 ± 1.3	218 ± 8
40.9 ± 1.0	78 ± 7	38.1 ± 1.4	90 ± 7
43.3 ± 1.0	35 ± 5	40.7 ± 1.6	98 ± 7

4725 keV		5334 keV	
Angle (Degrees)	Normalised Yield (Counts)	Angle (Degrees)	Normalised Yield (Counts)
24.7 ± 1.7	1686 ± 25	22.6 ± 1.9	1706 ± 26
28.2 ± 1.5	1280 ± 22	26.5 ± 1.6	1387 ± 22
31.7 ± 1.3	699 ± 19	30.2 ± 1.4	657 ± 18
34.8 ± 1.2	776 ± 16	33.5 ± 1.3	603 ± 14
37.7 ± 1.1	337 ± 12	36.6 ± 1.2	266 ± 11
40.4 ± 1.1	316 ± 13	39.3 ± 1.1	201 ± 8

5549 keV		5822 keV	
Angle (Degrees)	Normalised Yield (Counts)	Angle (Degrees)	Normalised Yield (Counts)
21.8 ± 1.9	736 ± 17	20.8 ± 2.1	553 ± 14
25.9 ± 1.6	511 ± 14	25.0 ± 1.7	484 ± 15
29.7 ± 1.4	264 ± 12	28.9 ± 1.5	247 ± 13
33.0 ± 1.3	217 ± 9	32.4 ± 1.3	238 ± 11
36.1 ± 1.2	228 ± 13	35.6 ± 1.2	114 ± 16
39.0 ± 1.1	103 ± 10	38.5 ± 1.1	98 ± 14

6609 keV		7106 keV	
Angle (Degrees)	Normalised Yield (Counts)	Angle (Degrees)	Normalised Yield (Counts)
17.0 ± 2.6	1113 ± 21		
22.2 ± 2.0	800 ± 17	20.1 ± 1.3	156 ± 22
26.6 ± 1.6	542 ± 19	25.0 ± 1.5	88 ± 40
30.4 ± 1.4	277 ± 11	29.0 ± 1.8	37 ± 7
33.8 ± 1.3	129 ± 10	32.6 ± 2.2	42 ± 9
36.9 ± 1.2	150 ± 11	35.8 ± 1.3	58 ± 9

7176 keV		7337 keV	
Angle (Degrees)	Normalised Yield (Counts)	Angle (Degrees)	Normalised Yield (Counts)
19.8 ± 2.3	409 ± 26	19.0 ± 2.4	365 ± 25
24.7 ± 1.8	221 ± 40	22.3 ± 1.8	208 ± 16
28.8 ± 1.5	170 ± 16	28.4 ± 1.6	160 ± 15
32.5 ± 1.4	123 ± 14	32.0 ± 1.4	115 ± 15
35.7 ± 1.3	71 ± 10	35.3 ± 1.3	102 ± 11

7420 keV		7559 keV	
Angle (Degrees)	Normalised Yield (Counts)	Angle (Degrees)	Normalised Yield (Counts)
18.6 ± 2.4	162 ± 20	17.8 ± 2.6	54 ± 12
23.9 ± 1.9	82 ± 13	23.3 ± 1.9	36 ± 9
28.1 ± 1.6	107 ± 15	27.7 ± 1.6	25 ± 11
31.8 ± 1.4	47 ± 12	31.5 ± 1.4	29 ± 11
35.1 ± 1.3	54 ± 10	34.8 ± 1.3	38 ± 12

7619 keV		7749 keV	
Angle (Degrees)	Normalised Yield (Counts)	Angle (Degrees)	Normalised Yield (Counts)
17.5 ± 2.6	72 ± 12	16.7 ± 2.8	14 ± 10
23.0 ± 1.9	47 ± 9	22.6 ± 2.0	25 ± 6
27.5 ± 1.6	50 ± 11	27.1 ± 1.7	24 ± 10
31.3 ± 1.4	33 ± 11	30.9 ± 1.5	22 ± 8
34.7 ± 1.3	34 ± 12	34.4 ± 1.3	30 ± 17

7820 keV		7982 keV	
Angle (Degrees)	Normalised Yield (Counts)	Angle (Degrees)	Normalised Yield (Counts)
16.3 ± 2.9	49 ± 10	15.2 ± 3.1	25 ± 9
22.3 ± 2.0	47 ± 8	21.6 ± 2.1	27 ± 10
26.8 ± 1.7	23 ± 10	26.3 ± 1.7	34 ± 6
30.7 ± 1.5	31 ± 7	30.3 ± 3.0	44 ± 9
34.2 ± 1.3	46 ± 15	33.8 ± 1.4	48 ± 8

Bibliography

[1] W. D. Arnett. "Type I supernovae. I - Analytic solutions for the early part of the light curve". *The Astrophysical Journal* 253 (1982), pp. 785–797.

[2] A. M. Laird et al. "Progress on nuclear reaction rates affecting the stellar production of 26Al". *Journal of Physics G: Nuclear and Particle Physics* 50 (2023), p. 033002.

[3] R. H. Cyburt et al. "Big bang nucleosynthesis: Present status". *Reviews of Modern Physics* 88 (2016), p. 015004.

[4] E. Margaret Burbidge et al. "Synthesis of the Elements in Stars". *Reviews of Modern Physics* 29 (1957), pp. 547–650.

[5] C. Fox et al. "Explosive Hydrogen Burning of ^{17}O in Classical Novae". *Physical Review Letters* 93 (2004), p. 081102.

[6] M. Salaris and S. Cassisi. *Evolution of Stars and Stellar Populations*. John Wiley and Sons, 2005.

[7] J. Audouze and G. Israel. *The Cambridge Atlas of Astronomy (2 ed.)* Cambridge University Press, 1988.

[8] W. J. Huang et al. "The AME 2020 atomic mass evaluation (I). Evaluation of input data, and adjustment procedures". *Chinese Physics C* 45 (2021), p. 030002.

[9] M. Wang et al. "The AME 2020 atomic mass evaluation (II). Tables, graphs and references". *Chinese Physics C* 45 (2021), p. 030003.

[10] S Höfner and H. Olofsson. "Mass loss of stars on the asymptotic giant branch". *The Astronomy and Astrophysics Review* 26 (2018).

[11] J. Bliss et al. "Impact of (α, n) reactions on weak r-process in neutrino-driven winds". *Journal of Physics G: Nuclear and Particle Physics* 44 (2017), p. 054003.

[12] B. S. Meyer. "The r-, s-, and p-Processes in Nucleosynthesis". *Annual Review of Astronomy and Astrophysics* 32 (1994), pp. 153–190.

[13] F. Käppeler et al. "The *s* process: Nuclear physics, stellar models, and observations". *Reviews of Modern Physics* 83 (2011), pp. 157–193.

[14] D. M. Siegel, J. Barnes, and B.D. Metzger. "Collapsars as a major source of r-process elements". *Nature* 569 (2019), pp. 241–244.

[15] D. Watson et al. "Identification of strontium in the merger of two neutron stars". *Nature* 574 (2019), pp. 497–500.

[16] M. L. Pumo. "The s-process nucleosynthesis in massive stars: current status and uncertainties due to convective overshooting". *Astrophysics*. IntechOpen, 2012.

[17] A. P. Ji et al. "Complete element abundances of nine star in the r-process galaxy reticulum II". *The Astrophysical Journal* 830 (2016), p. 93.

[18] S. Wanajo et al. "Production of all the r-process nuclides in the dynamical ejecta of neutron star mergers". *The Astrophysical Journal* 789 (2014), p. L39.

[19] A. Arcones, H.-T. Janka, and L. Scheck. "Nucleosynthesis-relevant conditions in neutrino-driven supernova outflows I. Spherically symmetric hydrodynamic simulations". *Astronomy and Astrophysics* 467 (2007), pp. 1227–1248.

[20] C. Travaglio et al. "Galactic evolution of Sr, Y and Zr: a multiplicity of nucleosynthetic processes". *The Astrophysical Journal* 601 (2004), pp. 864–884.

[21] M. Spite and F. Spite. "Nucleosynthesis in the Galaxy and the chemical composition of old halo stars". *Astronomy and Astrophysics* 67 (1978), pp. 23–31.

[22] J. Cowan and F. Thielemann. "R-Process Nucleosynthesis in Supernovae". *Physics Today* 57 (2004), pp. 47–53.

[23] S. E. Woosley, A. Heger, and T. A. Weaver. "The evolution and explosion of massive stars". *Reviews of Modern Physics* 74 (2002), pp. 1015–1071.

[24] K. S. Krane. *Introductory Nuclear Physics*. Hoboken NJ: Wiley, 1987.

[25] G. Meynet, S. Ekström, and A. Maeder. "The early star generations: the dominant effect of rotation on the CNO yields". *Astronomy and Astrophysics* 447 (2006), pp. 623–639.

[26] M. Pignatari et al. "The s-process in massive stars at low metallicity: the effect of primary ^{14}N from fast rotating stars". *The Astrophysical Journal* 687 (2008), pp. 95–98.

[27] M. Rayet and M. Hashimoto. "The s-process efficiency in massive stars. Astronomy and Astrophysics". *Astronomy and Astrophysics* 354 (2000), pp. 740–748.

[28] M. Pignatari et al. "The weak s-process in massive stars and its dependence on the neutron capture cross-sections". *The Astrophysical Journal* 710 (2010), pp. 1557–1577.

[29] M. P. Taggart et al. "A direct measurement of the $^{17}O(\alpha,\gamma)^{21}Ne$ reaction in inverse kinematics and its impact on heavy element production". *Physics Letters B* 798 (2019), p. 134894.

[30] J. Frost-Schenk et al. "The impact of ^{17}O $+\alpha$ reaction rate uncertainties on the s-process in rotating massive stars". *Monthly Notices of the Royal Astronomical Society* 514 (2022), pp. 2650–2657.

[31] National Nuclear Data Centre. *ENSDF, NNDC online data service, ENSDF database.* `http://www.nndc.bnl.gov/ensdf/`. 2015.

[32] G. R. Caughlan and W. A. Folwer. "Thermal reaction rates V". *Atomic Data and Nuclear Data Tables* 40 (1988), p. 243.

[33] W. A. Fowler, G. R. Caughlan, and B. A. Zimmerman. "Thermonuclear reaction rates, II". *Annual Review of Astronomy and Astrophysics* 13 (1975), pp. 69–112.

[34] P. Descouvemont. "Microscopic three-cluster study of 21-nucleon systems". *Physical Review C.* 48 (1993), p. 2746.

[35] A. Best et al. "First direct measurement of resonance strengths in ^{17}O$(\alpha,\gamma)^{21}$Ne". *Physical Review C* 83 (2011), p. 052802.

[36] S. Engel et al. "Commissioning the DRAGON facility at ISAC". *Nuclear Instruments and Methods in Physics Research Section A: Accelerators, Spectrometers, Detectors and Associated Equipment* 553 (2005), pp. 491–500.

[37] A. Best et al. "Measurement of the reaction $^{17}O(\alpha,n)^{20}Ne$ and its impact on the s process in massive stars". *Physical Review C.* 87 (2013), p. 045805.

[38] P. D. Kunz. "Distorted Wave Code DWUCK4 (unpublished)" (1978).

[39] R. Longland et al. "Charged-particle thermonuclear reaction rates: I. Monte Carlo method and statistical distributions". *Nuclear Physics A* 841 (2010). The 2010 Evaluation of Monte Carlo based Thermonuclear Reaction Rates, pp. 1–30.

[40] A.L. Sallaska et al. "STARLIB: A NEXT-GENERATION REACTION-RATE LIBRARY FOR NUCLEAR ASTROPHYSICS". *The Astrophysical Journal Supplement Series* 207 (2013), p. 18.

[41] M. Molero et al. "Origin of neutron-capture elements with the Gaia-ESO survey: the evolution of s- and r-process elements across the Milky Way". *Monthly Notices of the Royal Astronomical Society* 523 (2023), pp. 2974–2989.

[42] C. Winteler et al. "Magnetorotationally Driven Supernovae as the Origin of Early Galaxy r-process Elements?" *The Astrophysical Journal Letters* 750 (2012), p. L22.

[43] S. E. Woosley et al. "The r-Process and Neutrino-heated Supernova Ejecta". *The Astrophysical Journal* 433 (1994), p. 229.

[44] A. Arcones and F.-K. Thielemann. "Neutrino-driven wind simulations and nucleosynthesis of heavy elements". *Journal of Physics G: Nuclear and Particle Physics* 40 (2013), p. 013201.

[45] H.-Th. Janka et al. "Theory of core-collapse supernovae". *Physics Reports* 442 (2007), pp. 38–74.

[46] Rutgers, The State University of New Jersey, Department of Physics & Astronomy. 2014. URL: `https://www.physics.rutgers.edu/analyze/wiki/onion.png`.

[47] D. Watson et al. "Identification of strontium in the merger of two neutron stars". *Nature* 574 (2019), pp. 497–500.

[48] Y.-Z. Qian and G.J. Wasserburg. "Where, oh where has the r-process gone?" *Physics Reports* 442 (2007), pp. 237–268.

[49] S. Wanajo et al. "Nucleosynthesis in the Innermost Ejecta of Neutrino-driven Supernova Explosions in Two Dimensions". *The Astrophysical Journal* 852 (2018), p. 40.

[50] A. Psaltis et al. "Constraining Nucleosynthesis in Neutrino-driven Winds: Observations, Simulations, and Nuclear Physics". *The Astrophysical Journal* 935 (2022), p. 27. URL: `https://dx.doi.org/10.3847/1538-4357/ac7da7`.

[51] J. Bliss et al. "Nuclear physics uncertainties in neutrino-driven, neutron-rich supernova ejecta". *Physical Review C* 101 (2020), p. 055807.

[52] G. G. Kiss et al. "Low-energy Measurement of the 96Zr(α,n)99Mo Reaction Cross Section and Its Impact on Weak r-process Nucleosynthesis". *The Astrophysical Journal* 908 (2021), p. 202.

[53] T. N. Szegedi et al. "Activation thick target yield measurement of ^{100}Mo$(\alpha, n)^{103}$Ru for studying the weak r-process nucleosynthesis". *Physical Review C* 104 (2021), p. 035804.

[54] Gy. Gyürky et al. "The activation method for cross section measurements in nuclear astrophysics". *European Physical Journal A* 55 (2019), p. 41.

[55] W.-J. Ong et al. "Measurement of the ^{100}Mo(α, xn) cross section at weak r-process energies". *Physical Review C* 105 (2022), p. 055803.

[56] P. F. F. Carnelli et al. "Multi-Sampling Ionization Chamber (MUSIC) for measurements of fusion reactions with radioactive beams". *Nuclear Instruments and Methods in Physics Research Section A: Accelerators, Spectrometers, Detectors and Associated Equipment* 799 (2015), pp. 197–202.

[57] P. Mohr et al. "Astrophysical reaction rates of α-induced reactions for nuclei with 26 $\leq$Z$\leq$ 83 from the new Atomki-V2 α-nucleus potential". *Atomic Data and Nuclear Data Tables* 142 (2021), p. 101453.

[58] M. Kelabi. "Half-life of Alpha Decay from A Straight-line Potential Barrier" (2015).

[59] S. Courtin et al. *proposal andromede*. 2016.

[60] H. P. Trautvetter and C. Rolfs. "Direct capture in the ^{24}Mg(p,γ)^{25}Al reaction". *Nuclear Physics A* 242 (1975), pp. 519–532.

[61] C. Iliadis. "Proton single-particle reduced widths for unbound states". *Nuclear Physics A* 618 (1997), pp. 166–175.

[62] C. Iliadis. *Nuclear Physics of Stars*. Wiley, 2007.

[63] G Mairle et al. "A Comparative Spectroscopic Investigation of 2 by Pickup Reactions". *Zeitschrift für Physik A* 301 (1981), pp. 157–163.

[64] I. J. Thompson. "Coupled Channels Methods for Nuclear Physics". *Computer Physics Reports* 7 (1988), pp. 167–212.

[65] C. M. Perey and F. G. Perey. "Compilation of phenomenological optical-model parameters 1954–1975". *Atomic Data and Nuclear Data Tables* 17 (1976), pp. 1–101.

[66] P. E. Hodgson. "The nuclear optical model". *Reports on Progress in Physics* 34 (1971), p. 765.

[67] R. L. Varner et al. "A global nucleon optical model potential". *Physics Reports* 201 (1991), pp. 57–119.

[68] S. Giron. "Etude de la réaction d'intérêt astrophysique ^{60}Fe(n,γ)^{61}Fe par réaction de transfert (d,p) gamma". Theses. Université Paris Sud - Paris XI, 2011.

[69] R. C. Johnson and P. J. R. Soper. "Contribution of Deuteron Breakup Channels to Deuteron Stripping and Elastic Scattering". *Physical Review C* 1 (1970), pp. 976–990.

[70] G. L. Wales and R.C. Johnson. "Deuteron break-up effects in (p, d) reactions at 65 MeV". *Nuclear Physics A* 274 (1976), pp. 168–176.

[71] L. McFadden and G. R. Satchler. "Optical-model analysis of the scattering of 24.7 MeV alpha particles". *Nuclear Physiscs* 84 (1966), pp. 177–200.

[72] A. J. Koning and J. P. Delaroche. "Local and global nucleon optical models from 1 keV to 200 MeV". *Nuclear Physics A* 713 (2003), pp. 231–310.

[73] P. Demetriou, C. Grama, and S. Goriely. "Improved global α-optical model potentials at low energies". *Nuclear Physics A* 707 (2002), pp. 253–276.

[74] V. Avrigeanu, M. Avrigeanu, and C. Mănăilescu. "Further explorations of the α-particle optical model potential at low energies for the mass range $A \approx 45$–209". *Physical Review C* 90 (2014), p. 044612.

[75] V. Avrigeanu, P. E. Hodgson, and M. Avrigeanu. "Global optical potentials for emitted alpha particles". *Physical Review C* 49 (1994), pp. 2136–2141.

[76] M. Nolte, H. Machner, and J. Bojowald. "Global optical potential for α particles with energies above 80 MeV". *Physical Review C* 36 (1987), pp. 1312–1316.

[77] W. Hauser and H. Feshbach. "The Inelastic Scattering of Neutrons". *Physical Review* 87 (1952), pp. 366–373.

[78] F. S. Dietrich. "Simple Derivation of the Hauser-Feshbach and Weisskopf-Ewing Formulae, with Application to Surrogate Reactions" (2004). URL: `https://www.osti.gov/biblio/15013687`.

[79] S. Hilaire A. Koning and S. Goriely. *TALYS-1.95 User Manual*. 2019. URL: `https://tendl.web.psi.ch/tendl_2021/talys.html`.

[80] URL: `https://www.phy.anl.gov/atlas/,`.

[81] G. Savard et al. "Radioactive beams from gas catchers: The CARIBU facility". *Nuclear Instruments and Methods in Physics Research Section B: Beam Interactions with Materials and Atoms* 266.19 (2008), pp. 4086–4091.

[82] A. N. Agnihotri et al. "An ECR ion source-based low-energy ion accelerator: development and performance". *Physica Scripta* 2011.T144 (2011), p. 014038. URL: `https://dx.doi.org/10.1088/0031-8949/2011/T144/014038`.

[83] J. C. Lighthall et al. "Commissioning of the HELIOS spectrometer". *Nuclear Instruments and Methods in Physics Research Section A: Accelerators, Spectrometers, Detectors and Associated Equipment* 622 (2010), pp. 97–106.

[84] A. H. Wuosmaa et al. "A solenoidal spectrometer for reactions in inverse kinematics". *Nuclear Instruments and Methods in Physics Research Section A: Accelerators, Spectrometers, Detectors and Associated Equipment* 580 (2007), pp. 1290–1300.

[85] B. B. Back et al. "First Experiment with HELIOS: The Structure of ^{13}B". *Physical Review Letters* 104 (2010), p. 132501.

[86] R. Paschotta. *Position-sensitive Detectors*. URL: `https://www.rp-photonics.com/position_sensitive_detectors.html`.

[87] C. Hoffman. *HELIOSmatics: part of the "digios" software package*. 2019. URL: `https://zenodo.org/record/3517238`.

[88] R. Brun and F. Rademakers. "ROOT — An object oriented data analysis framework". *Nuclear Instruments and Methods in Physics Research Section A: Accelerators, Spectrometers, Detectors and Associated Equipment* 389 (1997), pp. 81–86. URL: `https://www.sciencedirect.com/science/article/pii/S016890029700048X`.

[89] C. Angus et al. "Forthcoming" (2023).

[90] H. An and C. Cai. "Global deuteron optical model potential for the energy range up to 183 MeV". *Physical Review C* 73 (2006), p. 054605.

[91] F. D. Becchetti et al. "^{12}C(^{7}Li, t)^{16}O and stellar helium fusion". *Nuclear Physics A* 305 (1978), pp. 293–312.

[92] C. M. Vincent and H. T. Fortune. "New Method for Distorted-Wave Analysis of Stripping to Unbound States". *Physics Review C* 2 (1970), pp. 782–792. URL: `https://link.aps.org/doi/10.1103/PhysRevC.2.782`.

[93] A. R. Stanford and P.A. Quin. "Study of stripping to levels of ^{21}Ne". *Nuclear Physics A* 342 (1980), pp. 283–292.

[94] A. J. Howard, J. O. Pronko, and C. A. Whitten. "Studies on ^{21}Ne and ^{23}Ne via the ^{20}Ne(d, p)^{21}Ne and ^{22}Ne(d, p)^{23}Ne reactions". *Nuclear Physics A* 152 (1970), pp. 317–336.

[95] S Thummerer et al. "Gamma-decay study of ^{21}Na and ^{21}Ne, octupole bands in ^{21}Ne". *Journal of Physics G: Nuclear and Particle Physics* 29 (2003), pp. 509–519.

[96] C. Wheldon et al. "Octupole-deformed molecular bands in ^{21}Ne". *European Physical Journal A* 26 (2005), pp. 321–326.

[97] C. Rolfs and H. P. Trautvetter. "A study of excited states of ^{21}Ne". *Nuclear Physics A* 189 (1972), pp. 661–664.

[98] H. T. Fortune, J. D. Garrett, and R. Middleton. "Neutron pickup from ^{22}Ne". *Physical Review C* 19 (1979), pp. 1615–1623.

[99] A. Hoffman et al. "Structure of the mirror nuclei ^{21}Ne and ^{21}Na". *Zeitschrift für Physik A* 332 (1989), p. 289.

[100] R. B. Firestone. "Nuclear Data Sheets for A = 21". *Nuclear Data Sheets* 103 (2004), pp. 269–324.

[101] P.M. Endt. "Energy levels of A = 21–44 nuclei (VII)". *Nuclear Physics A* 521 (1990), pp. 1–400.

[102] H. O. Cohn and J. L. Fowler. "Differential Elastic Scattering of Neutrons from Neon". *Physical Review C.* 114 (1958), pp. 194–200.

[103] S. Hinds and R. Middleton. "The Energy Levels of ^{21}Ne". *Proceedings of the Physical Society* 74 (1959), pp. 779–782.

[104] M. Heil et al. "Stellar neutron capture cross sections of ^{20,21,22}Ne". *Physical Review C* 90 (2014), p. 045804.

[105] C. E. Porter and R. G. Thomas. "Fluctuations of Nuclear Reaction Widths". *Physical Review* 104 (1956), pp. 483–491.

[106] M. Williams et al. "Private Communcation" (2024).

[107] F. Hammache et al. "Forthcoming" (2024).

[108] B. Davids et al. "Initial operation of the recoil mass spectrometer EMMA at the ISAC-II facility of TRIUMF". *Nuclear Instruments and Methods in Physics Research Section A: Accelerators, Spectrometers, Detectors and Associated Equipment* 930 (2019), pp. 191–195.

[109] K. Jayamanna et al. "Off-line ion source terminal for ISAC at TRIUMF". *Review of Scientific Instruments* 79 (2008), p. 02C711.

[110] G. Mauri. *Development and characterization of detectors for large area application in neutron scattering and small area application in neutron reflectometry.* 2019.

[111] M. Hamid and S. Bri. "Micromegas Detector Using 55 Fe X-ray Source". *International Journal of Advanced Research* (2013).

[112] G. Hackman and C. E. Svensson. "The TRIUMF-ISAC gamma-ray escape suppressed specrometer, TIGRESS". *Hyperfine Interactions* 225 (2014), pp. 241–251.

[113] J. Williams et al. "Implementation of the Doppler shift attenuation method using TIP/TIGRESS at TRIUMF: Fusion-evaporation lifetime measurements in ^{22}Ne". *Nuclear Instruments and Methods in Physics Research Section A: Accelerators, Spectrometers, Detectors and Associated Equipment* 859 (2017), pp. 8–17.

[114] C. E. Svensson et al. "TIGRESS: TRIUMF-ISAC gamma-ray escape-suppressed spectrometer". *Journal of Physics G: Nuclear and Particle Physics* 31 (2005), S1663–S1668.

[115] V. Godinho et al. "Characterization and Validation of a-Si Magnetron-Sputtered Thin Films as Solid He Targets with High Stability for Nuclear Reactions". *ACS Omega* 1 (2016), pp. 1229–1238.

[116] P.C. Bender et al. "GRSISort - A lean, mean, sorting machine" (2019). URL: `https://github.com/GRIFFINCollaboration/GRSISort`.

[117] B. Davids and G. Hackman. "Private communication" (2023).

[118] E. Wallander et al. "States in ^{89}Sr excited by the ^{86}Kr(α, n)^{89}Sr reaction". *Nuclear Physics A* 361 (1981), pp. 387–398.

[119] M. Williams et al. "Cross sections of the ^{83}Rb$(p,\gamma)^{84}$Sr and ^{84}Kr$(p,\gamma)^{85}$Rb reactions at energies characteristic of the astrophysical γ process". *Physical Review C* 107 (2023), p. 035803.

[120] M. Bozoian. "A useful formula for departures from Rutherford backscattering". *Nuclear Instruments and Methods in Physics Research Section B: Beam Interactions with Materials and Atoms* 82 (1993), pp. 602–603.

[121] B. Davids. "Private communication" (2023).

[122] G. Schiwietz and P. L. Grande. "Improved charge-state formulas". *Nuclear Instruments and Methods in Physics Research Section B: Beam Interactions with Materials and Atoms* 175-177 (2001), pp. 125–131.

[123] J. Allison et al. "Geant4 developments and applications". *IEEE Transactions on Nuclear Science* 53 (2006), pp. 270–278.

[124] J. Allison et al. "Recent developments in Geant4". *Nuclear Instruments and Methods in Physics Research Section A: Accelerators, Spectrometers, Detectors and Associated Equipment* 835 (2016), pp. 186–225.

[125] S. Agostinelli et al. "Geant4—a simulation toolkit". *Nuclear Instruments and Methods in Physics Research Section A: Accelerators, Spectrometers, Detectors and Associated Equipment* 506 (2003), pp. 250–303.

[126] B. Davids et al. “Private communication” (2023).

[127] A. Simon et al. “Impact of the α optical model potential on the γ-process nucleosynthesis”. *Journal of Physics G: Nuclear and Particle Physics* 44 (2017), p. 064006.

[128] M. Williams. “Private communication” (2023).